

Diffusion Related Processes in Nanoconfined Liquids and in Proteins Under Force

Liwen Cheng

Submitted in partial fulfillment of the
requirements for the degree
of Doctor of Philosophy
in the Graduate School of Arts and Sciences

COLUMBIA UNIVERSITY

2012

©2012

Liwen Cheng

All Rights Reserved

ABSTRACT

Diffusion Related Processes in Nanoconfined Liquids and in Proteins Under Force

Liwen Cheng

This thesis investigates some diffusion related problems, in acetonitrile confined in silica nanopores, and in modeling single molecule forced rupture experiments of biomacromolecules. Based on a method used to calculate the position-dependent diffusion coefficients in inhomogeneous liquids, we apply absorbing boundary conditions in the analysis of molecular dynamics trajectories of confined acetonitrile. We show that the dynamics of acetonitrile may be described by a two population exchange model that accounts for bulk-like relaxation in the center, frustrated dynamics near the surface of the pore and the self-diffusion. We find that hydrogen-bonding interactions play a large role in engendering this behavior. We compare our method with prior techniques that do not take diffusion into account and discuss their pitfalls. We also calculate the position-dependent diffusion tensors in the center population of acetonitrile. To model single molecule forced rupture experiments under constant velocity conditions, we study the barrier crossing problem of a diffusive particle in a time-dependent potential. We develop an integral equation connecting the first passage time distribution of a Brownian diffusion process in the presence of an absorbing boundary condition and the corresponding Green's function in the absence of the absorbing boundary. We further investigate the numerical solutions of the integral equation for a diffusion process in a time-dependent potential. Our numerical procedure, based on the exact integral equation, avoids the adiabatic approximation used in the previous analyt-

ical theories and is useful for fitting the rupture force distribution data from experiments, especially at larger pulling speeds, large cantilever spring constants, and smaller reaction rates. We also propose a model based on subdiffusion to explain the anomalous rupture force distributions with positive skewness that are observed in some single molecule forced rupture experiments of ligand-receptor complexes.

Table of Contents

1	Introduction	1
1.1	Structure and Dynamics of Nanoconfined Liquid Acetonitrile	2
1.2	First Passage Time Distribution in Stochastic Processes with Application to Biological Rupture Experiments	7
2	Force Field Development and System Setup	10
2.1	Force Field Development	10
2.2	System Setup and Simulation Protocol	19
3	Structure and Dynamics of Acetonitrile Confined in Silica Pores	23
3.1	Propagating Bilayer Structure	23
3.1.1	Number density profile	23
3.1.2	Orientational profile of acetonitrile	25
3.1.3	Charge density profile and hydrogen bond effect	28
3.1.4	Structure of acetonitrile in a larger pore	32
3.2	Two Population Dynamics	33
3.2.1	Singlet reorientational dynamics and hydrogen bond effect	34
3.2.2	Two population exchange model	38
3.2.3	Parallel diffusion	41
3.2.4	Dynamics of acetonitrile in a larger pore	43

3.3	Comparison of Two Analysis Methods	47
3.4	Diffusion Tensor Calculation of Liquids Confined in Cylindrical Pores	50
3.4.1	Parallel diffusion coefficient	51
3.4.2	Perpendicular diffusion coefficient	52
3.4.3	Correction to the positions of the absorbing boundaries	54
3.4.4	Results	55
3.5	Conclusions	59
4	First Passage Time Distribution in Stochastic Processes with Application to Forced Rupture Experiments	61
4.1	Single Molecule Forced Rupture Experiments	61
4.2	Kramers' Theory	63
4.3	Adiabatic Approximation for a Time-dependent Potential in Forced Rup- ture Experiments	66
4.4	Integral Equations of First Passage Time Distribution	68
4.4.1	Some analytical solutions	70
4.4.2	Numerical solutions	72
4.5	Subdiffusion Model for Anomalous Rupture Force Distribution	77
4.6	Conclusion	84
	Bibliography	85
A	Analytical solutions of the first passage time distribution for three model po- tentials	94
B	Time-dependent Green's function for a linear stochastic process in the absence of an absorbing boundary	97

List of Figures

2.1	Snapshot of the small slit system used in Born-Oppenheimer molecular dynamics simulations. Color code: yellow, silicon; red, oxygen; white, hydrogen; blue, nitrogen; cyan, carbon.	12
2.2	The renormalized radial distribution functions between atoms of the silanol group (the hydroxyl oxygen OH and the hydroxyl hydrogen HY) and the heavy atoms of acetonitrile (the cyanide nitrogen NZ, the cyanide carbon CZ and the methyl carbon CT) in the silica slit system simulated by classical molecular dynamics with force field (black), ab initio molecular dynamics with DZVP basis set (red), and ab initio molecular dynamics with TZV2P basis set (blue).	17
2.3	The renormalized radial distribution functions between atoms of the silanol group (the hydroxyl oxygen OH and the hydroxyl hydrogen HY) and the heavy atoms of acetonitrile (the cyanide nitrogen NZ, the cyanide carbon CZ and the methyl carbon CT) in the silica slit system simulated by classical molecular dynamics with our force field (black), classical molecular dynamics with the force field of Morales <i>et al.</i> (red), and ab initio molecular dynamics with DZVP basis set (blue).	18

2.4	Snapshots of the silica pore of diameter 24 Å filled with acetonitrile. Left panel: when looking down the axis of the cylindrical pore (Z axis of the box). Right panel: when looking at the X-Z cross section at $y = 28.64$ Å, only half of the box is shown. Color code: yellow, silicon; red, oxygen; white, hydrogen; blue, nitrogen; cyan, carbon.	20
3.1	The number densities of different atoms plotted as a function of the radial distance from the center of the silica pore of diameter 24 Å. The top, middle and bottom panels depict the results for the OH, O, and CH ₃ systems, respectively. Black, red, and green color are for the nitrogen, cyanide carbon, and methyl carbon of acetonitrile. Blue, silanol oxygen or surface methyl group; brown, silicon; orange, silica oxygen. The data for the silica oxygen are divided by two for better comparison.	24
3.2	The orientational density distribution $F(r, \cos \theta)$ as defined in the text. Panels A, B, and C depict the distribution computed from the OH, O, and CH ₃ pores of diameter 24 Å, respectively.	27
3.3	The charge density of acetonitrile (black) and silica (red) plotted as a function of the radial distance from the center of the silica pore of diameter 24 Å. Panels A, B, and C are for the OH, O, and CH ₃ systems, respectively.	30
3.4	The radial distribution function (RDF) of various species in the OH (top panel) and O (bottom panel) pores of diameter 24 Å. The black line is the RDF between the oxygen atoms of silanols and the nitrogen atoms of acetonitrile. The red line is the RDF between the oxygen atoms of silanols and the cyanide carbon atoms of acetonitrile. The blue line is the RDF between the oxygen atoms of silanols and the methyl carbon atoms of acetonitrile.	31
3.5	The orientational density distribution $F(r, \cos \theta)$ as defined in the text for the acetonitrile in the hydroxylated silica pore of diameter 44 Å.	32

3.6	The charge density of acetonitrile in two hydroxylated silica pores of diameters 24 Å and 44 Å. The red curve is for the 44 Å pore. The black curve for the 24 Å pore has been shifted to the right by 10 Å in order to better compare the behavior at the silica-acetonitrile interface.	33
3.7	(A) A snapshot of the silica pore of diameter 24 Å filled with acetonitrile, taken looking down the axis of the cylindrical pore. (B) A schematic representation of the division of the acetonitrile into two populations. Red indicates the surface population and blue indicates the center population. . .	35
3.8	(A): The singlet reorientational time correlation function of acetonitrile in different regions in the OH, CH ₃ and O of diameter 24 Å. (B): The time correlation function of the fluctuations in the singlet orientation obtained by first subtracting the plateau value, and then renormalization the results shown in panel A. The red, blue and green colors indicate the OH, CH ₃ and O pores, respectively. Black is for the bulk. The solid and dotted lines are for the surface population and the center population, respectively.	37
3.9	The singlet reorientational time correlation function of the total population in the OH pore of diameter 24 Å as calculated by definition (red solid line) and approximated by our two-population model (red dotted line). The survival probabilities of acetonitrile in the surface population (black line) and the center population (blue line) of the OH pore of diameter 24 Å.	40
3.10	The mean square displacements of acetonitrile in different regions in the OH, CH ₃ and O pores of diameter 24 Å. The red, blue and green colors are for the OH, CH ₃ and O pores, respectively. The solid and dotted lines are for the surface population and the center population, respectively. Black indicates the behavior of the bulk acetonitrile.	42

- 3.11 The dynamical properties of acetonitrile in two hydroxylated pores of diameters 24 Å and 44 Å calculated by the survival probability method for the surface population and the center population. Panel A depicts the singlet reorientational time correlation functions. Panel B shows the mean square displacements. The red and blue curves depict the the surface population and the center population, respectively. The solid and dotted lines indicate the 24 Å pore and the 44 Å pore, respectively. 45
- 3.12 The singlet reorientational time correlation function of the total population for the acetonitrile in the hydroxylated pore of diameter 44 Å as calculated by definition (red solid line), and approximated by our two-population model (red dotted line). Also shown are the three functions used in the two-population model: the survival probability of acetonitrile in the surface population (magenta line), the singlet reorientational time correlation functions for the surface population (black line) and the center population (blue line) calculated by the survival probability method. 46
- 3.13 The dynamical properties of acetonitrile in the 24 Å OH pore calculated by two different methods. Panel A shows the singlet reorientational time correlation functions and the survival probabilities. Panel B depicts the mean square displacements. The red and blue colors indicate the surface population and the center population, respectively. The solid and dotted lines depict the results of the survival probability and the initial position method, respectively. The dashed magenta and green lines denote the survival probabilities of the surface population and the center population, respectively. 49

3.14	The axial mean square displacements (A) and the natural logarithms of the radial eigenfunction autocorrelation functions (B) are shown for acetonitrile in four different layers in the hydroxylated silica pore of diameter 44 Å. The black, red, blue and green colors are for the {0 Å, 3.8 Å}, {3.8 Å, 8.2 Å}, {8.2 Å, 12.5 Å}, {12.5 Å, 17.0 Å} layers, respectively. . . .	58
4.1	Schematic representation of a single molecule forced rupture experiment . . .	62
4.2	Several different potentials where we can solve the boundary value problem analytically. The particle starts from a position x_0 and disappear when passing over the point b . From left to right, $V_0(x) = 0$, $V_0(x) = -Fx$, and $V_0(x) = \frac{1}{2}kx^2$	71
4.3	Survival probabilities at four different pulling speeds and two different diffusion constants calculated from several numerical and analytical methods. The k_0 rates are 10^{-4} s^{-1} (A and B) and 10^{-5} s^{-1} (C and D) respectively. Four pulling speeds $v = 0.6, 6.0, 60.0$ and 600.0 nm/ms are studied. Black, red, green and blue lines are numerical results from stochastic simulation, numerical results from the integral equation, approximated analytical results and the Gaussian upper limit results respectively. Black and red lines overlap in all graphs. Black, red and blue dash lines in graph (B) and (D) overlap. The pulling spring constant is $k_s = 10 \text{ pN/nm}$ and $x_0 = 0$. We have put circles on the black lines (simulation results) and crosses on the blue lines (upper limit results) for a better view.	74
4.4	Survival probability at two different pulling speeds, similar to Fig. 4.3 (A) but for the pulling spring constant $k_s = 50 \text{ pN/nm}$. Black and red lines overlap. All the labels are the same as in Fig. 4.3.	75

4.5	Rupture force distributions at two different pulling speeds, intrinsic rates and effect pulling constants calculated from stochastic simulation (black circles or squares), the integral equation (red), and the approximated analytical theory (green). See Eqs 4.32, 4.26 and 4.29.	76
4.6	Survival probabilities simulated for subdiffusion in the potential defined in Eq 4.17 at different α . Top panel: plotted in normal scale; Bottom panel: plotted in logarithmic scale on both axes. Red, green, and blue are for α at 0.8, 0.6, and 0.4 respectively. The results for $\alpha = 1$ simulated in Brownian dynamics are shown in black color.	83
4.7	Rupture force distribution simulated for subdiffusion in the potential defined in Eq 4.17 at different α . Red, green, and blue are for α at 0.8, 0.6, and 0.4 respectively. The result for $\alpha = 1$ simulated in Brownian dynamics is shown in black color.	84

List of Tables

2.1	Intramolecular parameters of silanol	14
2.2	Partial charges on atom sites	14
2.3	Lennard Jones parameters for silica acetonitrile interactions.	15
3.1	Diffusion coefficients for acetonitrile in four different layers in the hydroxylated silica pore of diameter 44 Å	59

Acknowledgments

First and foremost, I would like to thank my adviser Prof. Bruce Berne for his guidance and support. His broad knowledge, scientific insights, art of lecturing, optimistic personality, patience all help me through the years. Specially, I am indebted to him for his sympathy and generosity to approve, when I knew my father's illness and asked for a leave during my study.

I would like to thank my collaborators: Dr. Joseph Moraine, Prof. Xiongnu Hi and Dr. Sterling Para more. They are always ready to help. Joe developed the force field used in the silica-Central project, and contributed many insights in helpful discussions. Without his contribution, it is impossible to complete the silica-acetonitrile project. Zhonghan and I worked together on the single molecule rupture project when he was a postdoc in Prof. Berne's group, he came up with the main idea of the integral equation approach. He encouraged me a lot, and I am overwhelmed by his diligence and keen interest on theory. In the early stage of the silica project, Sterling used the force matching method to develop a force field for bulk silica, and showed me many useful computer codes.

I would like to thank my graduate committee members, Prof. David Reichman and Prof. Angelo Cacciuto, for their helpful comments on my qualification and original research proposal. I would like to thank Dr. Ruhong Zhou and Prof. Sanat Kumar for their time to serve on my dissertation committee.

I would like to thank Prof. David Reichman, Prof. Bruce Berne, and Prof. Richard Friesner for their insightful and stimulating lecture on statistical mechanics and quantum

mechanics.

I would like to thank many other people I met in the theory groups at Columbia, for creating a wonderful working environment and the time we enjoyed together. In particular, Prof. Jingyuan Li, Dr. Lingle Wang, Dr. Shulu Feng, Jing Zhang, Dr. Lan Hua, Dr. Yuhui Li, Dr. Jianing Li, Dr. Severin Schneebeli, Dr. Li Tian, Dr. Ting Wang, Dr. Suwen Zhao, Dr. Kai Zhu, Prof. Thomas Markland, Dr. Jagannath Mondal, Dr. Razvan Nistor, Dr. Guillaume Stirnemann, Dr. Mortan Hagen and Prof. Ronen Zangi.

I would like to thank my friends at Columbia. Without their companion, life at graduate school would be much harder.

Finally, I would like to thank my family for their unconditional love and support. My parents gave me a warm family so that I can focus on my study. I think I can totally understand their love and sacrifice only if I have a child in the future. My father is an honest and hardworking man. I am proud of him. Unfortunately he passed away on January 3rd 2012, after fighting with late stage lung cancer for one year. Wish he could know I passed my dissertation defense on March 29th 2012. My grandparents also looked after me before my middle school. I can easily recall the beautiful memories, how my grandfather tutored me in learning Chinese characters and math, how my grandmother prepared food and games for kids. Also, I feel so lucky to have my perfect other half. Without my wife's encouragement and understanding, I could not complete my graduate study. I am so sorry that I did little for them in the past.

To my wife Ting Jin,
my mother Lan Lv,
my grandparents Zuomou Cheng and Jizhao Peng,
my deceased father Xuening Cheng.

Chapter 1

Introduction

Diffusion is a kinetic process of fundamental importance in physics, chemistry and biology, e.g., diffusion controlled reactions, osmosis in living cells, doping in semiconductors. Einstein's study on Brownian motion showed that the random motion of a Brownian particle is a result of short and uncorrelated random hits by the molecule under thermal motion in the medium. The mean square displacement of a Brownian particle grows linearly in time $\langle \Delta r(t)^2 \rangle = 2dDt$, where d is the dimensionality and D is the diffusion coefficient. Einstein derived an equation relating the diffusion coefficient to the friction coefficient, from which the Avogadro's constant can be measured. Experiments later on confirmed Einstein's theory on Brownian motion, and verified the existence of atoms and the kinetic theory.

Diffusion in inhomogeneous liquids, such as liquids near solid surfaces or liquids confined in pores is not easy to study. Since the surface breaks the symmetry and induces layering effect in liquids, the diffusion tensor can be anisotropic and the diffusion coefficients can be position-dependent. We carry out molecular dynamics simulations of liquid acetonitrile confined in cylindrical silica pores. The silica surfaces induces a propagating bilayer structure in acetonitrile. To investigate the position-dependent diffusion of confined acetonitrile, we impose absorbing boundary conditions in different concentric layers

in the analysis of molecular dynamics trajectories, following a recent method.¹ Acetonitrile near the pore surface exhibits subdiffusion, while acetonitrile in the center region exhibits Brownian diffusion. The diffusion tensors are calculated in different layers of the center region. We also extend the analysis method using absorbing boundary conditions to the study of the singlet reorientation dynamics of acetonitrile in different layers. We show that it is necessary to take into account the diffusion from the surface population to the center population in order to explain the singlet reorientation dynamics of the total population.

Brownian diffusion in a time-independent external potential with absorbing boundaries entails Kramers' theory,² which is fundamental in understanding chemical reactions in condensed phases. To understand the kinetics in single molecule force rupture experiments, Hummer and Szabo extended Kramers' theory to a time-dependent one dimensional potential, and obtained approximate analytic formulas for survival probabilities and rupture force distributions.³ We propose an integral equation approach to obtain the first passage time distributions numerically, when the approximate formulas of Hummer and Szabo fail. Brownian dynamics on a one dimensional potential can not explain the anomalous rupture force distributions with positive skewness observed in some experiments on ligand-receptor complexes⁴⁻⁹. Although a static disorder model can explain this anomaly,¹⁰ we argue that an alternative model based on subdiffusive dynamics can also explain this.

1.1 Structure and Dynamics of Nanoconfined Liquid Acetonitrile

The study of liquids confined or near an interface is an area of active experimental and computational investigation. The properties of liquids under these conditions can be very different than in the bulk. For example, the phase behavior of liquids in confinement is changed. The freezing point depression of confined liquids is predicted by the Gibbs-Thomson equa-

tion, and the boiling point elevation is predicted by the Kelvin equation.^{11,12} The glass transition temperature of confined liquids is also shifted.¹³ The mechanical properties can be also altered,^{14,15} Khan *et al.*¹⁵ observed a sharp transition from viscous to elastic responses when compressing nanoconfined water between the mica substrate and the atomic force microscopy (AFM) tip.

The properties of confined liquids depend intriguingly on the size of the confinement and the functionalization of the surfaces. For liquids confined in small pores with diameters of several nanometers, the fraction of interfacial molecules is large and the interactions with the functionalized surfaces becomes important. The classic interpretations based on macroscopic concepts break down for nanoconfined liquids. For example, Morineau *et al.*¹⁶ observed that the glass transition temperature of toluene confined in regular porous silicates (MCM-41 and SBA-15) is elevated for pores of diameter smaller than 3.5 nm but depressed for pores of diameter larger than 3.5 nm, compared to the bulk value. Quellec *et al.*¹⁷ found that the glass transition temperature of ortho-terphenyl (oTP) confined in porous silica with a pore size around 7 nm increases when the silica surface is hydroxylated with hydroxyl groups and decreases when the silica surface is silanized with trimethylsilyl groups, compared to the bulk value. And oTP confined in hydroxylated porous silica exhibits two glass transitions at 269 K and 243 K, one higher and one lower than the bulk value 248 K.¹⁷ These experiments suggest that the interfacial layer of confined liquids have frustrated dynamics when their interactions with surfaces are not too weak, while the inner layer of confined liquids could have faster dynamics than in bulk. The finite size effect will be enhanced when reducing the pore size, but what is more important for nanoconfined liquids is that the fraction of interfacial molecules will be increased, thus the properties of nanoconfined liquids can have non-monotonic dependence on the pore size.

In the present work, acetonitrile confined in nanosized porous silica is studied. Acetonitrile (CH_3CN) is a polar, aprotic, linear molecule with amphiphilic character in the sense

that the cyanide end is capable of accepting hydrogen bonds whereas the methyl group has hydrophobic character. Acetonitrile is a good polar aprotic solvent of high dielectric constant (37.5 at ambient conditions) and large dipole moment (3.92 debye). Acetonitrile in porous structure has many applications. In supercapacitors,^{18,19} acetonitrile is used as the solvent of the electrolytes due to its high dielectric constant and chemical inertness; porous carbon or carbon nanotubes are used as the electrode to increase the surface area of the electric double layer. In chromatography, acetonitrile is used as a cosolvent in the mobile phase since it is miscible with water; porous silica is used as the stationary phase since it can be easily synthesized and functionalized with different chemical groups.

Experiments have been performed to elucidate the behavior of acetonitrile confined in porous silica.²⁰⁻²⁵ Acetonitrile molecules close to the interface can form hydrogen bonds with the silanol groups, resulting in a blue shift of the C≡N stretching band observed in fourier transform infrared spectroscopy (FTIR),²²⁻²⁴ and a characteristic peak corresponding to the 2.6 Å distance from the hydrogen-bonded nitrogen atom to the silanol oxygen atom in X-ray diffraction.²⁵ Acetonitrile in the center region of a hydroxylated silica pore of diameter 37 Å has similar structure to bulk acetonitrile.²⁵ The collective reorientational dynamics of acetonitrile confined in silica pores of diameter 24 Å and 44 Å was studied by Loughnane *et al.* using optical Kerr effect (OKE) spectroscopy.²⁰ The autocorrelation functions are found to be well fit with triple exponential functions based on the assumption that there are two exchanging populations, a dynamically frustrated surface population, and a population that exhibits bulk-like relaxation times in the center of the pore. The authors suggested that acetonitrile in the frustrated surface population forms an anti-parallel bilayer structure. One sublayer effectively anchored by hydrogen bonding interactions is pointing with the nitrogen end toward the surface. Another sublayer exchangeable with the center population is pointing in the opposite direction due to dipole pairing effect between neighbor acetonitrile molecules.

Several recent simulation studies^{26–29} have complimented the experimental work. These studies have employed potentials describing the acetonitrile–silica interactions based on combining rules that were not optimized by further fitting to experimental or *ab initio* data. Despite this, several aspects of the simulations are in general agreement with the picture provided by experiments.^{20–25} Morales and Thompson’s simulation²⁶ confirmed that the blue shift of the C≡N stretching band in FTIR^{22–24} for nanoconfined acetonitrile in hydroxylated silica pores is due to the charge transfer effects of hydrogen bonding. The antiparallel bilayer structure proposed by Loughnane *et al.*²⁰ was observed in Morales and Thompson’s simulation.²⁶ A simulation of acetonitrile on a flat hydroxylated silica surface²⁸ showed that the antiparallel bilayer structure can propagate into the acetonitrile for about 2 nm. Morales and Thompson argued that the ordering of acetonitrile near the surface is mainly due to the electrostatic liquid-wall interactions and not the explicit hydrogen bonding of silanols to acetonitrile.²⁶

This study revisits the problem of acetonitrile confined in silica nanopores. We utilize a force field that is parametrized to yield good agreement with first principles computations, particularly in terms of the hydrogen bonding interactions between silanol groups at the surface and the acetonitrile. This force field is then utilized in extensive molecular dynamics simulations to study acetonitrile confined in a nanopore. In order to assess the importance of explicit hydrogen bonding and surface charge, we additionally perform simulations where silanols are replaced by methyl groups as well as simulations in which the H site is eliminated and its charge is “absorbed” into the oxygen site of the OH group.²⁶ In agreement with Ref. 26, we find that the observed long range order can be explained by non-specific electrostatic interactions. However, we find that hydrogen bonding is essential to describe the slow relaxation associated with the first layers of acetonitrile at the surface. More generally, we show that the reorientational and diffusional dynamics of acetonitrile near the interface is significantly frustrated by surface interactions. The relaxation near the

surface speeds up when hydrogen bonding interactions are muted, and it increases further when the magnitude of the surface charge distribution is lowered by methylation of the silanol groups. Furthermore, we find that a two-population exchange model is a reasonable description of reorientational dynamics, in agreement with the OKE experiment.²⁰ This picture is also consonant with a recent study by Milischuk and Ladanyi³⁰ which reported frustrated dynamics near the silica surface and bulk-like dynamics in the center region for water confined in a silica pore. The parallel diffusion exhibits subdiffusive behavior for acetonitrile near the silica surface and Brownian behavior for acetonitrile in the center region of the pore.

In order to investigate the dynamics we extend a recently developed method¹ to calculate relevant time correlation functions for molecules in different layers of the pore. This method takes into account the short lifetimes of the molecules in the layers, whereas in a recent study³⁰ the approach adopted does not exclude contributions from molecules that can exchange between layers. This can lead to qualitative and quantitative errors when the lifetimes in any layer of interest are short. Comparing and contrasting our method with this previous method, we find that it gives an improved analysis of the spatial dependence of the dynamics.

We also investigate how the size of the pore affects the fluid structure and dynamics. Comparison of the properties of acetonitrile confined in two different sized hydroxylated silica pores of diameters 24 Å and 44 Å reveals that the timescale of singlet reorientational dynamics of acetonitrile in different layers is insensitive to the diameter of the pore, a result consistent with the OKE study,²⁰ but the angular distribution in the center of the small pore is not uniform whereas in the larger pore it is uniform.

Applying the recently developed method¹ to cylindrical geometry, the diffusion tensors are calculated for acetonitrile in different layers of the center region. The perpendicular diffusion coefficient can be computed from the autocorrelation function of the eigenfunction

of the radial diffusion equation with absorbing boundary conditions. The diffusion tensor is nearly isotropic for acetonitrile 1 nm away from the silica surface.

Chapter 2 presents the development of the specialized force field and the details of the simulation setup. Chapter 3 presents the results for the equilibrium and dynamical properties of acetonitrile confined in silica nanopores of diameters 24 Å and 44 Å. Section 3.1 shows the propagating bilayer structure resulting from the non-specific electrostatic interactions. Section 3.2 presents the results of reorientational and translational dynamics for the surface population and the center population using an extension of the recently developed method.¹ Section 3.3 shows that the method used in the present study gives a sharper picture of two population dynamics, compared to a previous technique.³⁰ Section 3.4 presents the details of diffusion tensor calculation of liquids confined in cylindrical pores and the results for acetonitrile confined in a silica pore of diameter 44 Å.

1.2 First Passage Time Distribution in Stochastic Processes with Application to Biological Rupture Experiments

First passage time distributions of stochastic processes in the presence of absorbing boundaries have important applications in diffusion controlled reactions, self-organized criticality, dynamics of neurons, and trigger of stock options.³¹ Recently, first passage models have been proposed to analyze the kinetics of unfolding (or bond rupture) in single-molecule pulling experiments by atomic force spectroscopy.^{3,32-34} Hummer and Szabo³ showed that a simple first passage time model incorporating Kramers rate theory can be used to extract much more accurate kinetic information than the previously used Bell's model.³⁵⁻³⁷ Their analytic theory fits experimental data for both the average rupture force as a function of pulling speed and the distribution of rupture forces at certain (usually slow) pulling speeds. Their work and the later works of Dudko *et. al.*^{32,33} and Freund³⁴ assumed a first-order rate

equation governing the decay of the survival probability with a time dependent rate constant ($\approx \exp(-\int_0^t d\tau k(\tau))$). The time dependent rate constant was obtained by extending the Kramers' theory for a time-dependent potential. It has been noted that their underlying adiabatic approximation breaks down^{3,32} at extreme pulling speeds where the rate of pulling is fast compared to the diffusion rate. In this work we will show how to bypass this approximation. Aside from its validity being dependent on the rate of pulling, the validity of the formulas based on the adiabatic assumption^{3,32-34} has never been investigated with respect to other parameters such as the cantilever spring constant and the intrinsic reaction rate even though reasonable parameters have been extracted from rupture experiments of unfolding proteins^{38,39} and unzipping of DNA hairpins.⁴⁰

We present integral equations connecting the first passage time distribution in the presence of an absorbing boundary condition and the corresponding conditional probability (Green's function) without the absorbing boundary. The equations are a generalized version of similar treatments of discrete random walks.^{41,42} We solve the integral equation analytically for three different potential functions to determine how the first passage time distribution of a particle diffusion is affected by time independent external fields. Because the first passage time distribution was already determined analytically by other methods, these three cases provide benchmarks that validate our integral equation approach. We then apply the integral equation to the case of time-dependent pulling experiments, and obtain numerical results for different pulling speeds, cantilever spring constants and intrinsic reaction rates. We show that the previous theory³ is likely to break down not only at larger pulling speeds, but also at smaller reaction rates and larger cantilever spring constants. The simple iteration scheme based on the integral equation will thus help to fit force distribution data at these conditions where the adiabatic approximation breaks down.

In some single molecule rupture force experiments on ligand-receptor complexes⁴⁻⁹, anomalous rupture force distributions with positive skewness are observed. This anomaly

can not be explained with Brownian diffusion in a one-dimensional potential. Static disorder model based on Gaussian distributions of the barrier height and the distance to transition state were called for to explain this anomaly.¹⁰ We propose an alternative model based on subdiffusion to explain this anomaly. Stochastic processes corresponding to subdiffusion in a time-dependent potential are simulated. The resulting rupture force distributions have positive skewness. Our subdiffusion model and the static disorder model both treat the inadequacy of using just one reaction coordinate for some complex systems. The exploration of other coordinates on a complex multi-dimensional potential could result in a broad waiting time distribution from one point to another point on the projected one dimensional potential of mean force.⁴³

Chapter 2

Force Field Development and System Setup

2.1 Force Field Development

One of the aims of the present work is the development of improved force fields to accurately describe the interactions of the silica surface with acetonitrile. As noted in the introduction this interface has previously been studied utilizing potentials based on standard combining rules and by adapting parameters from silica water interfaces.^{26–29} In Ref. 26 and 27, the force field parameters for acetonitrile and silica were from the ANL acetonitrile potential⁴⁴ and the Brodka and Zerda⁴⁵ silica potential, respectively. Then the parameters for van der Waals interactions between acetonitrile and silica were not specially optimized but obtained from combining rules. In Ref. 28 and 29, the parameters for silica were taken from Rossky and co-workers' work^{46,47} on silica-water systems. The parameters for acetonitrile were from the acetonitrile model of Nikitin and Lyubartsev.⁴⁸ Similarly, combining rules were used for van der Waals interactions between acetonitrile and silica. However the interactions present at this interface are rather subtle and a more

thorough parametrization is desirable. We have designed an interaction potential specialized for silica acetonitrile interfaces that is consistent with the structure garnered from first principles molecular dynamics simulation.

Born-Oppenheimer molecular dynamics simulations are carried out for a small slab system of acetonitrile confined in between two hydroxylated silica surfaces, utilizing the QUICKSTEP module within the CP2K package.⁴⁹ The system simulated is shown in Figure 2.1. The simulation box is a rectangular cuboid of length 14.32 Å, 14.32 Å, and 30 Å in the X, Y, and Z dimension. Amorphous silica is cleaved in two surfaces located at the top and bottom of the box, the undercoordinated sites generated are hydroxylated. Acetonitrile molecules are filled in between the silica slit. The system contains 41 silicon atoms, 115 oxygen atoms, 16 silanol groups (SiOH), 5 disilanol groups (Si(OH)₂) and 29 acetonitrile molecules. The electronic structure is computed by means of density functional theory and a combined Gaussian basis set/plane wave approach.⁴⁹ The system is simulated for 5 ps with the TZV2P basis set and for 20 ps with the smaller but more computationally efficient DZVP basis set. The Becke exchange and Lee-Yang-Parr correlation functions are employed in all first principles computations.^{50,51} Similar treatments have been previously used to simulate bulk acetonitrile and acetonitrile at anatase surfaces.^{52,53} Although the present trajectories are too short to study dynamical properties, they may be utilized to evaluate the structure at the first layer of the interface and provide data for the fitting of our classical potential. In particular, the hydrogen-bonded interaction between acetonitrile and the surface may be characterized. Our classical potential is tuned such that the structure of acetonitrile at the surfaces and the intramolecular structure of the silanol group in Born-Oppenheimer molecular dynamics simulations are well reproduced by classical molecular dynamics simulations.

Our classical potential is composed of terms arising from silica-silica, acetonitrile-

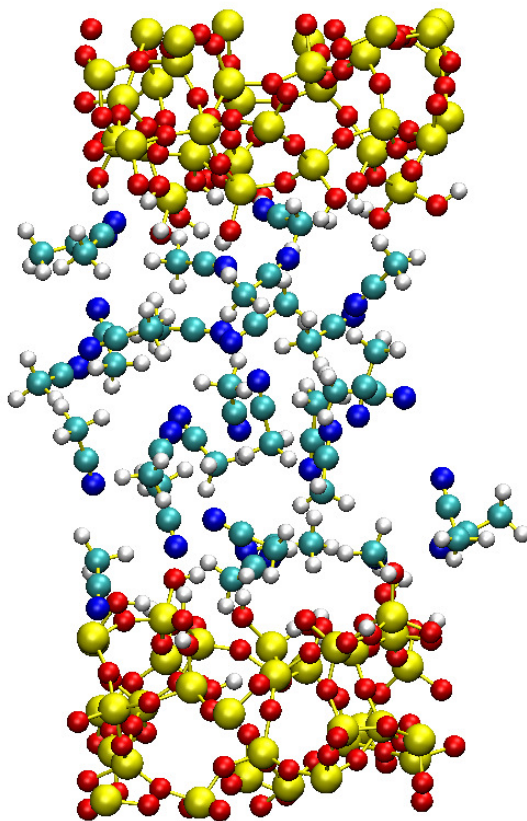


Figure 2.1: Snapshot of the small slit system used in Born-Oppenheimer molecular dynamics simulations. Color code: yellow, silicon; red, oxygen; white, hydrogen; blue, nitrogen; cyan, carbon.

acetonitrile, and interfacial interactions:

$$V = V_{\text{silica}} + V_{\text{acetonitrile}} + V_{\text{sil-acn}} \quad (2.1)$$

The silica term is adopted from a recent reparameterization of the BKS model⁵⁴ known as CHIK.⁵⁵ We utilize the OPLS/AA force field to treat the acetonitrile-acetonitrile interactions.⁵⁶ The surface of the silica is hydrolyzed, that is silanol groups replace surface defects, and their treatment is included in the interfacial term. The silanol groups are treated

in the following fashion. A partial charge of -0.8675 and $+0.39$ is assigned to the OH and H sites, respectively. The intramolecular structure of the silanol is treated as flexible with the harmonic bonding and bending potentials,

$$V_{\text{harmonic}} = \frac{1}{2}k(a - a_0)^2 \quad (2.2)$$

The intramolecular parameters of silanol are given in Table 2.1.

The interfacial term comprised of electrostatic and non-bonded terms is given by:

$$V_{\text{sil-acn}} = \sum_{i < j} \left(\frac{q_i q_j}{|r_{ij}|} + V_{\text{nb}}(r_{ij}) \right). \quad (2.3)$$

The parameters of the non-bonded potential were tuned to yield consistency with first principles molecular dynamics trajectories. The atomic partial charges are chosen to be consistent with the respective bulk potentials, except the partial charges on the OH and H sites of silanol groups are tuned.^{55,56} The atomic partial charges are given in Table 2.2. The non-bonded interactions given by V_{nb} are represented by a Lennard-Jones potential

$$V_{LJ} = 4\epsilon \left[\left(\frac{\sigma}{r} \right)^{12} - \left(\frac{\sigma}{r} \right)^6 \right] \quad (2.4)$$

with the exception of CZ-OH for which a Buckingham form is utilized,

$$V_{\text{buckingham}} = Ae^{-Br} - C/r^6, \quad (2.5)$$

with parameters $A = 36.9$ eV, $B = 1.95 \text{ \AA}^{-1}$, and $C = 21.7$ eV \AA^{-6} . The Lennard-Jones interactions between silicon sites and acetonitriles are taken to be small, in accord with prior parametrization.²⁶ The parameters for the Lennard-Jones interactions are given in Table 2.3.

Non-electrostatic interactions between the silanol hydrogen and other sites are not included in the potential with the exception of an additional 12-10 hydrogen bonding interaction⁵⁷ which is utilized to describe the hydrogen bond between the NZ and HY sites,

$$V_{\text{h-b}} = \frac{6^6}{5^5} \epsilon \left[\left(\frac{\sigma}{r} \right)^{12} - \left(\frac{\sigma}{r} \right)^{10} \right], \quad (2.6)$$

with parameters $\varepsilon = 200$ K and $\sigma = 1.70$ Å. We found it necessary include this term in order to reproduce hydrogen bonding without resort to increasing the magnitude of charge on the NZ or HY site, which was found to denigrate the model in other respects.

We utilize a united atom model for the methyl group with a partial charge of -0.2 and Lennard-Jones parameters $\sigma = 3.95$ Å and $\varepsilon = 0.732$ kJ/mol. Geometric combining rules are employed to generate the acetonitrile-methyl interactions.

pair	a_0	k
OH-HY	0.9515 Å	4.72×10^5 kJ mol ⁻¹ nm ⁻²
OH-SI	1.560 Å	9.16×10^5 kJ mol ⁻¹ nm ⁻²
Si-OH-HY	108.5°	300.0 kJ mol ⁻¹ rad ⁻²
OH-Si-OH	117.0°	300.0 kJ mol ⁻¹ rad ⁻²

Table 2.1: Intramolecular parameters of silanol

atom	charge (e)
NZ	-0.56
CZ	0.46
CT	0.08
HC	0.06
Si	1.91
O	-0.955
OH	-0.8675
HY	0.39

Table 2.2: Partial charges on atom sites

In Figure 2.2 we compare the radial distribution functions of the heavy atoms of acetoni-

pair	ϵ (K)	σ (Å)
OH-NZ	72.5	3.14
OH-CT	46.0	3.34
OH-HC	25.0	2.55
OH-OH	78.0	3.166
OX-NZ	75.7	3.35
OX-CZ	52.7	3.34
OX-CT	52.7	3.34
OX-HC	25.1	2.907
SI-NZ	9.25	3.02
SI-CZ	5.76	3.07
SI-CT	5.76	3.07
SI-HC	2.67	2.70

Table 2.3: Lennard Jones parameters for silica acetonitrile interactions.

trile from the silanol groups garnered from the first principles simulation with the results from classical molecular dynamics calculation using our force field developed, in the small slit system. The radial distribution functions have been renormalized following the method in Soper et al.'s work.^{58,59} It can be seen that the simulations performed with the two basis sets are in good agreement with each other, also from the first principles simulation, it is clear that the cyanide group accepts a hydrogen bond from the silanol. Hydrogen bonding plays a critical role in determining the nature of the interface, and reproducing such effects requires a careful balancing of electrostatic and other non-bonded interactions. Our force field has been optimized so as to yield good agreement with these distributions, in addition to other structural properties. One finds that our force field is successful at matching the first principles result. Furthermore it can be seen that the OH-NZ distribution and the HY-NZ

distribution sharply peak at approximately 2.8 angstroms and 1.8 angstroms respectively. This is again indicative of the presence of hydrogen bonding. Further analysis indicates that as expected those molecules that are closest to the surface prefer to be oriented with the nitrogen pointing towards the surface. This feature is consistent with the results of prior work.^{26,28,29}

In Figure 2.3 we compare the radial distribution functions from classical molecular dynamics simulations using two different force fields, one is the force field developed here and the other is the force field of Morales *et al.*^{26,27} The results from the first principle simulation with the DZVP basis set are also shown. It can be seen that in general our force field agrees with the first principles calculation better than the force field of Morales *et al.*. The induced ordering of acetonitrile are stronger in our force field than in the force field of Morales *et al.*. This is reflected in several differences in the radial distribution functions. In the OH-NZ distribution and the HY-NZ distribution, the two force fields agree with each other in the positions and heights of the first peaks. The hydrogen bonds are present in both of the two force fields. However, the OH-NZ distribution has much higher density in the force field of Morales *et al.* and develops a shoulder peak, at about 3.5 Å where it is the interstitial space between the first and second coordination shell with low density in our force field. In the OH-CT distribution, the second peak is missing in the force field of Morales *et al.*, instead a shoulder peak develops at the interstitial space. The probability densities of the HY-NZ distribution and the HY-CZ distribution are also higher at the interstitial spaces in the force field of Morales *et al.* than in our force field. In the OH-CZ distribution, the first peak is broader and shifted to the right in the force field of Morales *et al.*. These differences tell that the acetonitrile molecules in the force field of Morales *et al.* are less ordered and have more flexibility to fit in the adsorption sites on the hydroxylated silica surface, compared to our force field and the first principles simulation.

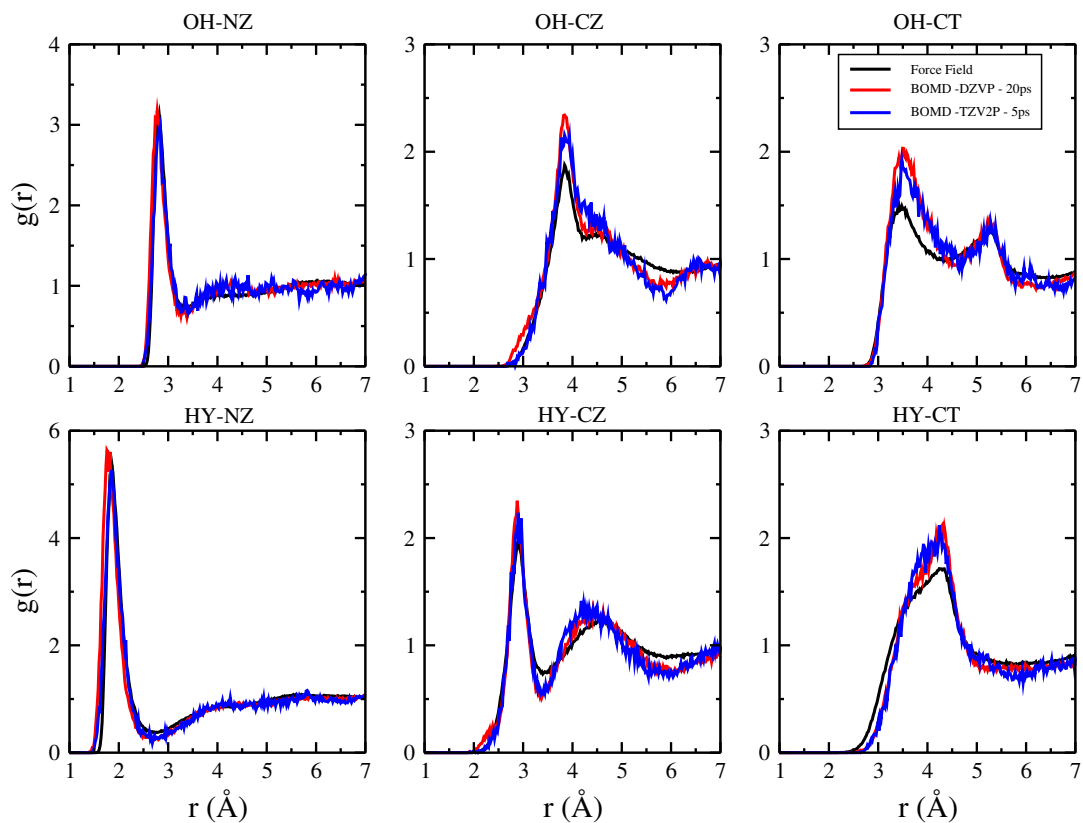


Figure 2.2: The renormalized radial distribution functions between atoms of the silanol group (the hydroxyl oxygen OH and the hydroxyl hydrogen HY) and the heavy atoms of acetonitrile (the cyanide nitrogen NZ, the cyanide carbon CZ and the methyl carbon CT) in the silica slit system simulated by classical molecular dynamics with force field (black), ab initio molecular dynamics with DZVP basis set (red), and ab initio molecular dynamics with TZV2P basis set (blue).

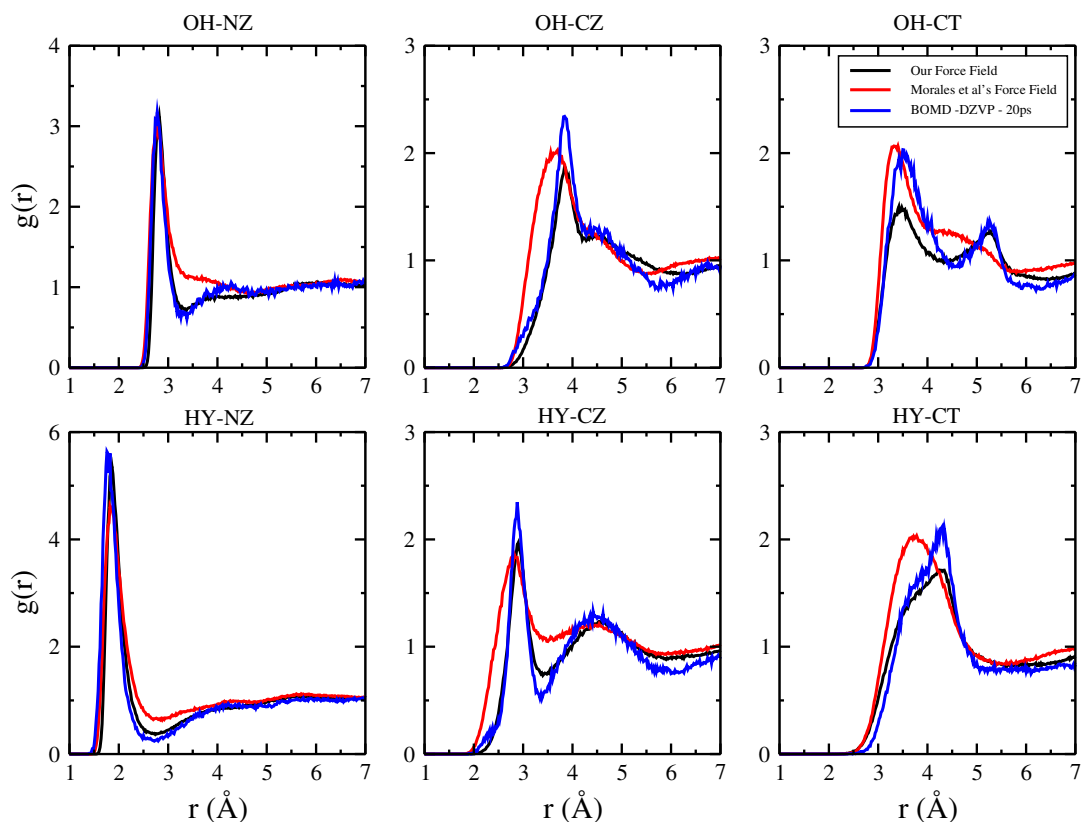


Figure 2.3: The renormalized radial distribution functions between atoms of the silanol group (the hydroxyl oxygen OH and the hydroxyl hydrogen HY) and the heavy atoms of acetonitrile (the cyanide nitrogen NZ, the cyanide carbon CZ and the methyl carbon CT) in the silica slit system simulated by classical molecular dynamics with our force field (black), classical molecular dynamics with the force field of Morales *et al.* (red), and ab initio molecular dynamics with DZVP basis set (blue).

2.2 System Setup and Simulation Protocol

The force field described in the previous section has then been utilized to perform large-scale molecular dynamics simulations of the structure and dynamics of acetonitrile confined in silica nanopores. We focus on acetonitrile molecules confined in a 24Å diameter silica nanopore, but also compare this system to one with a pore diameter of 44Å. The diameter of 24Å was chosen to match the average value studied in the OKE experiment²⁰ and other simulation work.^{26,27} A β -cristobalite crystal in a periodic cubic box of length 57.28Å was melted at 8000K. After annealing from 8000K to 300K, the amorphous silica structure was obtained. The nanopore was created by cutting a cylindrical hole out of the amorphous silica. This generates under-coordinated silicon and oxygen sites at the surface. The surface was functionalized with silanols by saturating the under-coordinated silicon with hydroxyl groups and the under-coordinated oxygens with hydrogen atoms, while keeping the whole system electrically neutral. The density of silanols at the surface is approximately 4.5 per nm² which is in agreement with the 2-6 per nm² range in experiments depending on the thermal history of the sample.^{20,60} The empty pore was then filled with 280 acetonitrile molecules. The number of acetonitrile molecules in the pore was determined by running an isothermal-isobaric ensemble (NPT) simulation where the pore was in a reservoir of acetonitriles at 1 atm and 300K, following the procedure in Rodriguez *et al.*'s work.⁶¹ In prior studies the density of acetonitrile in the pore has been calculated using grand canonical Monte Carlo.^{26,27} Our NPT simulations in liquid reservoir should predict similar densities as the grand canonical Monte Carlo simulation, provided, as is presently the case, that the height of the cylindrical pore and the thickness of the reservoir is sufficiently large. After filling the silica pore with the determined number of acetonitrile molecules, the final system contains 3319 silicon atoms, 6842 oxygen atoms, 122 silanol groups(SiOH), 21 disilanol groups(Si(OH)₂) and 280 acetonitrile molecules. Snapshots of the system are shown in Figure 2.4. The cylindrical pore is at the center of the simulation

box. The axis of the cylindrical pore is the Z axis of the simulation box. This system was equilibrated at 300K in canonical ensemble (NVT) simulation for 500 picoseconds. Starting from the positions and velocities in the equilibrated configuration, a production run was performed in the microcanonical ensemble (NVE) for 5 nanoseconds. The temperature was found to be 300K in the NVE production run. The trajectory was saved every 100 femtoseconds.

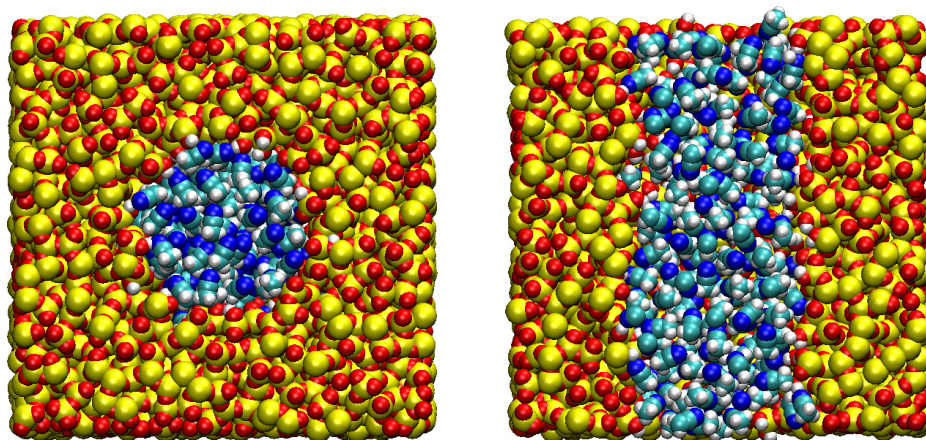


Figure 2.4: Snapshots of the silica pore of diameter 24 \AA filled with acetonitrile. Left panel: when looking down the axis of the cylindrical pore (Z axis of the box). Right panel: when looking at the X-Z cross section at $y = 28.64 \text{ \AA}$, only half of the box is shown. Color code: yellow, silicon; red, oxygen; white, hydrogen; blue, nitrogen; cyan, carbon.

In addition to the hydroxylated surfaces, simulations where the OH groups are replaced by methyl groups were performed. Unlike the case of the silanols, the interaction of acetonitrile with the methyl groups was garnered from combination rules and not from extensive reparameterization. Finally, to study how the removal of explicit surface hydrogen

bonds affects the dynamics of liquid acetonitrile, we simulated the silanol system where each silanol hydrogen site was eliminated and its charge was “absorbed” into the O of the OH site.²⁶ We refer to each model as OH, CH3, and O, respectively. The number of acetonitrile molecules were found to be 235 and 262, in the CH3 and O model respectively. A separate simulation for bulk acetonitrile was also performed in the NVE ensemble, after setting the proper density in the NPT ensemble at 1 atm and 300K. The bulk density was found to be 0.722g/cm^3 in the NPT simulation. The density in the center region of the pore was 0.673g/cm^3 , 0.691g/cm^3 and 0.704g/cm^3 for the OH, CH3 and O model respectively. The somewhat lower density in the center region than in bulk was also observed in grand canonical Monte Carlo simulations for water confined in silica nanopores.³⁰

In addition, we have simulated the properties of a larger hydroxylated silica pore of diameter 44\AA using the same procedure to obtain insight into the dependence of structural and dynamical properties on nanopore size. The system for this larger pore contains 5251 silicon atoms, 11018 oxygen atoms, 288 silanol groups, 84 disilanol groups and 1085 acetonitrile molecules in a cubic cell of length 71.6\AA . The density of silanols at the pore surface is about 4.6 per nm^2 . The density of acetonitrile in the center region of the pore is 0.682g/cm^3 .

All simulations were performed using the GROMACS 4.0.7 simulation package⁶² compiled in double precision. The leapfrog method with a timestep 1 femtosecond was used to integrate the equations of motion. The grid search algorithm with a cutoff 12\AA was used in the neighbor searching, and the neighbor lists were updated every timestep to ensure good energy conservation. A cutoff of 10\AA was used to compute the van der Waals interactions. The van der Waals interactions were looked up in tabulated tables prepared in advance, since the combination rules were not assumed in our force field. The Particle-Mesh Ewald (PME) algorithm was used to compute the electrostatic interactions. A cutoff of 12\AA and a switching function starting from 11\AA were used for the real space sum. A

grid spacing of 1 Å and a interpolation order of 6 were used for the reciprocal sum. The relative strength of the direct potential at the real space cutoff is 10^{-5} . The Nose-Hoover thermostat with a time constant 0.1 picosecond was used for the temperature coupling in the NVT and NPT runs. In the NPT runs that were carried out to determine the density of acetonitrile in the silica pores, the Z dimension of the box was doubled to 114.56 Å and the silica pore was put in a reservoir of 2100 acetonitrile molecules initially. An semi-isotropic Parrinello-Rahman barostat with a time constant 1 picosecond was used for the pressure coupling in the Z dimension of the box. The compressibility in the X/Y dimension and the Z dimension were 0 and $4.5 \times 10^{-5} \text{ bar}^{-1}$, respectively.

Chapter 3

Structure and Dynamics of Acetonitrile Confined in Silica Pores

3.1 Propagating Bilayer Structure

3.1.1 Number density profile

The number density profiles of different atoms as function of distance from the center of the pore are shown in Figure 3.1, for the OH, O, and CH₃ pores of diameter 24 Å. Taking account of the cylindrical symmetry of the system, the number density profile is defined as

$$\rho(r) = \frac{1}{2\pi r L_Z} \left\langle \sum_{i=1}^N \delta(r - r_i) \right\rangle \quad (3.1)$$

where L_Z is the length of the simulation box in the Z dimension, r_i is the radial coordinate of the i th atom of one type, N is the total number of atoms of one type, $\delta(x)$ is the Dirac delta function, the angle brackets stand for time averaging of the trajectory.

The density profiles of the silanol oxygen in the OH, O pores and the methyl group in the CH₃ pore all have a broad peak centered around $r = 12$ Å. So the diameters of the pores are 24 Å although the surfaces of the pores are rough. In the OH pore, the density profiles

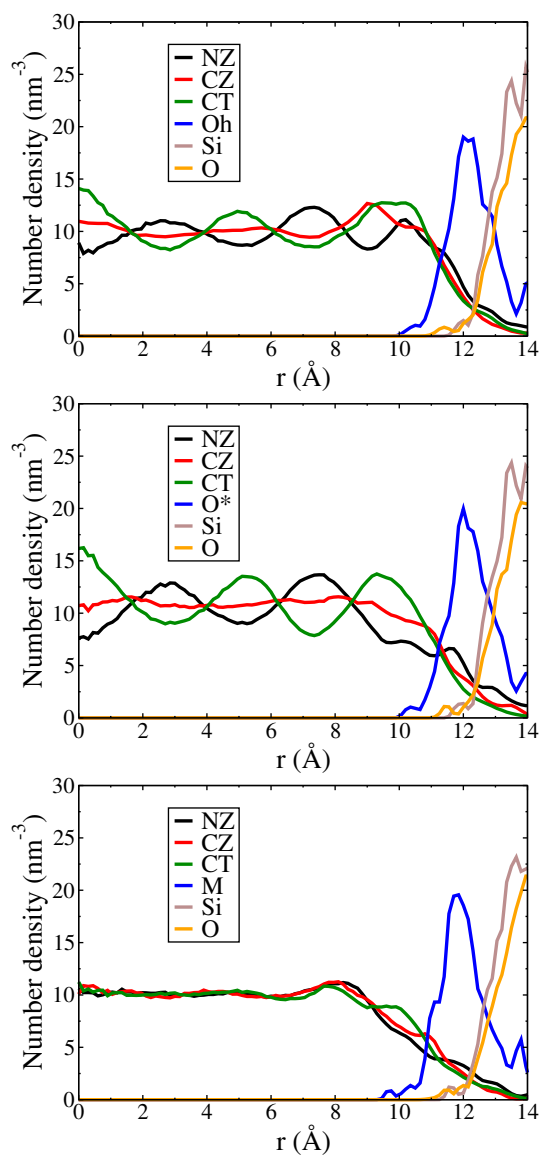


Figure 3.1: The number densities of different atoms plotted as a function of the radial distance from the center of the silica pore of diameter 24 Å. The top, middle and bottom panels depict the results for the OH, O, and CH₃ systems, respectively. Black, red, and green color are for the nitrogen, cyanide carbon, and methyl carbon of acetonitrile. Blue, silanol oxygen or surface methyl group; brown, silicon; orange, silica oxygen. The data for the silica oxygen are divided by two for better comparison.

of the nitrogen and methyl carbon atom of acetonitrile show oscillations with opposite phases that propagate from the interface to the center of the pore. The density of nitrogen is high where the density of methyl carbon is low and vice versa. Such patterns are also observed in acetonitrile near a flat hydroxylated silica surface.²⁸ The density profiles in the O pore are very similar to those in the OH pore, except the first peaks near the interface are muted for the nitrogen atom and the cyanide carbon atom. Removing the hydrogen bond interaction between the acetonitrile nitrogen and the silanol hydrogen does not change the structure of acetonitrile much, in agreement with the study of Morales *et al.*²⁶ The local structure near the surface has some change when acetonitrile can not make hydrogen bonds with the surface hydroxyls in this fictitious setup. In the CH₃ pore, the oscillations in density profiles are almost completely damped and the density is homogeneous in the center region of the pore.

The strong propagating oscillations result from preferential orientation induced by the surfaces and dipole pairing between acetonitrile molecules, that will be discussed further in later sections.

3.1.2 Orientational profile of acetonitrile

The orientational profile of the acetonitrile molecules as a function of the distance from the center of the pore is shown in Figure 3.2. This property is computed as follows. Cylindrical coordinates, $(\mathbf{r}_i^{com}, z_i)$, are utilized to describe the position of the center of mass of the i th acetonitrile molecule in the silica pore, and to define \mathbf{u}_i as the unit vector pointing from the C atom to the N atom in the CN group of the i th acetonitrile molecule. Then $(\mathbf{u}_i \cdot \mathbf{r}_i^{com}) = \cos \theta_i$, has a positive value when the nitrogen atom of the CN group is pointing towards the silica surface. The quantity calculated in Figure 3.2 is the two dimensional

histogram corresponding to the normalized orientational density

$$F(r, \cos \theta) = \frac{1}{2\pi r L_Z} \left\langle \sum_{i=1}^N \delta(\cos \theta - \cos \theta_i) \delta(r - \|\mathbf{r}_i^{com}\|) \right\rangle. \quad (3.2)$$

From the orientational distribution, one can develop a clear picture of the structure of acetonitrile in the silica pore. The ordering and layering of acetonitrile is present in both the hydrogen-bonded (OH) and non-hydrogen bonded (O) cases. The acetonitrile molecules closest to the surface form a sub-layer ($0.95 \text{ nm} < R < 1.20 \text{ nm}$), with their nitrogen atom pointing toward the surface. The acetonitrile molecules form a second sub-layer ($0.75 \text{ nm} < R < 0.95 \text{ nm}$) that is oriented anti-parallel to the first sub-layer, with their methyl end pointing toward the surface. Anti-parallel dipole pairings are also found in the bulk acetonitrile⁵⁶ although they possess transient lifetimes. At hydrophilic surfaces, the attraction of the first sub-layer to the surface further orders the pairings in the second sub-layer. This anti-parallel bilayer picture has been postulated in previous studies based on optical Kerr experiments,²⁰ vibrational sum frequency generation experiments,²⁹ and has been observed in recent simulations.^{26,28,29} The anti-parallel bilayer structure also occurs in propionitrile proximate to a flat hydroxylated silica surface.⁶³ Essentially the same picture is found in the present simulation. The anti-parallel layering effect propagates into the center of the pore for the OH case and the O case. However, the anti-parallel bilayer ordering is not present near the methylated surface (CH₃). Instead, acetonitrile molecules lie parallel to the surface when it is close to the methylated surface.

In comparison, according to Milischuk and Ladanyi's work, water is weakly ordered near the hydroxylated silica surface and the ordering does not propagate further into the water as does the ordering of acetonitrile. Acetonitrile can only act as an acceptor when it makes a hydrogen bond with silanol group, while water can act as both an acceptor and a donor. Thus near the surface, the nitrogen end of the acetonitrile is strongly preferred by the silanol groups, while the oxygen and the hydrogen sites of water are both preferred by the silanol groups. In addition, water can form tetrahedral networks while acetonitrile

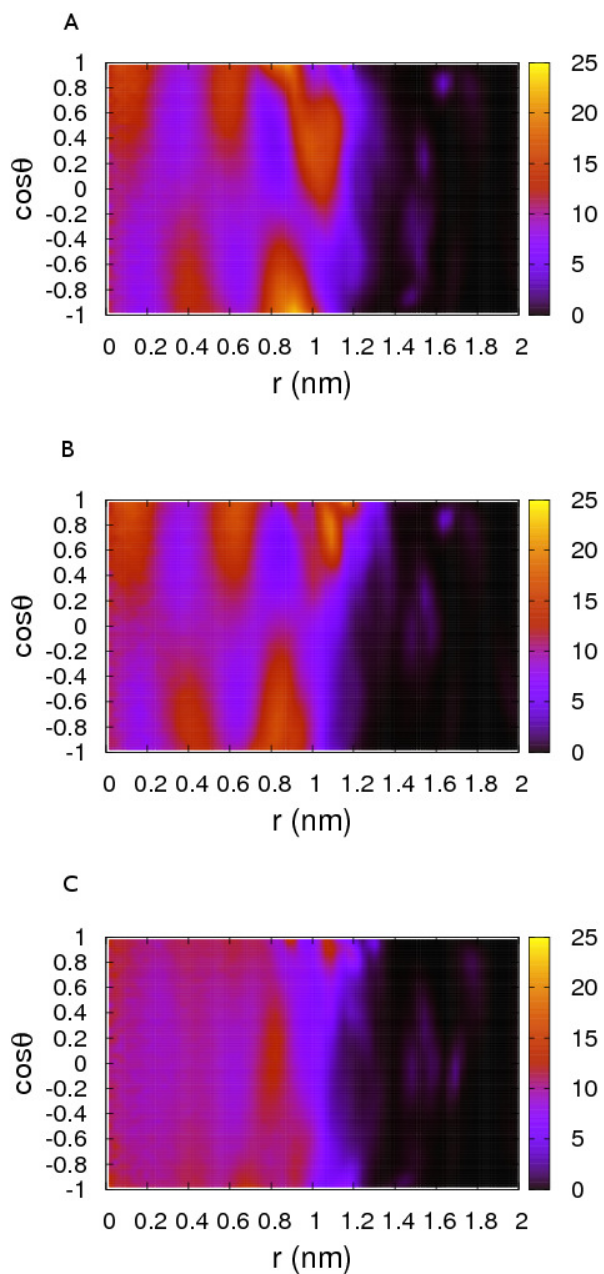


Figure 3.2: The orientational density distribution $F(r, \cos \theta)$ as defined in the text. Panels A, B, and C depict the distribution computed from the OH, O, and CH3 pores of diameter 24 Å, respectively.

exhibits dipole pairing that is more unidirectional and this surface templated ordering is not observed in water.

3.1.3 Charge density profile and hydrogen bond effect

In order to better understand the origin of the anti-parallel bilayer ordering, the charge density profiles of acetonitrile and silica surface are calculated as a function of the distance from the center of the pore, according to the following equation

$$\rho_q(r) = \frac{1}{2\pi r L_Z} \left\langle \sum_{i=1}^N q_i \delta(r - r_i) \right\rangle \quad (3.3)$$

where q_i is the partial charge of the i th atom that belong to acetonitrile or silica, N is the total number of atoms belong to acetonitrile or silica, and the meaning of other symbols have been introduced in Eq 3.1.

From the results shown in Figure 3.3, it can be seen that there is a significant surface dipole on the functionalized surface in both the OH and the O cases. Such surface charge distributions induce the anti-parallel dipole pairing and layering of the acetonitrile. In contrast for the methylated case, the surface charge is much smaller and thus the ordering of the acetonitrile is significantly muted. Both the OH surface and the O surface exhibit similar long range electrostatic effects on acetonitrile, this is in agreement with the work of Morales *et al.*²⁶ where it was found that the structure and orientation of acetonitrile in the pore is insensitive to specific hydrogen bonding interactions.

As one might expect, hydrogen bonding interactions give rise to some differences in the structure and orientation of the acetonitrile molecules nearest to the surface. The radial density functions between the atoms on the acetonitrile molecules and the silanol oxygen atoms are shown in Figure 3.4 for the OH surface and the O surface respectively. Here NZ, CT and CZ designate the nitrogen atom, the methyl carbon atom, and the cyanide carbon atom of the acetonitrile molecule, respectively. OH designates the oxygen atom of

the hydroxyl group on silica surfaces. The radial distribution functions have been properly renormalized utilizing the method of Soper *et al.*^{58,59} to account for the excluded volume effect of the confined geometry. The nitrogen peak is much higher and its position is closer to the oxygen in the OH case. One can see that the acetonitrile near the silanol groups are more structured in the presence of hydrogen bonding. Also it can be seen in Figure 3.2, that the acetonitrile molecule in the nearest sub-layer to the surface points almost perpendicular to the surface with its nitrogen end towards the O-functionalized silica pore, but is more tilted in the OH functionalized pore. This is consistent with the “bent” geometry necessitated by the formation of a hydrogen bond in the OH case. As will be shown in Section 3.2.1, specific hydrogen bonding interactions have a greater impact on dynamical properties.

In addition, we have attempted to compute the contact angle of acetonitrile with the flat hydroxylated and methylated silica surface. This work was prompted by recent experimental measurements of the contact angle for acetonitrile across numerous modified silica interfaces.⁶⁴ These experiments found that acetonitrile forms relatively low contact angles with the surface and show only slight dependence on the functionalization. According to the experiments, the contact angle of acetonitrile on the methylated silica surface is 12° while the contact angle of water on the same surface is 96° . The methylated surface is hydrophobic in water since the interactions between water molecules are strong enough that water molecules prefer to associate rather than be next to the methylated surface. In contrast, the methylated surface is not solvophobic in acetonitrile since acetonitrile molecules are amphiphilic and their interaction with each other is not significantly stronger than their interactions with the methylated surface. This difference in self-association is also reflected in the fact that the surface tension of acetonitrile is about 2.5 times smaller than the surface tension of water.⁶⁵ Owing to the affinity between acetonitrile and silica surfaces, all the differently functionalized surfaces are almost entirely wetted by acetonitrile in our simulations

and the contact angle is too small to be determined without ambiguity.

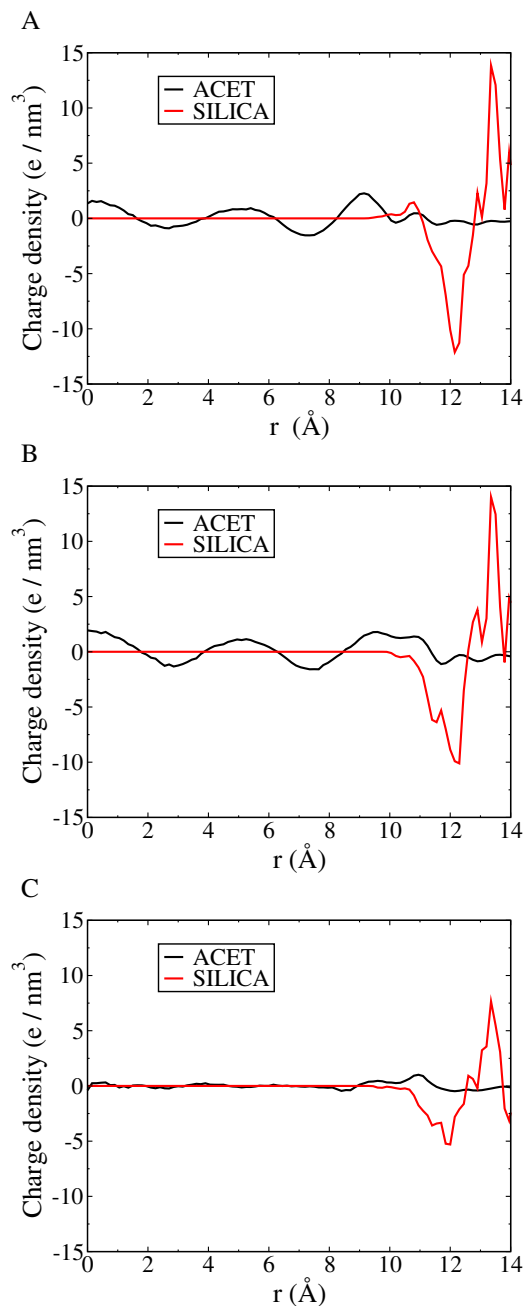


Figure 3.3: The charge density of acetonitrile (black) and silica (red) plotted as a function of the radial distance from the center of the silica pore of diameter 24 \AA . Panels A, B, and C are for the OH, O, and CH3 systems, respectively.

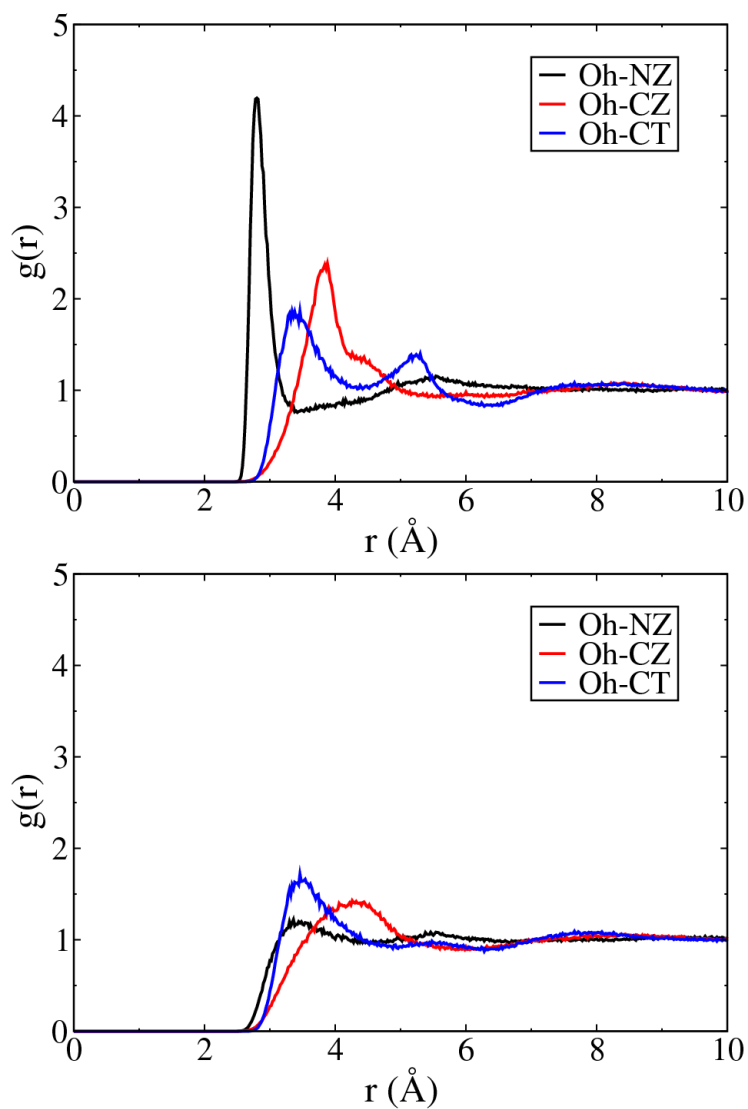


Figure 3.4: The radial distribution function (RDF) of various species in the OH (top panel) and O (bottom panel) pores of diameter 24 Å. The black line is the RDF between the oxygen atoms of silanols and the nitrogen atoms of acetonitrile. The red line is the RDF between the oxygen atoms of silanols and the cyanide carbon atoms of acetonitrile. The blue line is the RDF between the oxygen atoms of silanols and the methyl carbon atoms of acetonitrile.

3.1.4 Structure of acetonitrile in a larger pore

Figure 3.5 depicts the orientational density distribution $F(r, \cos \theta)$ of acetonitrile in the hydroxylated pore of diameter 44 Å. As in the hydroxylated pore of diameter 24 Å, an antiparallel bilayer structure is formed near the surface ($1.7 \text{ nm} < R < 2.15 \text{ nm}$). The antiparallel layering can propagate into the acetonitrile for at least 1.75 nm ($0.4 \text{ nm} < R < 2.15 \text{ nm}$), and there is still some trace of layering in the very center of the pore ($R < 0.4 \text{ nm}$). This is consistent with the finding in Hu *et al.*'s work²⁸ that the antiparallel layering effect can propagate for 2 nm in acetonitrile near a flat hydroxylated crystal silica surface.

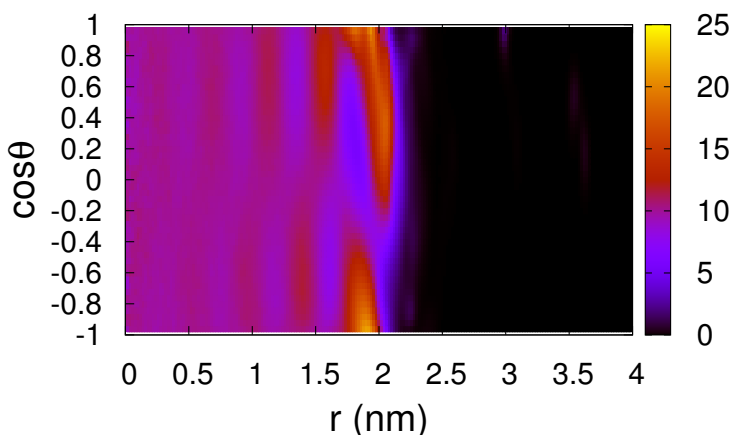


Figure 3.5: The orientational density distribution $F(r, \cos \theta)$ as defined in the text for the acetonitrile in the hydroxylated silica pore of diameter 44 Å.

The charge density profiles of acetonitrile in the two hydroxylated pores of different sizes are compared in Figure 3.6. The data for the 24 Å pore has been shifted to the right by 10 Å. The positions and intensities of the charge density oscillations are similar for the first two cycles away from the surfaces in the two different pores. But at the third peak position, which also corresponds to the center of the pore of diameter 24 Å, the charge

density in the 24 Å pore is more than three times of that in the 44 Å pore. This enhanced density signifies that there is an in-phase construction between layering induced by the two symmetrical sides of the pore of diameter 24 Å. Such in-phase construction or out of phase destruction could manifest in the pores of small sizes, since the layering does not phase out in the center of small pores.

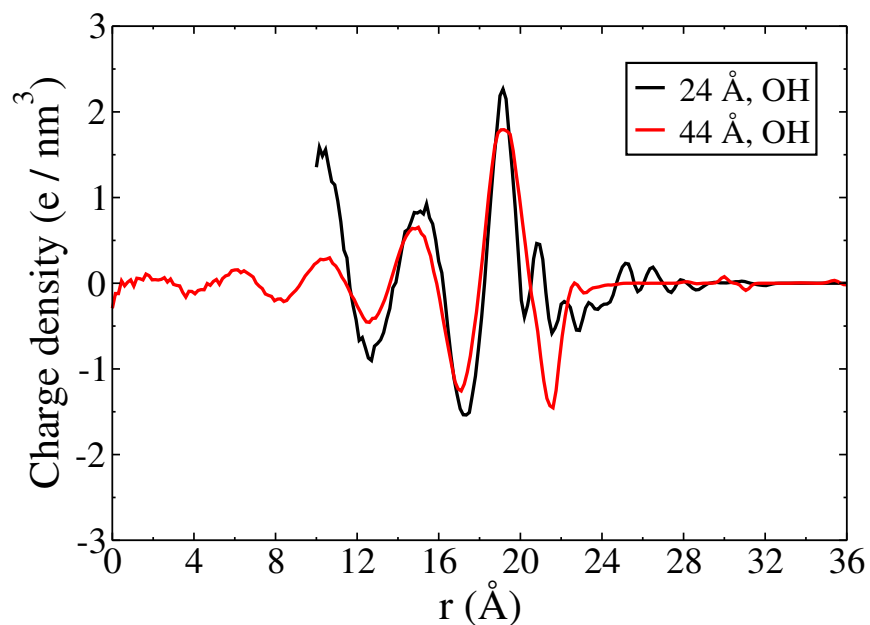


Figure 3.6: The charge density of acetonitrile in two hydroxylated silica pores of diameters 24 Å and 44 Å. The red curve is for the 44 Å pore. The black curve for the 24 Å pore has been shifted to the right by 10 Å in order to better compare the behavior at the silica-acetonitrile interface.

3.2 Two Population Dynamics

Experimental studies using the OKE²⁰ and NMR²¹ techniques show that the dynamics of acetonitrile near the pore surface is frustrated compared to its bulk-like behavior near the pore center. While geometrical confinement effects provide the main contribution to

the frustrated dynamics of weakly wetting liquids,⁶⁶ the attractive interactions with the pore surfaces dominate in the frustrated dynamics of strongly wetting liquids.^{20,67} We find that specific hydrogen bonding plays a dominant role in engendering the frustrated dynamics of acetonitrile in the silica pore functionalized with silanol groups, particularly with respect to orientational relaxation. The distinctive dynamics of acetonitrile near the OH pore wall and in the pore center make it necessary to use a two population exchange model in order to explain the the total singlet reorientational dynamics. Our study on reorientational dynamics of acetonitrile in silica pores shows great consistency with OKE experimental studies.^{20,67}

3.2.1 Singlet reorientational dynamics and hydrogen bond effect

The singlet reorientational time correlation functions are calculated separately for the center and surface populations of acetonitrile. The surface population contains acetonitrile molecules in the two anti-parallel sublayers near the silica surface (the rightmost two sublayers as shown in Figure 3.2A), and the center population contains acetonitrile molecules far from the surface (the leftmost three sublayers in Figure 3.2A). This division between the two populations is also shown in Figure 3.7. The center of mass position is used in classifying which region an acetonitrile molecule belongs to. Since the two populations exchange with each other by self-diffusion, it is necessary to include the survival probabilities for each population in the calculation of their reorientational correlation functions. The prescription for calculating population specific singlet time correlation functions has already been presented¹ and is expressed in the following equation,

$$C_1(t) = \frac{1}{T} \sum_{t_0=1}^T \frac{1}{N(t_0, t_0+t)} \sum_{i \in \mathcal{S}(t_0, t_0+t)} \mathbf{u}_i(t_0) \cdot \mathbf{u}_i(t_0+t), \quad (3.4)$$

where $\mathcal{S}(t_0, t_0+t)$ is the set of molecules that stay in the layer continuously from time t_0 to t_0+t , $N(t_0, t_0+t)$ is the number of molecules in the set $\mathcal{S}(t_0, t_0+t)$, \mathbf{u}_i is a unit vector

pointing from the nitrogen atom to the methyl carbon atom on the i th molecule.

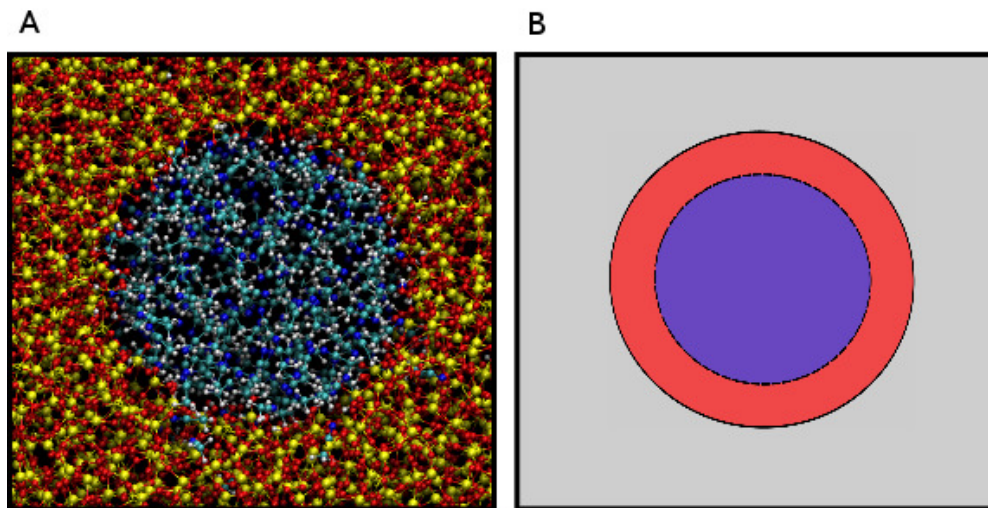


Figure 3.7: (A) A snapshot of the silica pore of diameter 24 Å filled with acetonitrile, taken looking down the axis of the cylindrical pore. (B) A schematic representation of the division of the acetonitrile into two populations. Red indicates the surface population and blue indicates the center population.

We note that in previous simulation studies, (a) either the dynamic properties were reported for the total population,²⁶ (b) the population specific dynamic properties were calculated in a way that neglects the exchange between different regions,³⁰ or (c) only for molecules that stayed in a prescribed region for a time equal to the maximum correlation time computed.^{28,29} Approach (b) can cause problems when the exchange between different populations is faster than the decay of the time correlation functions being calculated. Approach (c) yields error bars that grow larger even at very short times as the maximum correlation time studied is increased, since the population averaged over will become vanishingly small.

The results calculated for the three different systems of diameter 24 Å are shown in Figure 3.8A. The time correlation function (TCF) $C_1(t)$ for bulk acetonitrile is also shown.

Unlike bulk acetonitrile, the TCFs of acetonitrile in the three pore systems decay to nonzero plateaus, no matter whether they are for the surface populations or the center populations. While we observe that when the silica surface is made purely repulsive, the TCFs (not shown) in the two populations both decay to zero. The difference lies in the ordering and layering effect by the somewhat rugged silica surface and the surface heterogeneity shown in our small system size. The acetonitrile molecules in the surface population are ordered by their interaction with the silica surface. Although the surface layer has approximate cylindrical symmetry, the probability that one acetonitrile can change its orientation significantly by moving along the surface without leaving the surface layer is small, so that to relax their orientations such molecules must exchange with populations that are further away than the correlation length of orientational pair correlations. Thus in the pores we observe a plateau at long times in the population specific TCFs for the surface population. The TCFs for the center populations in the three models are very similar to each other, however they also decay to a plateau (of value 0.11), either because the pore radius is not large compared to the above mentioned correlation length, or more likely because our constructed heterogeneous silica surfaces happen to have unbalanced charge distributions in the Y direction. As a result, the acetonitrile has an average preferential orientation in the Y direction ($\langle \mathbf{u}_Y \rangle = 0.3$). In Section 3.2.4, we show that these plateaus for the center population disappear in larger sized pores.

The plateau values in the TCFs for the surface populations of the OH and O models are much greater than for the CH3 model, where the ordering of acetonitrile is muted. The much less frustrated dynamics in the CH3 model demonstrate that the attractive interactions with the pore surfaces dominate the frustrated dynamics of strongly wetting liquids. Loughnane *et al.* also made this point based on the faster reorientational decay observed in OKE experiments when they methylated the silanol groups on the pore surfaces.^{20,67} Moreover, hydrogen bonding interactions give rise to the frustrated short and intermedi-

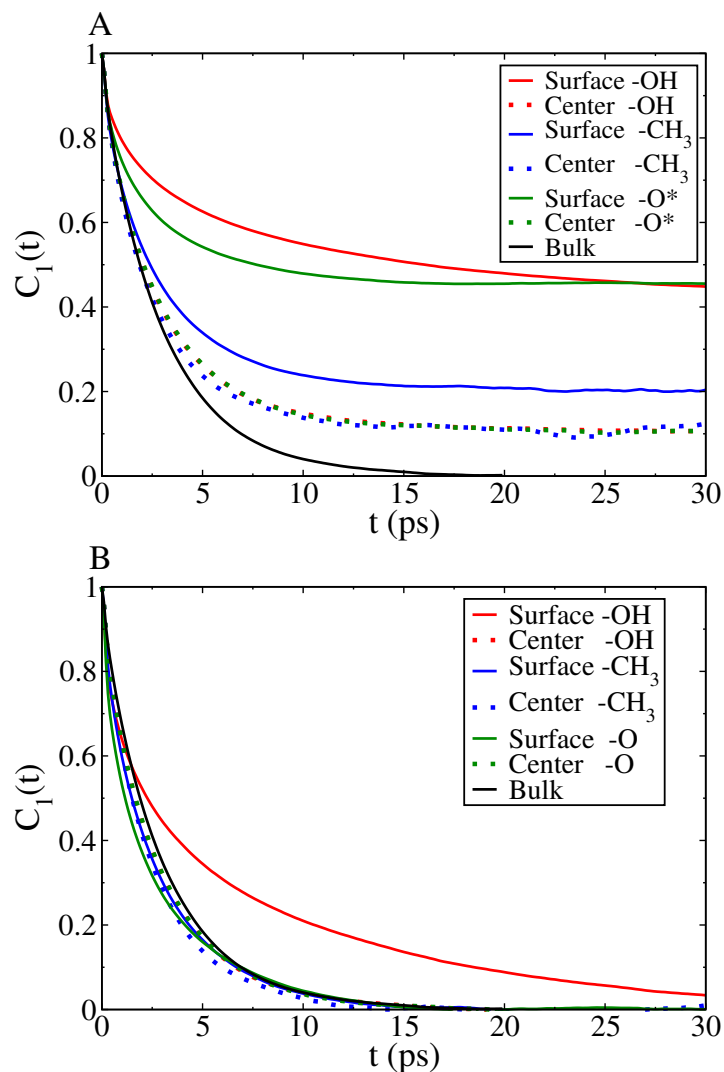


Figure 3.8: (A): The singlet reorientational time correlation function of acetonitrile in different regions in the OH, CH₃ and O of diameter 24 Å. (B): The time correlation function of the fluctuations in the singlet orientation obtained by first subtracting the plateau value, and then renormalization the results shown in panel A. The red, blue and green colors indicate the OH, CH₃ and O pores, respectively. Black is for the bulk. The solid and dotted lines are for the surface population and the center population, respectively.

ate time orientational relaxation. This is not so obvious in Figure 3.8A, as the long time plateau values are different. To make this point clearer, the TCFs of the fluctuations in the singlet orientation are obtained by renormalization of the $C_1(t)$ after subtracting the corresponding long time plateau values. From the results shown in Figure 3.8B, the relaxation of the fluctuations in the singlet orientation is greatly retarded and non-exponential only in the surface population of the OH system where the hydrogen bonding is present. The relaxation in other populations are close to the exponential relaxation of the bulk. The bulk relaxation (black curve) can be fit by an exponential function $\exp(-t/\tau_b)$ with $\tau_b = 2.87\text{ps}$. The relaxation in the surface population of the OH model (red curve) can be fit by a stretched exponential function $\exp(-(t/\tau)^\alpha)$ with $\tau = 4.41\text{ps}$ and $\alpha = 0.577$. Although the structures of liquid acetonitrile are similar for the OH and O systems, the relaxation decay of the surface populations for these two systems are quite different, as is indicated in Figure 3.8B. This finding underlines the indispensable role that hydrogen bonding interactions play in governing the dynamical properties of acetonitrile near the hydroxylated surface.

3.2.2 Two population exchange model

Loughnane *et al.* proposed a two-population exchange model for the collective reorientation dynamics of acetonitrile confined in hydroxylated nanoporous glasses.²⁰ In their model, acetonitrile molecules in silica pores partition into two distinct populations with different reorientation time scales, the bulk-like center population and the retarded surface population. The exchange between two populations provides the surface population another channel for reorientational relaxation. In our simulation, we find, as described above, the existence of two populations with different reorientational dynamics. The exchange between two populations can be well described via the survival probabilities in different

regions,

$$S(t) = \frac{1}{T} \sum_{t_0=1}^T \frac{N(t_0, t_0+t)}{N(t_0)} \quad (3.5)$$

where $N(t_0, t_0+t)$ is the number of molecules stayed in the region continuously from time t_0 to t_0+t , and $N(t_0)$ is the number of molecules in the region at time t_0 . Based on the idea of Loughnane et al., we provide an ansatz to reconstruct the TCF of the total population in our OH pore with three functions, the population specific TCFs of the two populations (introduced in Section 3.2.1) and the survival probability of the surface population. Our approximate formula for the total TCF $C_{1T}(t)$ is,

$$C_{1T}(t) = \chi_c C_{1C}(t) + \chi_s S(t) C_{1S}(t) + \chi_s (1 - S(t)) C_{1C}(t), \quad (3.6)$$

where $C_{1C}(t)$ and $C_{1S}(t)$ are the TCFs of the center population and surface populations respectively, $S(t)$ is the survival probability of acetonitrile in the surface population, χ_c is the fraction of molecules in the center population, and $\chi_s = 1 - \chi_c$ is the fraction of molecules in the surface population. χ_c was found to be 0.405 from our simulation data by counting numbers of molecules, while Loughnane *et al.* found this parameter to be 0.39 at 309K by fitting their model to optical Kerr spectroscopy data.²⁰ As noted in previous sections, the diameter of our pore is the same as that in Loughnane et al.'s work.²⁰ The boundaries of our surface population were determined from the density profile of acetonitrile and were set to contain the acetonitrile molecules in the two antiparallel sublayers. The thickness of the surface layer was found to be 4.5Å in our case, while this value derived from Loughnane and co-workers' model of OKE data is 4.7Å.²⁰ The first term in Eq 3.6 accounts for the reorientation of the molecules that are initially in the center population, and we assume that the initial orientation of these molecules has been fully relaxed before they enter the surface population. The second term accounts for the reorientation of the retarded molecules that stay continuously in the surface population from time 0 to t . The third term accounts for the process by which some of the retarded molecules initially in the surface population

can reorient further by exchanging with the center population. The total TCF $C_{1T}(t)$ approaches the plateau value 0.11 after 100ps, which is also the plateau value of $C_{1C}(t)$. The total TCF can be fit by the function $A + (1 - A)\exp(-(t/\tau)^\alpha)$ with $A = 0.114$, $\tau = 4.87\text{ps}$ and $\alpha = 0.517$. The approximated total TCF (red dot line) from our two-population model was compared with the total TCF calculated by definition (red line) in Figure 3.9. The small difference between the two shows us that the two-population model is successful at describing singlet reorientational dynamics of acetonitrile confined in the hydroxylated silica pore. Our molecular dynamics simulation provides the first support for Loughnane et al.'s two-population exchange model²⁰ from molecular simulation.

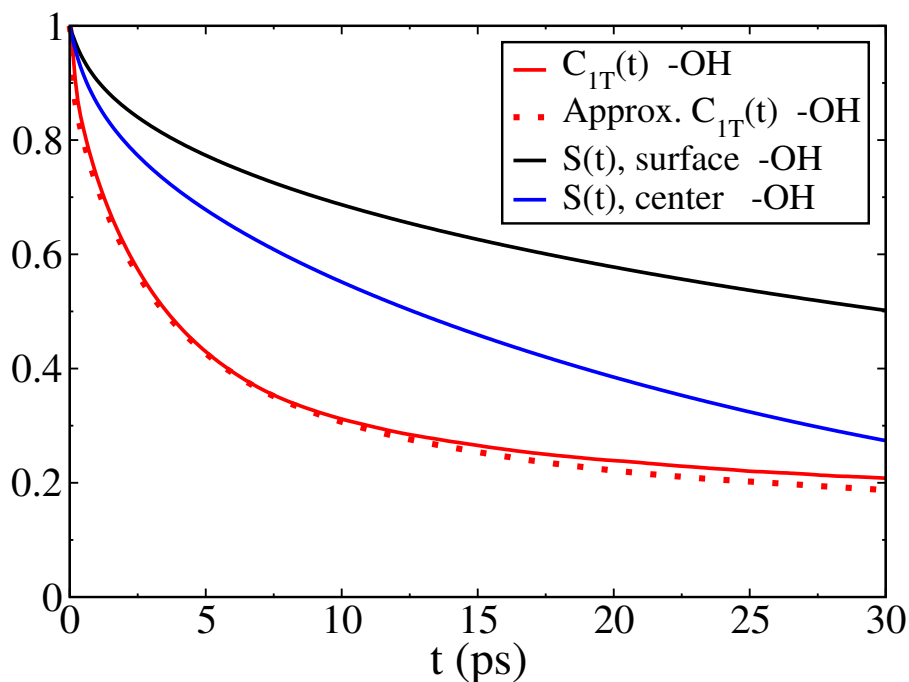


Figure 3.9: The singlet reorientational time correlation function of the total population in the OH pore of diameter 24 Å as calculated by definition (red solid line) and approximated by our two-population model (red dotted line). The survival probabilities of acetonitrile in the surface population (black line) and the center population (blue line) of the OH pore of diameter 24 Å.

3.2.3 Parallel diffusion

The translational diffusion constant has not been reported in simulation studies of acetonitrile near silica interfaces or in silica nanopores.^{26,28,29} Calculating the diffusion tensor in inhomogeneous liquid is not simple, Liu *et al.*¹ have an excellent treatise on this topic. An application of this method in cylindrical symmetry is detailed in Section 3.4. For the parallel diffusion, mean square displacements taking into account the survival probability have been used to compute the diffusion constant parallel to the water-vapor interface in Liu *et al.*'s work.¹ To study the diffusion parallel to the axis of the cylindrical pore (Z axis) in the surface population and the center population, the mean square displacement taking into account of the survival probability is calculated from the following expression,¹

$$MSD_{1Z}(t) = \frac{1}{T} \sum_{t_0=1}^T \frac{1}{N(t_0, t_0+t)} \sum_{i \in \mathcal{S}(t_0, t_0+t)} (Z_i(t_0+t) - Z_i(t_0))^2 \quad (3.7)$$

where $N(t_0, t_0+t)$ and $\mathcal{S}(t_0, t_0+t)$ share the same meaning as those in Eq 3.4. The results for the three pores of diameter 24 Å are plotted in double logarithmic scale in Figure 3.10.

For times greater than 1 ps, the MSDs in the center populations enter the Brownian diffusion regime and they are very close to the MSD in the bulk system. In contrast, the MSDs in the surface populations exhibit sub-diffusive behavior for times greater than 1ps. The sub-diffusive MSDs could be fit by a power-law relationship $MSD_{1Z} = (2K_\alpha/\Gamma(1+\alpha))t^\alpha$ derived from fractional diffusion equation⁶⁸ with α being 0.55, 0.55 and 0.76 for the OH, O and CH3 model respectively. $\Gamma(z)$ is the gamma function $\Gamma(z) = \int_0^\infty t^{z-1} e^{-t} dt$. The generalized diffusion coefficients K_α are $0.309\text{Å}^2/\text{ps}^{0.55}$, $0.413\text{Å}^2/\text{ps}^{0.55}$ and $0.605\text{Å}^2/\text{ps}^{0.76}$ for the OH, O and CH3 systems, respectively. Unlike the water-vapor interface in Liu *et al.*'s work,¹ the acetonitrile molecules in our case are attracted to specific sites on the rough and heterogeneous acetonitrile-silica interfaces. The sub-diffusive behavior could emerge when an acetonitrile travels on such a complex energy landscape on the surface, just like the sub-diffusion found in experiments when colloidal tracer particle travels in F-

actin networks.⁶⁹ The sub-linear power-law relationship in similar systems was also found in Rodriguez *et al.*'s work⁶¹ where they studied dynamics of the acetonitrile component of acetonitrile-water mixture in silica nanopores and in Gallo *et al.*'s work^{70,71} where water confined in silica nanopores was studied. The mean square displacement in the bulk system shown in Figure 3.10 gives the diffusion constant $D_{bulk} = 0.528 \text{ \AA}^2/\text{ps}$, while the value reported in one experimental study was $0.434 \text{ \AA}^2/\text{ps}$.⁷² In the center populations of our three models, diffusion constants parallel to the Z axis are within a 10 percent range of the bulk value.

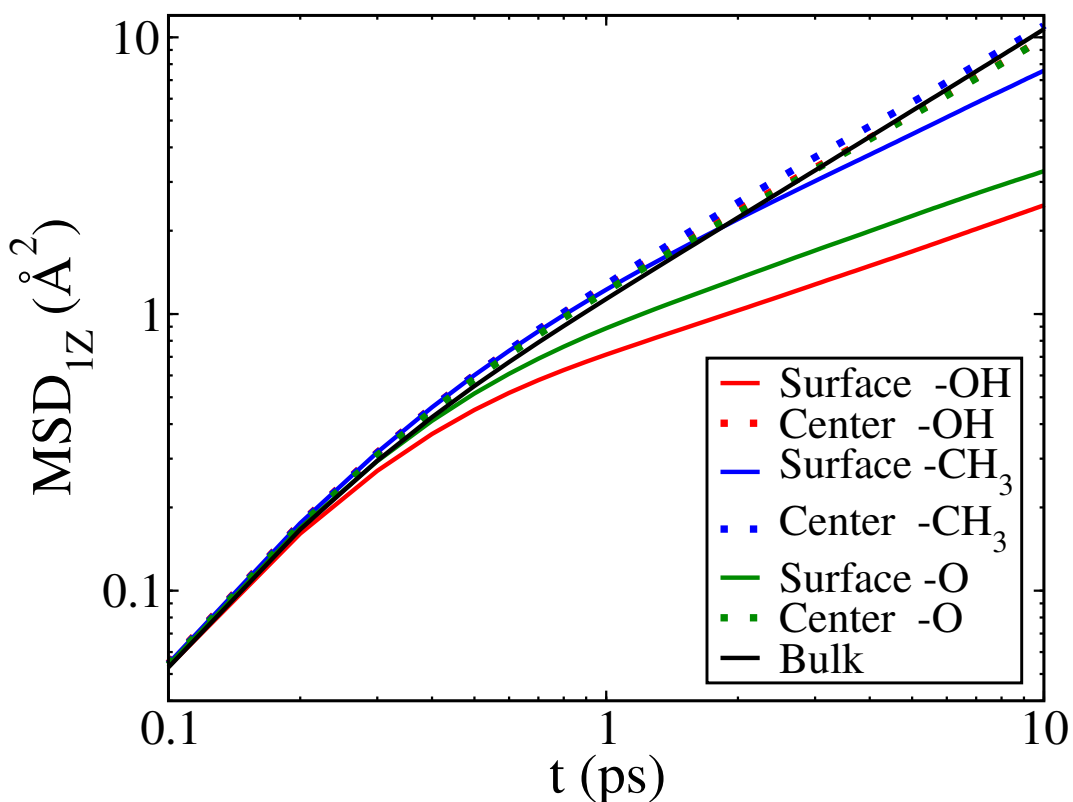


Figure 3.10: The mean square displacements of acetonitrile in different regions in the OH, CH₃ and O pores of diameter 24 Å. The red, blue and green colors are for the OH, CH₃ and O pores, respectively. The solid and dotted lines are for the surface population and the center population, respectively. Black indicates the behavior of the bulk acetonitrile.

The diffusional behavior of the surface population is described by two constants, K_α and α , instead of by the one diffusion coefficient needed for the bulk liquid. Diffusion in the surface populations can be compared qualitatively by direct comparison of the magnitude of the MSDs at 10ps instead of by comparing the values of (K_α, α) alone. As we see in Figure 3.10, diffusion along the Z direction of acetonitrile molecules near the surfaces is slowed down significantly in the OH and O systems, and is roughly 80% slower than in the bulk liquid. While the same motion is slowed down by only 35% in the surface population of the CH3 system. This shows that hydrophilic surfaces can strongly hinder the translational motion of acetonitrile in the two antiparallel sub-layers next to the surfaces. This hindrance is reduced greatly at less attractive hydrophobic surfaces.

3.2.4 Dynamics of acetonitrile in a larger pore

The dynamical properties of acetonitrile in the two different sized hydroxylated pores are compared in Figure 3.11. The singlet orientational TCFs and the MSDs calculated by our survival probability method are almost the same for the surface population in the two pores. As expected surface heterogeneity has a smaller effect in the larger pore because part of the center population is further from the surface. Thus the TCF for the center population in the larger pore decays to zero instead of approaching the 0.11 plateau in the smaller pore. However, the TCFs for the center populations would be nearly the same if the 0.11 plateau is subtracted from the TCF of the smaller pore, and the result is renormalized. The diffusion constant of the center population in the axial direction is $0.585 \text{ \AA}^2/\text{ps}$ for the larger pore, which is greater than the $0.470 \text{ \AA}^2/\text{ps}$ value for the smaller pore. This is because the center population in the larger pore contains more acetonitriles that are less influenced by the propagating layering effect. The center population in the smaller pore contains three sublayers that are still ordered considerably by the propagating layering effect. Besides these sublayers, the center population in the larger pore contains five more sublayers that

are weakly ordered. If we only include the molecules in the three more ordered sublayers of the center population in the larger pore, then the diffusion constant for this population is $0.500 \text{ \AA}^2/\text{ps}$, which is closer to the $0.470 \text{ \AA}^2/\text{ps}$ value for the smaller pore.

We also tested the two-population model for the total reorientational TCF in the larger pore. The fraction of molecules in the center population χ_c changes to 0.60. This parameter was found to be 0.61 in the OKE experiments for the hydroxylated silica pore of diameter 44 \AA at 309K.²⁰ The three functions used in the construction of the total TCF are shown in Figure 3.12. As shown in Figure 3.12, the total TCF constructed by this model is very close to the total TCF calculated by definition.

From the above comparisons, we conclude that the population specific dynamical properties of acetonitrile have little dependence on the size of the pore, except for the diffusion of the center population in the axial direction. This conclusion may not hold for very small pore sizes around 10 \AA . For the hydroxylated pores of diameter 44 \AA , the observed faster reorientational dynamics of the total population in the larger pore is mainly due to the larger fraction of molecules in the center population, and not from changes in the reorientational dynamics in each separate population (surface and center). In Loughnane et al.'s experimental study,²⁰ the OKE data was fit by a sum of three exponentials. It was found that the fitted time constants are the same for two different sized hydroxylated silica pores. Our conclusion is consistent with this finding.

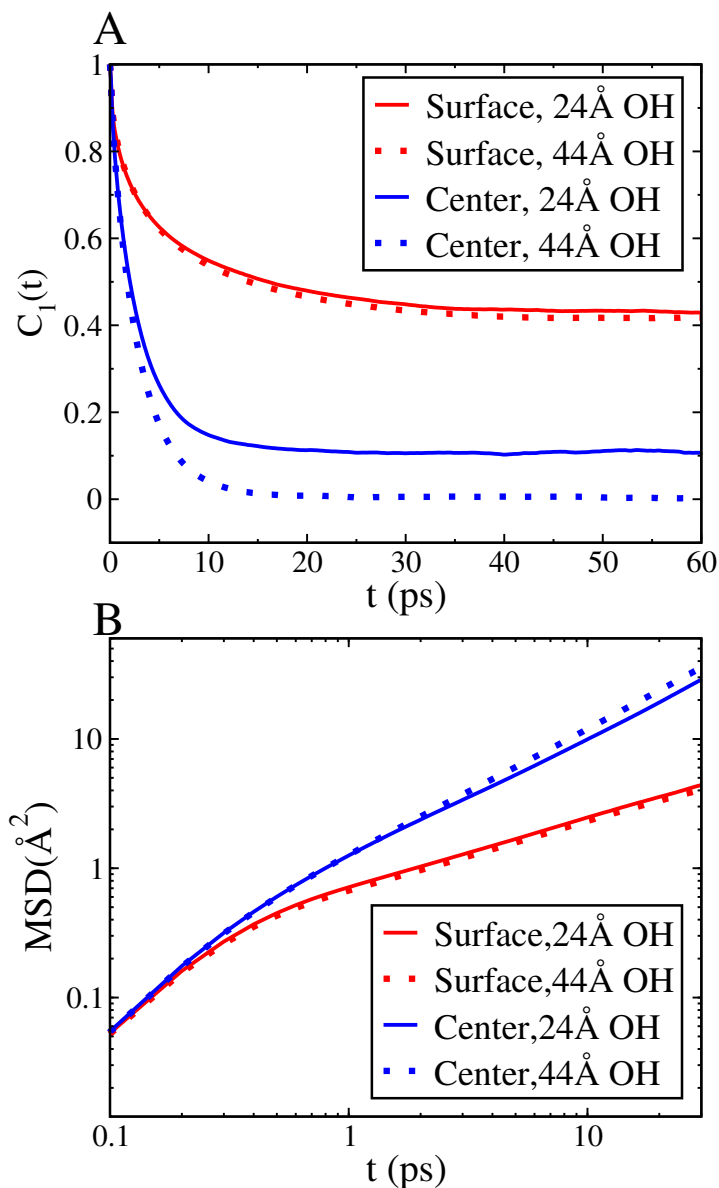


Figure 3.11: The dynamical properties of acetonitrile in two hydroxylated pores of diameters 24 Å and 44 Å calculated by the survival probability method for the surface population and the center population. Panel A depicts the singlet reorientational time correlation functions. Panel B shows the mean square displacements. The red and blue curves depict the the surface population and the center population, respectively. The solid and dotted lines indicate the 24 Å pore and the 44 Å pore, respectively.

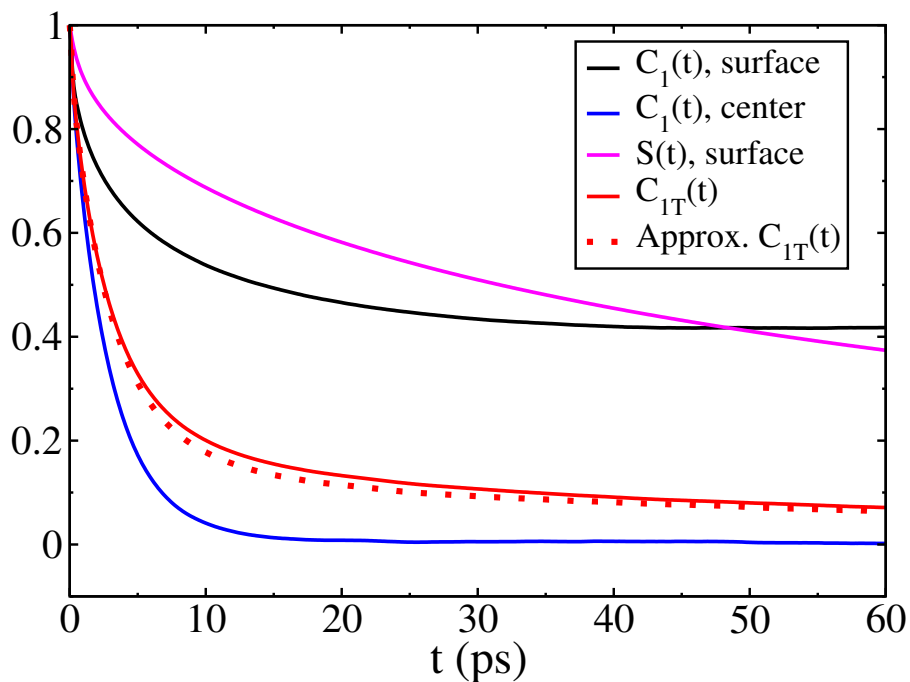


Figure 3.12: The singlet reorientational time correlation function of the total population for the acetonitrile in the hydroxylated pore of diameter 44 Å as calculated by definition (red solid line), and approximated by our two-population model (red dotted line). Also shown are the three functions used in the two-population model: the survival probability of acetonitrile in the surface population (magenta line), the singlet reorientational time correlation functions for the surface population (black line) and the center population (blue line) calculated by the survival probability method.

3.3 Comparison of Two Analysis Methods

In a previous study of the population specific dynamical properties,³⁰ molecules are considered to belong to one population for all times if their initial positions were in the specific region at a reference time. In this way, the population specific singlet orientational TCF is calculated by the following equation,

$$C_1^*(t) = \frac{1}{T} \sum_{t_0=1}^T \frac{1}{N^*(t_0)} \sum_{i \in \mathcal{S}^*(t_0)} \mathbf{u}_i(t_0) \cdot \mathbf{u}_i(t_0 + t), \quad (3.8)$$

where $\mathcal{S}^*(t_0)$ is the set of molecules that were in the specific region at a reference time t_0 , $N^*(t_0)$ is the number of molecules in the set $\mathcal{S}^*(t_0)$.

The TCFs calculated by this initial position method and our survival probability method for the 24Å OH pore are shown in Figure 3.13A. The survival probabilities of the surface population and the center population are also shown. Although the methods yield similar results near $t = 0$, for intermediate times, the surface population TCF calculated by the initial position method decays faster than the one calculated by the survival probability method. Unlike the TCF computed by the survival probability method, it does not plateau on the intermediate time scale. Instead at long times it approaches the same plateau level as the TCF of the center population (not shown in figure). Clearly, the TCF for the surface population in the initial position method is actually a mixing of the TCFs for the surface population and the center population in the survival probability method, since the decay of the survival probability and the reorientation of the acetonitrile molecule are on a comparable time scale in the surface population. In the center population, the TCFs calculated by the two different methods are roughly the same, with the one computed via the initial position method decaying slightly slower on the intermediate time scale. The mixing in this case is negligible since the acetonitrile in the center population reorients much faster than it exchanges into the surface population.

In the initial position method, the mean square displacement along the axis of the cylin-

drical pore is calculated by the following equation,

$$MSD_{1Z}^*(t) = \frac{1}{T} \sum_{t_0=1}^T \frac{1}{N^*(t_0)} \sum_{i \in \mathcal{S}^*(t_0)} (Z_i(t_0+t) - Z_i(t_0))^2, \quad (3.9)$$

where $N^*(t_0)$ and $\mathcal{S}^*(t_0)$ share the same meaning as those in Equation 3.8.

The MSDs calculated by the two different methods for the 24Å OH pore are shown in a double logarithmic scale in Figure 3.13B. For the surface population, the MSDs calculated by the two different methods are the same for times less than 1 ps. For times greater than 1 ps, the MSD calculated by the initial position method deviates from the MSD of the survival probability method, with its slope increasing from 0.55 to 1. It exhibits Brownian diffusive behavior after 10ps. The diffusion constant is $0.175 \text{ \AA}^2/\text{ps}$, if linear fitting is applied in the time window from 10 ps to 30 ps. However, we note that after 10 ps more than 30% of the surface population has been exchanged into the center population. Thus, when it is calculated by the initial position method, the MSD of the surface population carries evident characteristics from the center population. Furthermore, the diffusion constant obtained is not invariant when fit in windows at later times, since the mixing of the two populations increases with time. On the other hand, the MSD of the surface population calculated by the survival probability method exhibits sub-diffusive behavior for times greater than 1 ps. The power-law fitting is stable until 80ps, after which the statistics get worse as the survival probability decays. For the center population, the MSDs calculated by the two different methods are similar and linear in time. The diffusion constants are $0.428 \text{ \AA}^2/\text{ps}$ and $0.470 \text{ \AA}^2/\text{ps}$, for the initial position method and the survival probability method, respectively, when fit from 2ps to 10ps. The diffusion constants change to $0.371 \text{ \AA}^2/\text{ps}$ and $0.473 \text{ \AA}^2/\text{ps}$, when fit from 10ps to 20ps. The diffusion constant decreases at later time in the initial position method since the mixing of the two population contaminates the results. The survival probability method does not exhibit these problems.

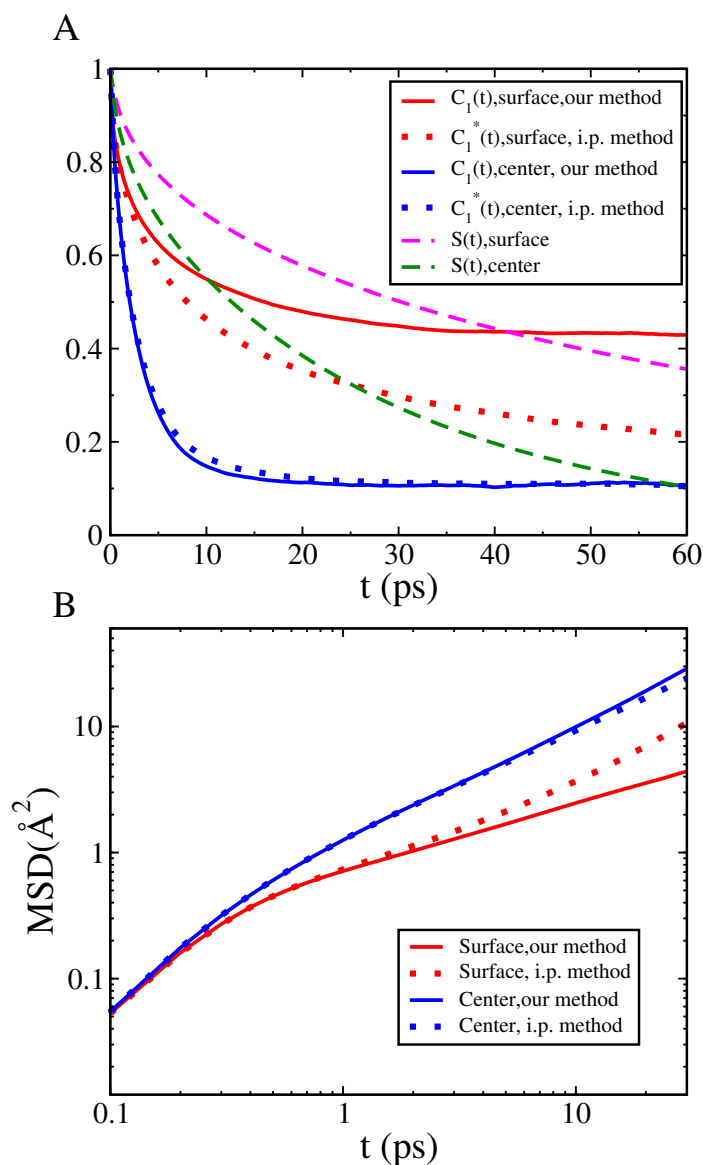


Figure 3.13: The dynamical properties of acetonitrile in the 24 Å OH pore calculated by two different methods. Panel A shows the singlet reorientational time correlation functions and the survival probabilities. Panel B depicts the mean square displacements. The red and blue colors indicate the surface population and the center population, respectively. The solid and dotted lines depict the results of the survival probability and the initial position method, respectively. The dashed magenta and green lines denote the survival probabilities of the surface population and the center population, respectively.

3.4 Diffusion Tensor Calculation of Liquids Confined in Cylindrical Pores

For uniform liquids, the Einstein relation $\langle \Delta r(t)^2 \rangle \sim 6Dt$ or the Green-Kubo relation $D = \frac{1}{3} \int_0^\infty dt \langle \mathbf{v}(t) \cdot \mathbf{v}(0) \rangle$ can be used to calculate the diffusion coefficients from molecular dynamics trajectories. The diffusion tensor could be position-dependent and anisotropic for liquids in confinement or at interfaces. The methods used to calculate diffusion coefficients for uniform liquids are not applicable for inhomogeneous liquids. Liu *et al.* developed a general method for calculating the diffusion tensor from molecular dynamics for liquids at interfaces.¹ In this method, the virtual absorbing boundary conditions are imposed for different layers in the analysis of molecular dynamics trajectories and the diffusion tensor of liquid is calculated for each layer. Here the way to apply this method in cylindrical geometry is present. The results for acetonitrile confined in the hydroxylated silica pore of diameter 44 Å are discussed.

The self-diffusion in inhomogeneous liquids can be described by the Smoluchowski equation,

$$\frac{\partial}{\partial t} p(\mathbf{r}, t | \mathbf{r}_0, t_0) = \nabla \cdot \mathbf{D} \cdot [\nabla + \beta \nabla W(\mathbf{r})] p(\mathbf{r}, t | \mathbf{r}_0, t_0) \quad (3.10)$$

where $p(\mathbf{r}, t | \mathbf{r}_0, t_0)$ is the conditional probability that a particle is at position \mathbf{r} at time t given it was at position \mathbf{r}_0 at time t_0 . \mathbf{D} is the diffusion tensor that is position-dependent. $W(\mathbf{r}) = -kT \ln(\rho(\mathbf{r}))$ is the potential of mean force resulting from the nonuniform density distribution of particles.

In the cylindrical pores, absorbing boundary conditions can be applied at radius r_a and r_b such that only particles in a thin concentric cylindrical shell are considered. \mathbf{D} and $W(\mathbf{r})$ are assumed to have no spatial dependence within this thin layer. This assumption is problematic for molecules near the surfaces. Thus the diffusion coefficients are not computed for the surface population in the present study. As we have shown, the diffusion along the

Z axis is anomalous in the surface population and conventional diffusion coefficients can not be defined. For the center population, with the above assumption, the Smoluchowski equation reduces to the diffusion equation that is much easier to solve. The diffusion equation can be separated into two equations, one for the parallel diffusion and one for the perpendicular diffusion.

$$\frac{\partial}{\partial t} p(z, t | z_0, t_0) = D_{\parallel} \frac{\partial^2}{\partial z^2} p(z, t | z_0, t_0) \quad (3.11)$$

$$\frac{\partial}{\partial t} p(r, \theta, t | r_0, \theta_0, t_0) = D_{\perp} \left(\frac{\partial^2}{\partial r^2} + \frac{1}{r} \frac{\partial}{\partial r} + \frac{1}{r^2} \frac{\partial^2}{\partial \theta^2} \right) p(r, \theta, t | r_0, \theta_0, t_0) \quad (3.12)$$

$$p(\mathbf{r}, t | \mathbf{r}_0, t_0) = p(r, \theta, t | r_0, \theta_0, t_0) p(z, t | z_0, t_0) \quad (3.13)$$

3.4.1 Parallel diffusion coefficient

As shown in Ref 1, the solution to the parallel diffusion equation is the well known Gaussian solution,

$$p(z, t | z_0, t_0) = \frac{1}{\sqrt{4\pi D_{\parallel} t}} \exp\left[-\frac{(z - z_0)^2}{4D_{\parallel} t}\right], \quad (3.14)$$

using the boundary condition

$$p(z \rightarrow \infty, t | z_0, t_0) = 0, \quad (3.15)$$

and the initial condition

$$p(z, t_0 | z_0, t_0) = \delta(z - z_0). \quad (3.16)$$

So the parallel mean square displacement of a particle that stays continuously in the shell from time t_0 to time $t_0 + t$ has linear dependence on time t at long time. The requirement that the particle has to stay continuously in the shell is due to the fact that the absorbing boundary conditions are applied in the radial direction at $r = r_a$ and $r = r_b$. The parallel mean square displacement of a particle that stays continuously inside the shell can be calculated from the molecular dynamics trajectory according to the following equation,

$$MSD_{1Z}(t) = \frac{1}{T} \sum_{t_0=1}^T \frac{1}{N(t_0, t_0+t)} \sum_{i \in \mathcal{S}(t_0, t_0+t)} (Z_i(t_0+t) - Z_i(t_0))^2 \quad (3.17)$$

where $\mathcal{S}(t_0, t_0+t)$ is the set of particles that stays continuously in the layer $\{r_a, r_b\}$ from timestep t_0 to t_0+t . $N(t_0, t_0+t)$ is the number of particles in the set $\mathcal{S}(t_0, t_0+t)$. Z_i is the Z coordinate of the i th particle. T is the total number of reference time points used in the time averaging. The parallel diffusion coefficient D_{\parallel} can be obtained from linear fit of $MSD_{1Z}(t)$ at large time,

$$MSD_{1Z}(t) \sim 2D_{\parallel}t \quad (3.18)$$

3.4.2 Perpendicular diffusion coefficient

The perpendicular diffusion equation needs to be solved with the absorbing boundary conditions,

$$p(r_a, \theta, t | r_0, \theta_0, 0) = p(r_b, \theta, t | r_0, \theta_0, 0) = 0, \quad (3.19)$$

and the initial condition,

$$p(r, \theta, 0 | r_0, \theta_0, 0) = \frac{1}{r_0} \delta(r - r_0) \delta(\theta - \theta_0) \quad (3.20)$$

($t_0 = 0$ has been adopted). The perpendicular diffusion equation can be solved after separation of variables.⁷³ The eigenfunctions of the spatial operator that satisfy the absorbing boundary conditions are

$$\Psi_{mn}(r, \theta) = \frac{1}{\sqrt{\pi G_{mn}}} [J_n(\omega_{mn}r) + B_{mn}N_n(\omega_{mn}r)] \cdot \begin{cases} \sqrt{\xi_n} \cos(n\theta) \\ \sqrt{2} \sin(n\theta) \end{cases} \quad (3.21)$$

$n = 0, 1, \dots; m = 1, 2, \dots$ ξ_n is 1 when $n = 0$ and 2 when $n \neq 0$.

$J_n(r)$ is the Bessel function of the first kind for integer order n . $N_n(r)$ is the Bessel function of the second kind for integer order n . ω_{mn} and B_{mn} can be obtained from the

absorbing boundary conditions,

$$\begin{cases} J_n(\omega_{mn}r_a) + B_{mn}N_n(\omega_{mn}r_a) = 0 \\ J_n(\omega_{mn}r_b) + B_{mn}N_n(\omega_{mn}r_b) = 0 \end{cases} \quad (3.22)$$

Thus ω_{mn} is the m th root of the equation

$$N_n(\omega_{mn})J_n(\omega_{mn}r_b) - N_n(\omega_{mn}r_b)J_n(\omega_{mn}r_a) = 0 \quad (3.23)$$

and

$$B_{mn} = -J_n(\omega_{mn}r_a)/(N_n(\omega_{mn}r_b)) \quad (3.24)$$

$$\begin{aligned} G_{mn} &= 2 \int_{r_a}^{r_b} r [J_n(\omega_{mn}r) + B_{mn}N_n(\omega_{mn}r)]^2 dr \\ &= r^2 [J_{n+1}(\omega_{mn}r) + B_{mn}N_{n+1}(\omega_{mn}r)]^2 \Big|_{r_a}^{r_b} \end{aligned} \quad (3.25)$$

Then with the initial condition, the solution of the perpendicular diffusion equation expressed in the form of an eigenfunction expansion is obtained

$$p(r, \theta, t | r_0, \theta_0, 0) = \sum_{n=0}^{\infty} \sum_{m=1}^{\infty} \Psi_{mn}^*(r, \theta) \Psi_{mn}(r_0, \theta_0) \exp(-D_{\perp} \omega_{mn}^2 t) \quad (3.26)$$

Using the orthogonality of the eigenfunctions, the autocorrelation function of one eigenfunction can be derived and it follows an exponential decay,

$$\begin{aligned} C_{\Psi}(t) &= \langle \Psi_{mn}(r(t), \theta(t)) \Psi_{mn}^*(r(0), \theta(0)) \rangle \\ &= \int_{r_a}^{r_b} r dr \int_0^{2\pi} d\theta \int_{r_a}^{r_b} r_0 dr_0 \int_0^{2\pi} d\theta_0 p(r, \theta, t | r_0, \theta_0, 0) p(r_0, \theta_0) \Psi_{mn}(r, \theta) \Psi_{mn}^*(r_0, \theta_0) \\ &= \frac{1}{\pi(r_a^2 - r_b^2)} \exp(-D_{\perp} \omega_{mn}^2 t) \end{aligned} \quad (3.27)$$

where $p(r_0, \theta_0) = 1/(\pi r_b^2 - \pi r_a^2)$ is the initial uniform distribution in the layer $\{r_a, r_b\}$.

This autocorrelation function can also be obtained from molecular dynamics trajectory,

$$C_{\Psi}(t) = \frac{1}{T} \sum_{t_0=1}^T \frac{1}{N(t_0)} \sum_{i \in \mathcal{S}(t_0, t_0+t)} \Psi_{mn}(r_i(t_0+t), \theta_i(t_0+t)) \Psi_{mn}^*(r_i(t_0), \theta_i(t_0)) \quad (3.28)$$

where $\mathcal{S}(t_0, t_0 + t)$ is the set of particles that stays continuously in the layer $\{r_a, r_b\}$ from timestep t_0 to $t_0 + t$. $N(t_0)$ is the number of particles in the layer at the initial reference timestep t_0 . r_i and θ_i are the coordinates of the i th particle in a cylindrical coordinate system. T is the total number of reference time points used in the time averaging.

The perpendicular diffusion coefficient D_{\perp} can be obtained from linear fit of $-\ln(C_{\Psi}(t))$ at large time,

$$-\ln(C_{\Psi}(t)) \sim D_{\perp} \omega_{mn}^2 t \quad (3.29)$$

3.4.3 Correction to the positions of the absorbing boundaries

As stated in Ref 1, there is a subtle difference between the absorbing boundaries used in the molecular dynamics analysis and the one used in the solution of the Smoluchowski equation. The boundary conditions used in the molecular dynamics analysis is actually the probability flux from outside regions to the layer under study is zero, $j_{out}(r = r_a \text{ or } r_b, t) = 0$. The probability of finding a particle at r_a or r_b is actually not zero as it will be in the Smoluchowski boundary conditions $p(r = r_a \text{ or } r_b, t) = 0$. So the width of the layer $\{r_a, r_b\}$ in the molecular dynamics analysis is smaller than that in the corresponding solution of the Smoluchowski equation. As in Ref 1, the correction width derived by Razi Naqvi *et al.*⁷⁴ is used here to correct the positions of the boundaries.

$$\lambda = (\pi m D_{\perp}^2 / 2 k_B T)^{1/2} \quad (3.30)$$

$$r_a^c = r_a - \lambda, r_b^c = r_b + \lambda \quad (3.31)$$

After correcting the positions of boundaries, the root ω_{mn}^c is obtained from solving Eq 3.23 with r_a^c and r_b^c . Then $D_{\perp}^c = D_{\perp} \omega_{mn}^2 / \omega_{mn}^c{}^2$. This corrective procedure is applied iteratively until self-consistency is achieved. Note r_a and r_b in Eq 3.31 should be kept to the values used in the first step, but not updated to the values in the last step.

Probably the necessity of correcting the boundaries is not well emphasized in some studies using the eigenfunction method.^{75,76} In one study using this method,⁷⁵ it was reported that D_{\perp} is about 10 percent smaller than D_{\parallel} for water in the center region of a clay slit pore of diameter 10 nm. However, the authors did not state whether the correction of boundaries has been adopted in the study. Since D_{\perp} will be underestimated without the correction, the readers may want to know the smaller D_{\perp} reported is not because of that the correction was not applied. From test calculations for bulk acetonitrile at 1 atm and 300K, it can be shown that without the correction the artifact on D_{\perp} is obvious. The eigenfunction method is applied in the analysis of acetonitrile in a cylindrical shell $\{3.8 \text{ \AA}, 8.2 \text{ \AA}\}$ for the bulk system. D_{\perp} is $0.42 \text{ \AA}^2/ps$ without the correction. Since the relation $MSD \sim 6Dt$ is valid for the bulk, the diffusion constant D can also be estimated from the slope of the MSD, which gives $D = 0.54 \text{ \AA}^2/ps$. The bulk acetonitrile is isotropic and $D_{\perp} < D$ must be erroneous. If we apply the correction of boundaries, the D_{\perp} given by the eigenfunction method is $0.53 \text{ \AA}^2/ps$, which is close to the value $D = 0.54 \text{ \AA}^2/ps$ obtained from the MSD method. So neglecting the correction of boundaries could give erroneous results, especially when the width of the layer is small.

3.4.4 Results

We have shown that the method described above can not compute diffusion coefficients in a surface population. So this method is employed to further analyze only the center population of acetonitrile in the hydroxylated silica pore of diameter 44 Å. We have shown that the method could not be used to compute diffusion coefficients in surface population. The center population is divided into four non-overlapping layers of width about 4 Å. The exact boundaries are $\{0 \text{ \AA}, 3.8 \text{ \AA}\}$, $\{3.8 \text{ \AA}, 8.2 \text{ \AA}\}$, $\{8.2 \text{ \AA}, 12.5 \text{ \AA}\}$, $\{12.5 \text{ \AA}, 17.0 \text{ \AA}\}$. Although it is more natural to let each layer contain only one sub-layer as shown in Figure 3.5, the errors are very large in such setting since the width of the layer (about 2 Å) is even smaller

than the scale of one acetonitrile molecule. So the exact boundaries of each layer are set such that one layer contains two antiparallel sub-layers as shown in Figure 3.5.

The mean square displacements along the axis direction for acetonitrile in different layers are computed according to Eq 3.17. The results are shown in the top panel of Figure 3.14. From the family of eigenfunctions defined in Eq 3.21, the one of lowest order ($m=1$ and $n=0$) is used to compute the eigenfunction autocorrelation functions according to Eq 3.28. Numerical errors will be greater if the eigenfunctions of higher order are used, since their autocorrelation decay faster. The eigenfunction used for the $\{0 \text{ \AA}, 3.8 \text{ \AA}\}$ layer is $J_0(\omega r)$ since there is only one absorbing boundary for this layer. The natural logarithms of the eigenfunction autocorrelation functions are shown in the bottom panel of Figure 3.14. Both the axial mean square displacements and the logarithms of the eigenfunction autocorrelation functions are mostly linear in time after a short period. The linear relationships deteriorate a little in the $\{12.5 \text{ \AA}, 17.0 \text{ \AA}\}$ layer that is closest to the surface population. Linear regression is used to extract the parallel diffusion coefficients D_{\parallel} and the perpendicular diffusion coefficients D_{\perp} from the data in the time window 2-6 ps. The results are given in Table 3.1. The errors are estimated as the standard deviations of the results computed from five different trajectories of simulation time 1 ns.

The diffusion tensors in different layers increase as a function of distance from the surface. The parallel and perpendicular diffusion coefficients in the $\{12.5 \text{ \AA}, 17.0 \text{ \AA}\}$ layer closest to the surface population are 31% and 39% smaller than the values in the $\{0 \text{ \AA}, 3.8 \text{ \AA}\}$ layer at the center of the pore. The diffusion tensors in the $\{3.8 \text{ \AA}, 8.2 \text{ \AA}\}$ layer and the $\{0 \text{ \AA}, 3.8 \text{ \AA}\}$ layer are about the same. The surface perturbation on the translational mobility of acetonitrile diminishes at a distance 14 \text{ \AA} from the surface. The diffusion coefficients at the center of the pore are about 18% greater than the $0.53 \text{ \AA}^2/\text{ps}$ value computed for the bulk system, probably due to the somewhat lower density in the center of the pore than in bulk.

The perpendicular diffusion coefficient D_{\perp} is 12% smaller than the parallel diffusion coefficient D_{\parallel} in the $\{12.5 \text{ \AA}, 17.0 \text{ \AA}\}$ layer closest to the surface population. In the other three layers, the diffusion tensor is nearly isotropic with D_{\perp} slightly smaller than D_{\parallel} . The diffusion tensor is expected to be isotropic for liquids far from the surfaces. Milischuk and Ladanyi³⁰ also found that D_{\perp} is slightly smaller than D_{\parallel} for water confined in a hydroxylated silica pore of diameter 40 Å, although the initial position method was used in their study. Wick and Dang⁷⁷ reported that the diffusion tensor is isotropic in the liquid phase 2 nm far away from the vapor-liquid interface of 2.2M sodium chloride aqueous solution, using a modified version of Liu *et al.*'s dual simulation method.¹ However, Botan *et al.*⁷⁵ found that D_{\perp} is 10% smaller than D_{\parallel} for water 5 nm away from the surface of a slit clay pore, using the eigenfunction method but whether the boundary correction was applied is unknown. The authors argued that the reason for the anisotropic diffusion tensor is related to the size-dependence of the diffusion coefficient⁷⁸ and the simulation box used is twice as large in the perpendicular direction than in the parallel direction. Predota *et al.*⁷⁹ found that D_{\parallel} is 10% higher than D_{\perp} for water 4 nm away from the Rutile surface, using a modified version of the plain MSD method that is not detailed well in the paper. The different results obtained using different methods and different systems urge in-depth studies in the future, to understand whether the diffusion is isotropic or anisotropic for liquids several nanometers away from the interfaces.

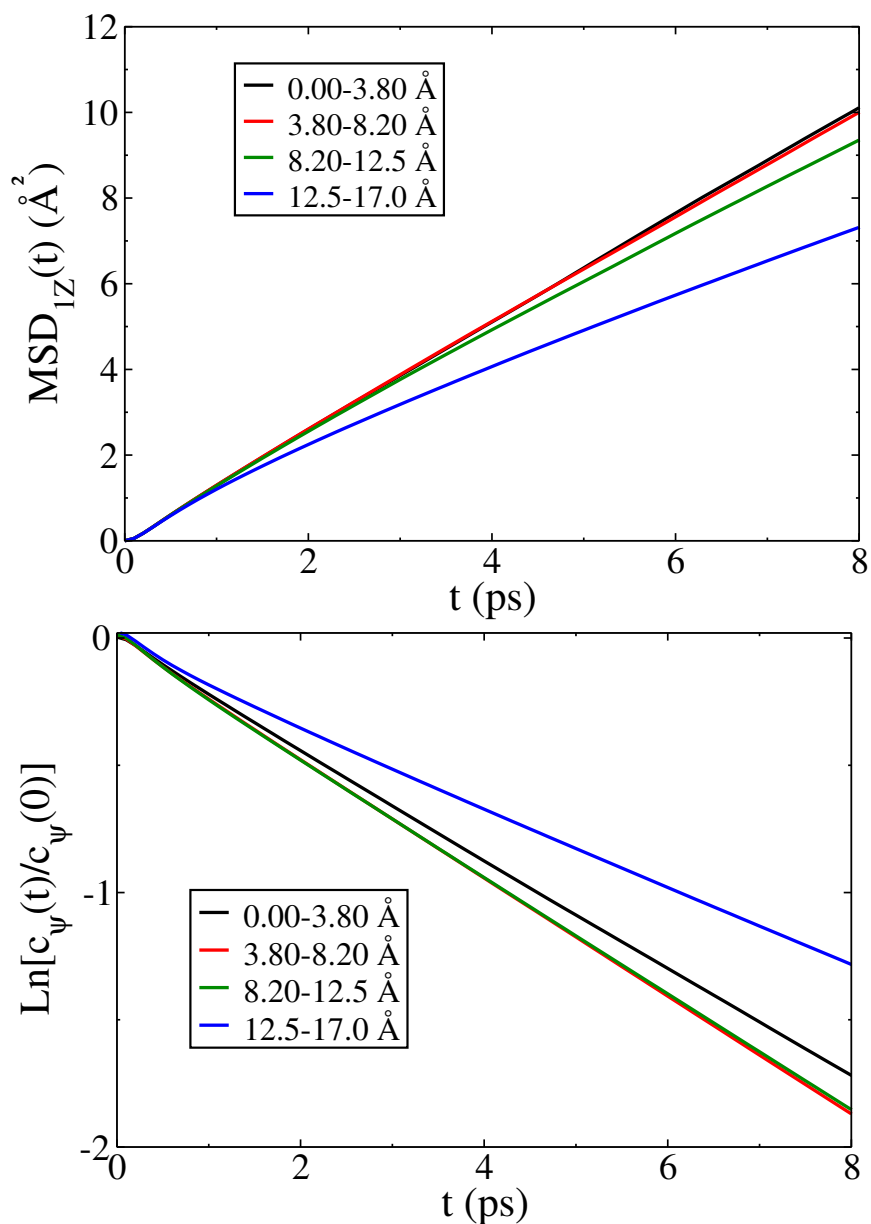


Figure 3.14: The axial mean square displacements (A) and the natural logarithms of the radial eigenfunction autocorrelation functions (B) are shown for acetonitrile in four different layers in the hydroxylated silica pore of diameter 44 Å. The black, red, blue and green colors are for the $\{0 \text{ Å}, 3.8 \text{ Å}\}$, $\{3.8 \text{ Å}, 8.2 \text{ Å}\}$, $\{8.2 \text{ Å}, 12.5 \text{ Å}\}$, $\{12.5 \text{ Å}, 17.0 \text{ Å}\}$ layers, respectively.

Layer	D_{\parallel} ($\text{\AA}^2/\text{ps}$)	D_{\perp} ($\text{\AA}^2/\text{ps}$)
{0 \AA , 3.8 \AA }	0.63 ± 0.04	0.62 ± 0.02
{3.8 \AA , 8.2 \AA }	0.62 ± 0.02	0.61 ± 0.01
{8.2 \AA , 12.5 \AA }	0.569 ± 0.006	0.551 ± 0.006
{12.5 \AA , 17.0 \AA }	0.432 ± 0.006	0.378 ± 0.003

Table 3.1: Diffusion coefficients for acetonitrile in four different layers in the hydroxylated silica pore of diameter 44 \AA

3.5 Conclusions

To better understand the structure and dynamics of liquid acetonitrile confined in a nanoscale silica pore, extensive molecular dynamics simulations are carried out. We develop a force field, in which the interfacial interactions are parametrized from *ab initio* molecular dynamics simulations. In agreement with previous simulation studies,^{26,28,29} our structural analysis demonstrates that the acetonitrile molecules within a distance of 4.5 \AA from the hydroxylated silica surface form a bilayer structure with two antiparallel oriented sublayers, where acetonitriles in the closest sublayer are ordered with the nitrogen end pointing toward the surface. This antiparallel layering effect can propagate into the center regions of the pores of radius 12 \AA and 22 \AA , and it was found that such an effect could propagate for 20 \AA for acetonitriles near a flat hydroxylated crystal silica surface.²⁹ Through charge density profile analysis, we show that such a long range layering effect is mainly caused by the charge distribution on the silica surface and is not sensitive to the presence of specific hydrogen bonding interactions, in agreement with the results of Ref. 26.

To better differentiate the dynamics of two inherently different populations, we adopt a different approach that takes into account the survival probability of the populations when calculating the singlet orientational time correlation functions and the mean square dis-

placements. Compared to the initial position technique,³⁰ the present method better differentiates the different populations and offers a sharper picture of the two population dynamics. For the three pore functionalizations studied, the orientational relaxation of the surface populations is constrained by the surface and decay to plateaus whose values are higher than found for the center populations. Only for the surface population in the pore that includes hydrogen bonding interactions is the relaxation of the orientational fluctuations qualitatively different from that of the bulk acetonitrile population. In this way, specific hydrogen bonding interactions greatly impact the dynamics at the interface. Based on survival probability approach and Loughnane, *et al.*'s work,²⁰ we find that the total singlet reorientational dynamics could be well reproduced with a two-population exchange model. Furthermore we find that singlet reorientational dynamics in specific layers has very little dependence on the diameters of the pores. Such a model could be general for strongly wetting liquids in nanopores.²⁰

Chapter 4

First Passage Time Distribution in Stochastic Processes with Application to Forced Rupture Experiments

4.1 Single Molecule Forced Rupture Experiments

Single molecule force-clamp technique can be used to study the mechanical properties of biomarcomolecules, the unfolding kinetics of proteins,³⁸ and the catalytic kinetics of the disulfide bond reactions.⁸⁰ Here we focus on the kinetics of protein unfolding under controlled force in single molecule forced rupture experiments. A schematic representation of a single molecule forced rupture experiment using atomic force microscopy is shown in Figure 4.1. One end of the protein molecule is bonded to a surface. The other end of the protein is attached to the tip of an elastic cantilever through a molecular linker. The loading force on the cantilever can be measured from the position of a laser beam reflected by the cantilever. The controlled force is usually applied in two different ways, the constant force condition⁸⁰ and the constant velocity condition.³⁸ Under the constant force condition, the

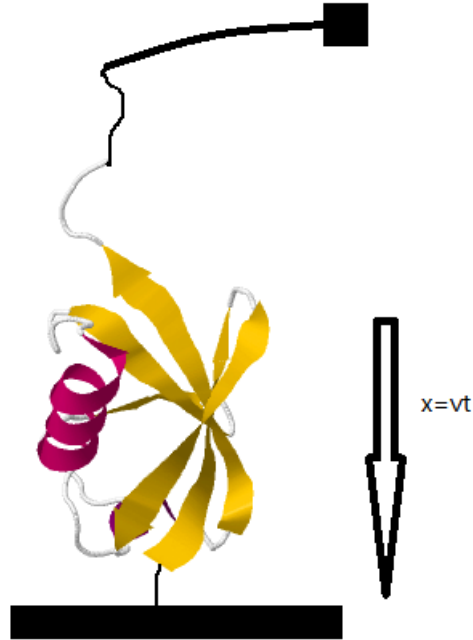


Figure 4.1: Schematic representation of a single molecule forced rupture experiment

loading force is maintained at a constant value by a force feedback system. The constant force condition is not studied in this work. Under the constant velocity condition, the surface that is bonded to one end of the protein is moved away from the cantilever at a constant velocity, and the loading force on the cantilever grows in time. After certain time, the protein molecule can not hold itself in the compact native structure, the protein molecule unfolds to a loose structure and the loading force drops abruptly. So the force at rupture can be measured as the value before the abrupt drop. The probability distribution of the force at rupture is obtained after recording the forced unfolding events in a number of samples. The rupture force distribution provides information about the kinetics of mechanical unfolding of the protein.

4.2 Kramers' Theory

The single molecule forced rupture experiments can be considered as the barrier crossing problem of Brownian particles in a potential. For the case where the potential is time independent, the problem was treated by Kramers in 1940.² The resulting Kramers' theory is fundamental in understanding the chemical kinetics in condensed phase.

Consider a Brownian particle in a one dimensional time-independent potential $V(x)$, its equation of motion is assumed to be the Langevin equation:

$$m \frac{d^2x}{dt^2} = -\frac{dV(x)}{dx} - \zeta \frac{dx}{dt} + \delta F(t) \quad (4.1)$$

$-\frac{dV(x)}{dx}$ is the force generated by the potential $V(x)$. $-\zeta \frac{dx}{dt}$ is the frictional force. $\delta F(t)$ is the fluctuating force that is a Gaussian white noise stochastic process.

$$\langle \delta F(t) \rangle = 0 \quad (4.2)$$

$$\langle \delta F(t) \delta F(t') \rangle = 2\zeta k_B T \delta(t - t') \quad (4.3)$$

The second moment $2\zeta k_B T$ in Eq 4.3 is a result of the fluctuation-dissipation theorem. The Einstein's relation $\zeta = k_B T / D$ relates the friction coefficient ζ to the diffusion coefficient D . In the high friction limit, neglecting the $m \frac{d^2x}{dt^2}$ term on the left hand side, the Langevin equation (Eq 4.1) can be rewritten as

$$\frac{dx}{dt} = -D \frac{\beta dV(x)}{dx} + \sqrt{2D} \xi(t) \quad (4.4)$$

where $\beta = 1/k_B T$ and $\xi(t)$ is a Gaussian white noise process with zero mean and unit variance. The probability density function of a stochastic process described by a Langevin equation satisfies the Fokker-Planck equation. For the Langevin equation Eq 4.4, the corresponding Fokker-Planck equation is also called the Smoluchowski equation

$$\frac{\partial f(x,t)}{\partial t} = D \frac{\partial}{\partial x} \left[\frac{\partial \beta V(x)}{\partial x} + \frac{\partial}{\partial x} \right] f(x,t) \quad (4.5)$$

For the barrier crossing problem, the Brownian particle starts from a position x_0 in the potential well at a initial time $t_0 = 0$. After a time t^* , the Brownian particle has passed the energy barrier and arrives at a position b ($b > x_0$) on the other side of the barrier for the first time. Considering there is a sink at position b , then the first passage time t^* is also the time when the particle is absorbed by the sink. The first passage time can model the time it takes for the chemical reaction to reach the product state starting from the reactant state, or the time it takes to rupture a protein in the single molecule forced rupture experiments. For the first passage time calculation, we can apply the following initial condition and absorbing boundary condition to the Smoluchowski equation (Eq 4.5)

$$\begin{cases} f(x,0) = \delta(x-x_0) \\ f(b,t) = 0 \end{cases} \quad \text{for } 0 \leq t < +\infty \quad (4.6)$$

The survival probability is defined as

$$S(t) = \int_{-\infty}^b dx f(x,t) = P(x(t) \leq b | x(0) = x_0) \quad (4.7)$$

which is a conditional probability of finding the particle having not passed over the point b at time t given that the particle is initially located at x_0 . The first passage time distribution,

$$h(t) = -\frac{dS(t)}{dt} \quad (4.8)$$

is such that $h(t)dt$ is the probability that the particle passes through the point b for the first time in the time interval $(t, t + dt)$. The mean first passage time is,

$$\tau(x_0) = \int_0^{\infty} dt t h(t) = \int_0^{\infty} dt S(t). \quad (4.9)$$

It can be shown that the mean first passage time satisfies the adjoint equation,⁸¹

$$\mathcal{L}_{FP}^+ \tau(x) = -1, \quad \tau(b) = 0 \quad (4.10)$$

in which \mathcal{L}_{FP}^+ is the adjoint of the Fokker-Planck operator. For the Smoluchowski equation Eq 4.5, the Fokker-Planck operator can be rewritten as

$$\mathcal{L}_{FP} = D \frac{\partial}{\partial x} e^{-\beta V(x)} \frac{\partial}{\partial x} e^{\beta V(x)}. \quad (4.11)$$

So the adjoint equation is

$$D e^{\beta V(x)} \frac{\partial}{\partial x} e^{-\beta V(x)} \frac{\partial}{\partial x} \tau(x) = -1, \quad \tau(b) = 0. \quad (4.12)$$

Solving the adjoint equation by quadrature, the mean first passage time is

$$\tau(x_0) = \frac{1}{D} \int_{x_0}^b dx e^{\beta V(x)} \int_{-\infty}^x dy e^{-\beta V(y)}. \quad (4.13)$$

where we assumed the diffusion constant D does not vary with position. If the energy barrier is high compared to $k_B T$, the integrals can be approximated by the Laplace method. Expanding $V(x)$ around the potential maximum and the potential minimum, the mean first passage time is approximately

$$\tau(x_0) \approx \frac{2\pi k_B T}{D \sqrt{|V^{(2)}(x_{min})| |V^{(2)}(x_{max})|}} e^{\beta \Delta U}, \quad (4.14)$$

where ΔU is the height of the energy barrier and $V^{(2)}(x)$ is the second derivative of $V(x)$. Then we obtain the Kramers rate constant in the high friction limit

$$k_0 = \frac{1}{\tau} = \frac{D\beta \sqrt{|V^{(2)}(x_{min})| |V^{(2)}(x_{max})|}}{2\pi} e^{-\beta \Delta U} \quad (4.15)$$

After integrating the first-order kinetics equation $dS(t)/dt = -k_0 S(t)$, the survival probability is

$$S(t) = e^{-k_0 t} \quad (4.16)$$

4.3 Adiabatic Approximation for a Time-dependent Potential in Forced Rupture Experiments

To model the Langevin dynamics of the pulling coordinate of a protein molecule under a constant velocity pulling force, Hummer and Szabo³ used a time-dependent harmonic potential with a sink as the potential of mean force,

$$\beta V(x,t) = \begin{cases} \frac{1}{2}k_m x^2 + \frac{1}{2}k_s(x-vt)^2 & x \leq b \\ -\infty & x > b \end{cases}, \quad (4.17)$$

where x is the fluctuating distance between the two pulling points, $\frac{1}{2}k_m x^2$ is assumed to be the intrinsic potential of mean force of the molecular system along the pulling coordinate, v is the pulling speed, k_s is the effective spring constant of the pulling apparatus, and the minus partial derivative of $\frac{1}{2}k_s(x-vt)^2$ with respect to x is the force exerted on the molecule by the pulling apparatus. Note the potential has been scaled by $k_B T$, so $k_m \leftrightarrow k_m \beta$ and $k_s \leftrightarrow k_s \beta$ should be used when interpreting the results obtained later.

Hummer and Szabo³ used an adiabatic approximation to calculate the time-dependent Kramers rate constant $K(t)$, using the instantaneous potential at time t . This approximation is good only if the time-dependent potential changes slowly compared to the diffusional exploration of the instantaneous potential surface. Then the time-dependent rate constant $K(t)$ is used to calculate the survival probability

$$S(t) = \exp \left\{ - \int_0^t K(\tau) d\tau \right\}, \quad (4.18)$$

assuming first-order kinetics $dS(t)/dt = -K(t)S(t)$. The adiabatic approximation extends the Kramers result for the rate constant in Eq 4.13 to a time-dependent potential as

$$K(t)^{-1} = \frac{1}{D} \int_{x_0}^b dx e^{\beta V(x,t)} \int_{-\infty}^x dy e^{-\beta V(y,t)}. \quad (4.19)$$

For a simple time-dependent harmonic potential defined in Eq. 4.17, Eq. 4.19 can be evaluated approximately and an analytic expression can be derived. To derive it, let us first

consider the time-independent case in which $k_s = 0$, then the intrinsic rate constant is

$$k_0^{-1}(k_m, b) = \frac{1}{D} \int_{x_0}^b dx e^{(1/2)k_m x^2} \int_{-\infty}^x dy e^{-(1/2)k_m y^2} \quad (4.20)$$

The inner integral is mostly contributed to by the integrand around the potential minimum $y = 0$. So we can raise the upper limit to infinity and obtain a Gaussian integral,

$$\int_{-\infty}^x dy e^{-(1/2)k_m y^2} \approx \int_{-\infty}^{\infty} dy e^{-(1/2)k_m y^2} = \sqrt{\frac{2\pi}{k_m}} \quad (4.21)$$

The outer integral is mostly contributed to by the integrand around the position $x = b$. We can replace the lower limit with minus infinity and expand the potential around b ,

$$\int_{x_0}^b dx e^{(1/2)k_m x^2} \approx \int_{-\infty}^b dx e^{(1/2)k_m b^2 + k_m b(x-b)} = \frac{1}{k_m b} e^{(1/2)k_m b^2} \quad (4.22)$$

Then the intrinsic rate constant is

$$k_0(k_m, b) \approx \frac{D}{\sqrt{2\pi}} k_m^{3/2} b e^{-\frac{1}{2}k_m b^2}. \quad (4.23)$$

The time-dependent potential in Eq 4.17 can be reorganized as

$$\begin{aligned} \beta V_0(x, t) &= \frac{1}{2} k_m x^2 + \frac{1}{2} k_s (x - vt)^2 \\ &= \frac{1}{2} k \left(x - \frac{k_s vt}{k} \right)^2 + \frac{1}{2} \frac{k_m k_s v^2 t^2}{k} \\ &= \frac{1}{2} k (x - s)^2 + \frac{1}{2} \frac{k k_m s^2}{k_s}, \end{aligned} \quad (4.24)$$

where $k = k_m + k_s$, and $s = k_s vt / k$ is a parameter independent of x . Based on the result of Eq 4.23, the time-dependent rate constant is

$$K(t) = k_0(k, b - s) \approx \frac{D}{\sqrt{2\pi}} k^{3/2} \left(b - \frac{k_s vt}{k} \right) e^{-\frac{1}{2}k(b - k_s vt/k)^2} \quad (4.25)$$

Following first-order kinetics, Eq 4.18 reads

$$S(t) \approx \exp \left\{ -\frac{Dk^{3/2} e^{-\frac{1}{2}kb^2}}{\sqrt{2\pi} k_s v} \left[\exp \left\{ k_s v t - \frac{1}{2} \frac{(k_s vt)^2}{k} \right\} - 1 \right] \right\}. \quad (4.26)$$

which is the same as Eq 16 in Ref 3 after using the expression Eq 4.23 for k_0 .

Experimentalists usually report the distribution and average of the force at rupture for different pulling speeds. The force at rupture is

$$F = -k_s(b - vt^*) \quad (4.27)$$

in which t^* is the first passage time. The mean rupture force and the rupture force distribution can be determined from the integration and the differentiation of the survival probability,

$$\bar{F} = -k_s(b - v\bar{t}^*) = -k_s(b - v \int_0^\infty S(t)dt) \quad (4.28)$$

$$p(F) = \frac{1}{k_s v} h(t)|_{t=(F+k_s b)/(k_s v)} \quad (4.29)$$

where $h(t)$ is the first passage time distribution.

The above analytic expressions obtained by Hummer and Szabo has been widely used to extract kinetics information from single molecule forced rupture experiments. The above procedure for handling this simple potential can be generalized to more complicated potentials as shown by Dudko *et. al.*^{32,33} and Freund.³⁴ Freund has also shown that the first-order rate equation can be naturally derived from a thermodynamic approach. It has been noted that the underlying adiabatic approximation breaks down at extreme pulling speeds.³² It might be interesting to know whether their analytic formulas (eq. 16 in ref. 3, eq. (4) in ref. 32 and eq. (1) in ref. 33 and eq. (10) and (14) in ref. 34) are valid or not at conditions of slow intrinsic reaction rates (small k_0 or small D) or relatively larger pulling spring constant k_s .

4.4 Integral Equations of First Passage Time Distribution

The analytical formulas derived by Hummer and Szabo using the adiabatic approximation are inaccurate at large pulling speed. So we want to derive an exact equation for the first

passage time distribution. It is usually difficult to solve the combined initial value and boundary value problem described by Eq 4.5 and Eq 4.6 while the solution to the Smoluchowski equation itself without any absorbing boundary condition, i.e. the usual conditional probability (Green's function) in the absence of reaction, might be easily obtained for special cases of $V(x, t)$. Letting $f^0(x, t|x_\tau, \tau)$ denote that conditional probability subject to a general initial condition $f(x, \tau) = \delta(x - x_\tau)$, we derive an integral equation relating the first passage time distribution $h(t)$ to $f^0(x, t|x_\tau, \tau)$.

Clearly, the usual conditional probability in the absence of reaction at time t for any point $x < b$ has two contributions: one from the real survival events and the other from events where the particle passed over the point b at an earlier time τ ($\tau < t$) but later comes back to the point x . This argument yields:

$$f^0(x, t|x_0, 0) = f(x, t) + \int_0^t d\tau h(\tau) f^0(x, t|b, \tau) \quad \text{for } x \leq b^- \quad (4.30)$$

Similarly, in the event that the particle is at any point $x > b$ at time t , the particle must have passed over the point b at an earlier time τ . We thus have the relation for $x > b$:

$$f^0(x, t|x_0, 0) = \int_0^t d\tau h(\tau) f^0(x, t|b, \tau) \quad \text{for } x \geq b^+ \quad (4.31)$$

The arguments used here to derive Eq 4.30 and 4.31 are conceptually similar to arguments used for discrete random walks with absorbing walls.^{31,41,42} Similar relations in Laplace space connecting the two Green's functions (with and without the absorbing boundaries) have been previously derived as well.^{82,83} When the usual conditional probability $f^0(x, t|x_0, 0)$ is continuous at the point b , Eq 4.30 and 4.31 are consistent with the absorbing boundary condition in Eq 4.6. Integrating both sides of Eq 4.30, we obtain the self-consistent relation between survival probability and the first passage time distribution:

$$\int_{-\infty}^b dx f(x, t) \equiv S(t) = \int_{-\infty}^b dx f^0(x, t|x_0, 0) - \int_0^t d\tau h(\tau) \int_{-\infty}^b dx f^0(x, t|b, \tau). \quad (4.32)$$

4.4.1 Some analytical solutions

Exact Eqs 4.30, 4.31 and 4.32 are soluble for three cases of time-independent potentials shown in Fig. 4.2 (A). In case of the free particle diffusion $V_0(x) = 0$, the usual conditional probability and the first passage time distribution are:

$$f^0(x, t | x_\tau, \tau) = \frac{1}{\sqrt{4\pi D(t-\tau)}} \exp \left\{ -\frac{(x-x_\tau)^2}{4D(t-\tau)} \right\}, \quad (4.33)$$

and

$$h(t) = \frac{(b-x_0)}{\sqrt{4\pi D t^3}} \exp \left\{ -\frac{(b-x_0)^2}{4Dt} \right\}, \quad (4.34)$$

respectively. In the long time limit $t \gg (b-x_0)^2/D$, the first passage time distribution asymptotically decays as $t^{-3/2}$. In case of the linear potential $V_0(x) = -Fx$, we have:

$$f^0(x, t | x_\tau, \tau) = \frac{1}{\sqrt{4\pi D(t-\tau)}} \exp \left\{ -\frac{(x-x_\tau - FD(t-\tau))^2}{4D(t-\tau)} \right\}, \quad (4.35)$$

and

$$h(t) = \frac{(b-x_0)}{\sqrt{4\pi D t^3}} \exp \left\{ -\frac{(b-x_0 - FDt)^2}{4Dt} \right\}. \quad (4.36)$$

In the long time limit $t \gg (b-x_0)/(FD)$, $h(t)$ decays as $t^{-3/2} e^{-F^2Dt/4}$. In case of the harmonic potential $V_0(x) = \frac{1}{2}kx^2$ with $b = 0$, we have:

$$f^0(x, t | x_\tau, \tau) = \frac{1}{\sqrt{2\pi\sigma_{t-\tau}}} \exp \left\{ -\frac{(x-x_\tau e^{-Dk(t-\tau)})^2}{2\sigma_{t-\tau}} \right\}, \quad (4.37)$$

and

$$h(t) = \frac{2De^{-Dkt}|x_0|}{\sqrt{2\pi\sigma_t^3}} \exp \left\{ -\frac{(x_0 e^{-Dkt})^2}{2\sigma_t} \right\}. \quad (4.38)$$

where the variance $\sigma_t = (1 - e^{-2Dkt})/k$. In the long time limit $t \gg 1/(Dk)$, the asymptotic behavior is $h(t) \sim e^{-Dkt}$. For convenience, we have assumed $\beta = 1$ for all the three cases considered here. For cases of particle diffusion in zero or linear potential, the results for first passage time distribution, Eqs 4.34 and 4.36 can be alternatively obtained either by a Green's function approach or by an intuitive image method.^{31,41} For the harmonic potential

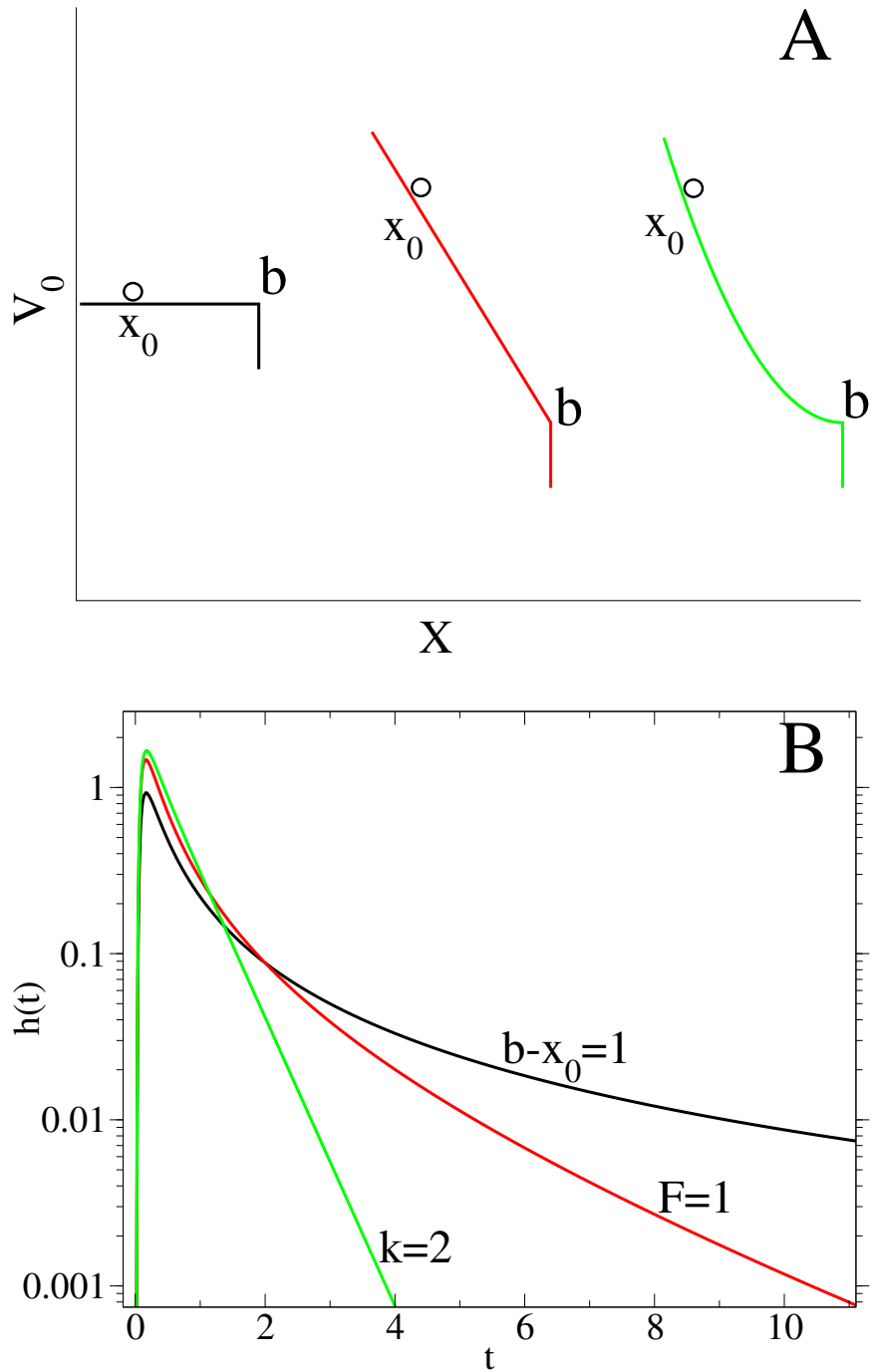


Figure 4.2: Several different potentials where we can solve the boundary value problem analytically. The particle starts from a position x_0 and disappears when passing over the point b . From left to right, $V_0(x) = 0$, $V_0(x) = -Fx$, and $V_0(x) = \frac{1}{2}kx^2$.

with the absorbing boundary at the bottom, Eq 4.38 has also been previously obtained through the image method by Szabo *et.al.*⁸⁴ In the Appendix A, we show how one can easily solve the first passage problem through the integral Eqs 4.31 and 4.32 for the three linear processes. A plot of the first passage time distributions for parameters $D = 1$, $b - x_0 = 1$, $F = 1$ and $k = 2$ are shown in Fig. 4.2 (B). The long tail behavior $t^{-3/2}$ in the case of free diffusion rapidly vanishes as the diffusion is biased while the peak of the $h(t)$ is much more slowly varying. As the first passage model of the biased diffusive process in the linear potential was used to understand the distribution of times between voltage spikes in neuron dynamics,^{85,86} the analytical formula Eq 4.38 might be useful to study the cases of integrate-and-fire neurons where the excitatory or inhibitory inputs linearly depends on the distance between the accumulated potential and the threshold.

4.4.2 Numerical solutions

For a complicated form of the potential $V(x, t)$, there is no analytical expression for either the first passage time distribution or the usual conditional probability in the absence of reaction. However, for the simple model potential $\beta V(x, t) = \frac{1}{2}k_m x^2 + \frac{1}{2}k_s(x - vt)^2$,^{3,32,33} the usual conditional probability of this linear process has a Gaussian form⁸⁷ (See details in Appendix B):

$$f^0(x, t | x_\tau, \tau) = \frac{1}{\sqrt{2\pi\sigma_{t-\tau}}} \exp\left\{-\frac{(x - \bar{x}_{\tau,t})^2}{2\sigma_{t-\tau}}\right\}, \quad (4.39)$$

with the mean and variance:

$$\bar{x}_{\tau,t} = x_\tau e^{-Dk(t-\tau)} + \frac{k_s v}{Dk^2} \left((1 - Dk\tau)e^{-Dk(t-\tau)} + Dkt - 1 \right), \quad (4.40)$$

and

$$\sigma_{t-\tau} = (1 - e^{-2Dk(t-\tau)})/k. \quad (4.41)$$

We are not able to solve the corresponding Smoluchowski equation (Eq 4.5) subject to the absorbing boundary condition (Eq 4.6) analytically to obtain the survival probability

and the first passage time distribution. Instead, we evaluate the numerical solution of the integral equation Eq 4.32 with the usual conditional probability of Eq 4.39. Since the upper limit of the survival probability is:

$$S(t) \leq \int_{-\infty}^b dx f^0(x, t | x_0, 0) = \frac{1}{2} \operatorname{erfc} \left(-\frac{(b - \bar{x}_{0,t})}{\sqrt{2\sigma_t}} \right), \quad (4.42)$$

Eq 4.32 might be solved iteratively by taking the upper limit as an ansatz. For general diffusive models having frequencies in the well (x_0) and the transition (b) regions, we might be able to use the analytical expression of the usual conditional probability corresponding to the harmonic potential for $f^0(x, t | x_0, 0)$ as in Eq 4.39 and use that corresponding to the inverted parabolic potential for $f^0(x, t | b, \tau)$ to solve Eq 4.32 numerically.

We choose parameters $k_m = 900\text{pN/nm}$, $k_s = 10\text{pN/nm}$, $b = 0.42\text{nm}$ describing the unfolding of the I27 protein monomer.^{3,38} The diffusion constant is chosen as either $D = 0.044\text{nm}^2/\text{ms}$ or $D = 0.0044\text{nm}^2/\text{ms}$ corresponding to the intrinsic reaction rate $k_0 = 10^{-4}\text{s}^{-1}$ or $k_0 = 10^{-5}\text{s}^{-1}$ respectively. Both intrinsic reaction rates are typical of biological systems. Fig. 4.3 shows the results for the survival probability from direct simulations of the stochastic process Eq 4.4 (black lines with circles), numerical solutions of the integral Eq 4.32 (red), the approximate analytical form of Eq 4.26 derived by Hummer and Szabo³ (green) and the upper limit Eq 4.42 (blue lines with crosses). All green lines are terminated at t such that $\bar{x}_{0,t} = b$ when the upper limit of the exact survival probability is equal to $1/2$.

The overlap between the black and red lines confirms the exact relation between the usual conditional probability and the first passage time distribution at all pulling speeds and intrinsic reaction rates. The statistics and efficiency are much better when the numerical results are generated from the integral equation rather than from the stochastic simulation. As expected, the adiabatic approximation underlying Eq 4.26 is invalid at larger pulling speeds. Fig. 4.3 (A) and (C) shows that the previous theory (Eq (16) in Ref 3) starts to break down at relatively slower pulling speeds when the intrinsic rate of the system is rela-

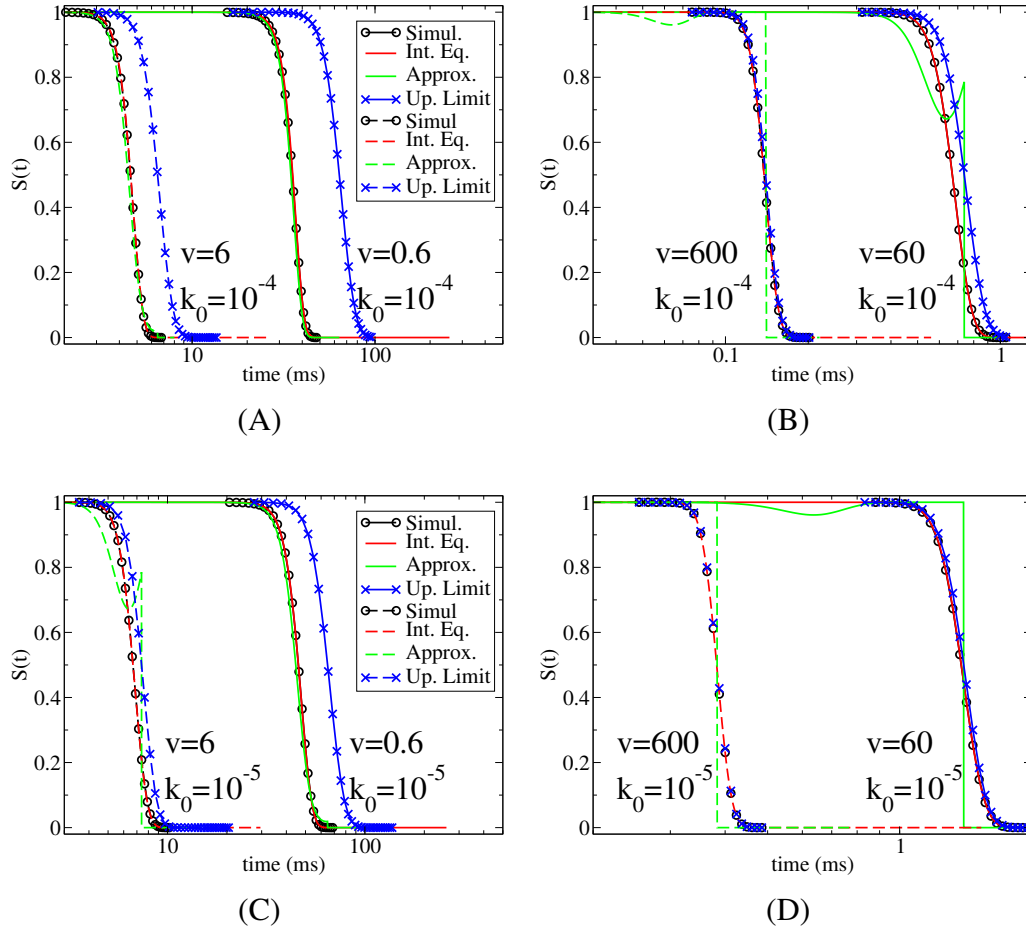


Figure 4.3: Survival probabilities at four different pulling speeds and two different diffusion constants calculated from several numerical and analytical methods. The k_0 rates are 10^{-4} s^{-1} (A and B) and 10^{-5} s^{-1} (C and D) respectively. Four pulling speeds $v = 0.6, 6.0, 60.0$ and 600.0 nm/ms are studied. Black, red, green and blue lines are numerical results from stochastic simulation, numerical results from the integral equation, approximated analytical results and the Gaussian upper limit results respectively. Black and red lines overlap in all graphs. Black, red and blue dash lines in graph (B) and (D) overlap. The pulling spring constant is $k_s = 10 \text{ pN/nm}$ and $x_0 = 0$. We have put circles on the black lines (simulation results) and crosses on the blue lines (upper limit results) for a better view.

tively smaller ($k_0 = 10^{-5} \text{s}^{-1}$). In the limit of large pulling speeds, the survival probability approaches its upper limit indicating that the recrossing events make small contributions to the usual conditional probability. The analytical upper limit formula could be used to obtain estimates of thermodynamic and kinetic parameters when experimental data at large pulling speeds are available.

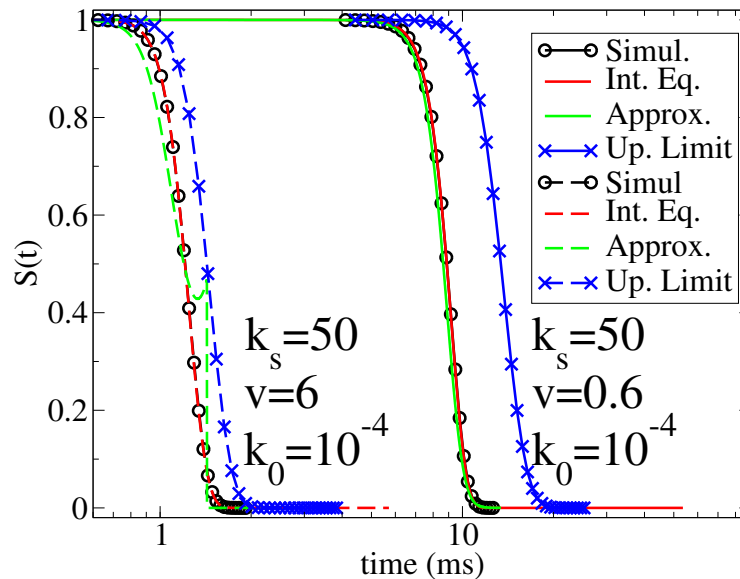


Figure 4.4: Survival probability at two different pulling speeds, similar to Fig. 4.3 (A) but for the pulling spring constant $k_s = 50$ pN/nm. Black and red lines overlap. All the labels are the same as in Fig. 4.3.

In experimental systems of forced protein unfolding where multimodules connected by molecular linkers are used instead of a single module, the effective pulling spring constant k_s is relevant not only to the cantilever of the apparatus but also to the properties of the molecular linker and the module itself. In a recent experiment of unfolding I27 domain by Harris and Kiang,⁸⁸ the spring constant of the cantilever is 50pN/nm. As suggested by Hummer and Szabo,³ a rough estimate from the slope of the force-extension curves before rupture (Fig 1b in Ref 88) yields the effective pulling spring constants $k_s = 10 \sim 20$ pN/nm. Fig. 4.4 shows our calculations of the survival probabilities at

$k_s = 50\text{pN/nm}$ and $k_0 = 10^{-4}\text{s}^{-1}$. Comparison between Fig. 4.3 (A) and Fig. 4.4 reveals that the rupture time significantly reduces as k_s increases from 10pN/nm to 50pN/nm . Thus the approximated analytical theory based on Eq 4.26 become less applicable at a larger k_s .

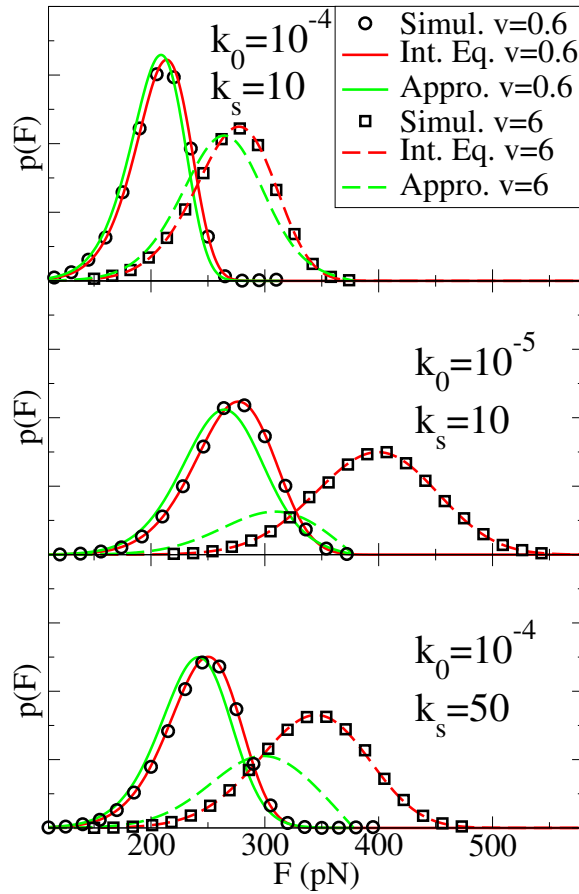


Figure 4.5: Rupture force distributions at two different pulling speeds, intrinsic rates and effect pulling constants calculated from stochastic simulation (black circles or squares), the integral equation (red), and the approximated analytical theory (green). See Eqs 4.32, 4.26 and 4.29.

Experimentalists usually report the distribution and average of the force at rupture for different pulling speeds determined from the integration and the differentiation of the measured survival probability. Approximate analytical formulas for them are given in Eqs 4.28

and 4.29. As shown in Fig. 4.3 and Fig. 4.4, the areas under the survival probability from the exact solution (black or red) and the approximated analytical solution (green) are almost equal for all cases investigated. Thus the previous analytical expression Eq 4.28 based on the adiabatic approximation is still approximately valid when fitting the average force as a function of the pulling speeds. However the deviations of the rupture force distribution are severe especially at larger pulling speeds v , slower intrinsic rates k_0 or larger effective pulling spring constants k_s . A comparison between the predictions of the approximate theory, the stochastic simulation results, and the exact results determined from the integral equation for varying v , k_0 and k_s is shown in Fig. 4.5. Clearly, to fit the experimental data at relatively larger pulling speeds, larger pulling spring constant or smaller intrinsic reaction rates, it is quite necessary to obtain the numerical results from the integral equations for the specific model and not from the approximate theory.

4.5 Subdiffusion Model for Anomalous Rupture Force Distribution

Standard models based on Langevin dynamics in a simple one dimensional potential, like the Hummer and Szabo's model, gives a rupture force distribution with negative skewness. However, in a series of constant velocity pulling experiments on ligand-receptor systems, such as DNA-protein complex,⁴⁻⁷ alkylammonium ion binded to calixarene⁸ and protein-protein complex,⁹ rupture force distributions with positive skewness are observed. Clearly, standard models fail to explain these experiments.

Raible *et al.*¹⁰ extend standard models, by taking into account the heterogeneity of the potential surface explored in each realization of the pulling experiments. Specifically, a Gaussian distribution of the distance between the potential well and the transition state is assumed. In this way, the resulting rupture force distributions have positive skewness and

fit the experiment data well. The model of Raible *et al.*¹⁰ is similar to the static disorder model^{89,90} used by Kuo *et al.*⁹¹ to explain the non-exponential survival probability observed in constant force pulling experiments of ubiquitin. In the static disorder model, the transitions between different sub-ensembles are slower than the chemical reaction rate, and the kinetics is non-exponential after averaging the chemical reaction rates over different sub-ensembles. The model of Kuo *et al.*⁹¹ also implies Gaussian distributions of the distance to transition state and the barrier height. Recently, molecular dynamics simulations have revealed that water insertion plays a significant role in the single-molecule kinetics of the forced unfolding of ubiquitin.⁹² When the unfolding kinetics depends on the number of inserted water molecules, there might not exist a well-defined transition state, but rather a broad distribution of transition states which gives rise to static disorder and non-exponential decay.

Alternatively, we may consider a model that does not call for a probability distribution of potentials. Instead, we think there is no randomness in the one dimensional potential. However, the underlying dynamics on this potential is assumed to be subdiffusive dynamics. One interesting property of subdiffusive dynamics is that the mean square displacement of a subdiffusive particle under constant potential follows a power law t^α dependence on time with α smaller than one. From the perspective of continuous time random walk, subdiffusion emerges when the probability distribution function of the waiting time between successive jumps follows a inverse power law asymptotically, while Brownian diffusion requires the waiting time distribution to have a finite mean.⁶⁸ From the continuous time random walk model, one can derive a subdiffusive fractional Fokker-Planck equation,⁶⁸

$$\frac{\partial f}{\partial t} = \frac{\partial}{\partial x} \left[\beta K_\alpha \frac{\partial V(x,t)}{\partial x} + K_\alpha \frac{\partial}{\partial x} \right] D_t^{1-\alpha} f(x,t) \quad (4.43)$$

where $D_t^{1-\alpha}$ is a Riemann-Liouville fractional derivative operator

$$D_t^{1-\alpha} f(t) = \frac{1}{\Gamma(\alpha)} \frac{d}{dt} \int_0^t dt' \frac{f(t')}{(t-t')^{1-\alpha}}, \quad (4.44)$$

K_α is the generalized diffusion constant, and $\langle \Delta x^2(t) \rangle = \frac{2K_\alpha}{\Gamma(1+\alpha)} t^\alpha$ when $V(x, t) = 0$.

Weron *et al.*⁹³ have given the underlying stochastic process corresponding to a fractional Fokker-Planck equation with time-dependent potential. Their procedure of modeling such a stochastic process is given below. Basically, one need to model a subordinated process of a Langevin dynamics,

$$Y(t) = X(S_t). \quad (4.45)$$

$X(\tau)$ is a Langevin process and S_t is a subordinator that maps the real time t to a time τ in the Langevin process, such that the random walk in real time has a power-law waiting time distribution. For our purpose, the subordinator is the inverse-time α -stable subordinator defined as

$$S_t = \inf\{\tau : U(\tau) > t\}. \quad (4.46)$$

where $U(\tau)$ is a strictly increasing α -stable Lévy process. $U(\tau)$ is propagated numerically as

$$\begin{aligned} U(0) &= 0 \\ U(\tau_i) &= U(\tau_{i-1}) + (\Delta\tau)^{1/\alpha} \xi_i \end{aligned} \quad (4.47)$$

where $\tau_i = i\Delta t$ and ξ_i are drawn independently from a totally skewed positive Lévy α -stable distribution $S_\alpha^0(\sigma = 1, \beta = 1, \mu_0 = 0)$, see Ref 94.

$$\xi_i = c_1 \frac{\sin[\alpha(Q + \frac{\pi}{2})]}{[\cos(Q)]^{1/\alpha}} \left(\frac{\cos[Q - \alpha(Q + \frac{\pi}{2})]}{W} \right)^{(1-\alpha)/\alpha} [\tan(\frac{\pi}{2}\alpha)]^{-1}, \quad (4.48)$$

where $c_1 = [\cos(\frac{\pi}{2}\alpha)]^{-1/\alpha}$, the random variable Q is drawn from a uniform distribution on $(-\frac{\pi}{2}, \frac{\pi}{2})$, W is drawn from an exponential distribution e^{-x} . The Langevin process $X(\tau)$ is

$$dX(\tau) = -K_\alpha \beta \frac{\partial V(X, U(\tau))}{\partial X} d\tau + \sqrt{2K_\alpha} dB(\tau) \quad (4.49)$$

where $B(\tau)$ is a Wiener process. Note It is $U(\tau)$ but not τ being used in the above equation, so the time-dependent external force is not subordinated.⁹³ $X(\tau)$ is propagated numerically as

$$\begin{aligned} X(0) &= 0 \\ X(\tau_i) &= X(\tau_{i-1}) - K_\alpha \beta \frac{\partial}{\partial X} V(X(\tau_{i-1}), U(\tau_{i-1})) \Delta\tau + \sqrt{2K_\alpha \Delta t} \chi_i \end{aligned} \quad (4.50)$$

where χ_i are drawn independently from a standard normal distribution. The real time t are discretized $t_j = j\Delta t$. Since $U(\tau)$ is strictly increasing,

$$S_{t_j} = \tau_i \quad \text{if } U(\tau_{i-1}) < t_j \leq U(\tau_i). \quad (4.51)$$

Then using $Y(t_j) = X(S_{t_j})$, we obtain a trajectory $Y(t_j)$ such that its probability density function satisfies the subdiffusive fractional Fokker-Planck equation Eq 4.43.

Using the above procedure, we harvest trajectories of a subdiffusive particle in the time-dependent potential defined in Eq 4.17. The parameters of the potential are set as $k_m = 900$ pN/nm, $k_s = 10$ pN/nm, $b = 0.42$ nm, and $v = 6$ nm/ps. The diffusion constant is chosen as $D = 0.044$ nm²/ms, and the temperature is set to be 300 K. The corresponding intrinsic reaction rate for this setup is $k_0 = 10^{-4}$ s⁻¹. The stochastic processes are propagated using the Euler method. The timestep for the stochastic processes $U(\tau)$ and $X(\tau)$ is $\Delta\tau = 0.002$ ms. The timestep for $Y(t)$ is $\Delta t = 0.01$ ms. The simulation of one trajectory is terminated when $Y(t) > 0.42$ nm or $t > 100$ ms. 10^5 trajectories have been simulated. From which the survival probability and the rupture force distribution are calculated.

The survival probabilities for $\alpha = 1.0, 0.8, 0.6, 0.4$ are shown in Fig. 4.6. The survival probability for Brownian dynamics ($\alpha = 1$) can be fitted with a compressed exponential function $\exp[-(t/\tau_1)^{\beta_1}]$ with $\tau_1 = 4.81$ ms and $\beta_1 = 8.63$. This also implies the rupture force distribution is a Weibull distribution. It might be possible to derive an analytical asymptotic formula for the first passage time distribution for this simple potential. We leave this for future investigation. The survival probabilities for subdiffusive dynamics have long

time tails that could be fitted with a power-law $t^{-\alpha_1}$. Fitting between 16 and 63 ms, α_1 are 0.84, 0.64 and 0.42 for the curves with α being 0.80, 0.60 and 0.40 respectively. So α_1 is close to the corresponding α . This is related to that the characteristic temporal decay governed by a fractional Fokker-Planck equation is a Mittag-Leffler function $E_\alpha[-kt^\alpha]$.⁹⁵ A Mittag-Leffler function $E_\alpha[-kt^\alpha]$ asymptotically approaches a power-law $[k\Gamma(1-\alpha)t^\alpha]^{-1}$ at large time, and behaves like a stretched exponential $\exp(-kt^\alpha/\Gamma(1+\alpha))$ at small time.⁹⁵

Rupture force distributions (Eq 4.29) obtained from simulations of subdiffusive dynamics are shown in Fig 4.7. The rupture force distribution under Brownian dynamics ($\alpha = 1$) has negative skewness, which is typical for standard models and many experimental observations. The rupture force distribution under subdiffusive dynamics ($\alpha = 0.8, 0.6, 0.4$) has positive skewness which is in agreement with some forced rupture experiments for ligand-acceptor complex.⁴⁻⁹ In our subdiffusion model, the positive skewness is related to the trapping dynamics with a inverse power-law trapping time distribution. The position of the subdiffusive particle can lag behind the position of the instantaneous well of the time-dependent potential more than a Brownian particle could. The correspondence in forced rupture experiments is that the molecule responds to the constant velocity pulling very slowly and the molecule loses its structure at greater times.

Static disorder model can also explain anomalous rupture force distributions with positive skewness.¹⁰ Our subdiffusion model and the static disorder model could be two different perspectives of looking at the same thing, the inadequacy of using just one reaction coordinate to describe a rugged multi-dimensional potential surface. The exploration in other coordinates of the rugged multi-dimensional potential surface could result in a broad waiting time distribution from one point to another point on the projected one dimensional potential of mean force.⁴³ The two models both include the exploration in other coordinates implicitly. There could be some arbitrariness in separating the systematic force and the noise for a stochastic process. Similar to this, static disorder model puts other

coordinates' contribution in the potential of mean force, while subdiffusion model puts other coordinates' contribution in the noise. Subdiffusion models have been used to explain the non-exponential dynamics in some biological molecules and complexes.^{43,95,96} Xie and coworkers find that the non-exponential autocorrelation function of fluorescence lifetime fluctuation in Fre/FAD complex can be fit well, assuming the donor-acceptor distance is governed by subdiffusive dynamics in a potential of mean force.^{43,96} Metzler and Klafter find that survival probabilities of the rebinding chemical reaction of carbon monoxide to myoglobin can be fit by the Mittag-Leffler function, in agreement with the theory of Kramers problem under subdiffusion dynamics.⁹⁵ Here, our stochastic simulations suggest that the anomalous rupture force distributions observed in forced rupture of ligand-receptor complexes⁴⁻⁹ can also be explained with a subdiffusion model.

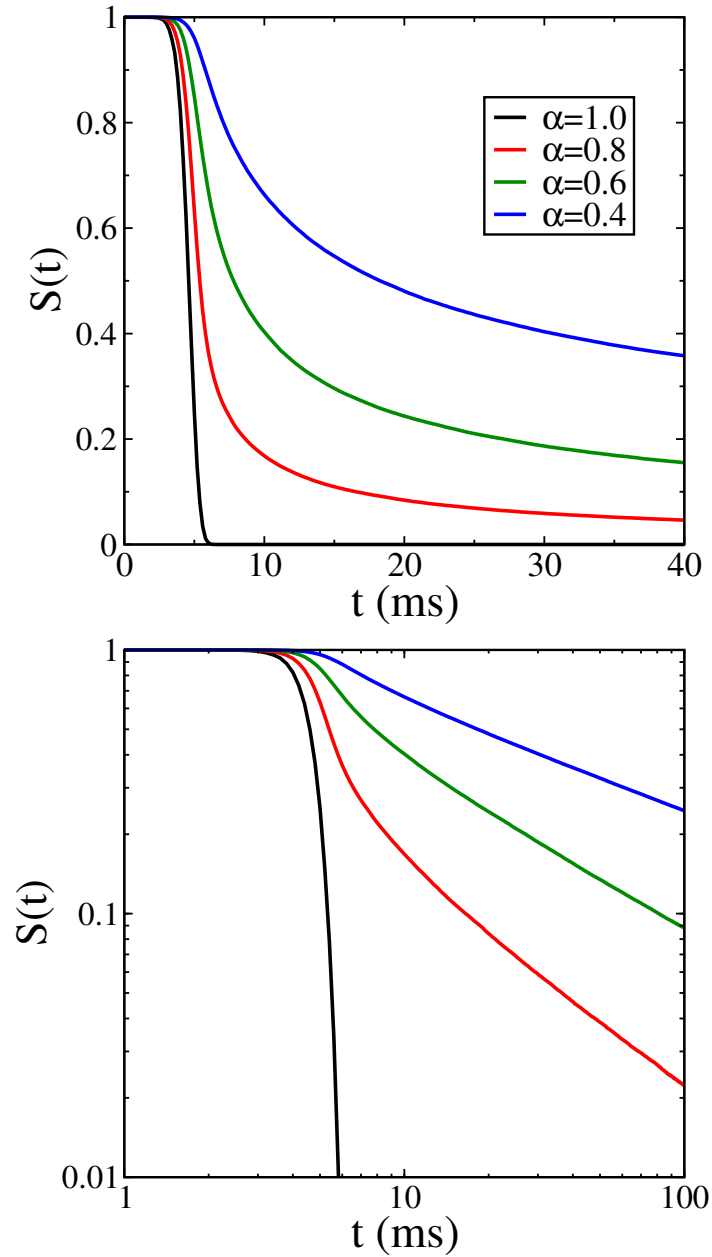


Figure 4.6: Survival probabilities simulated for subdiffusion in the potential defined in Eq 4.17 at different α . Top panel: plotted in normal scale; Bottom panel: plotted in logarithmic scale on both axes. Red, green, and blue are for α at 0.8, 0.6, and 0.4 respectively. The results for $\alpha = 1$ simulated in Brownian dynamics are shown in black color.

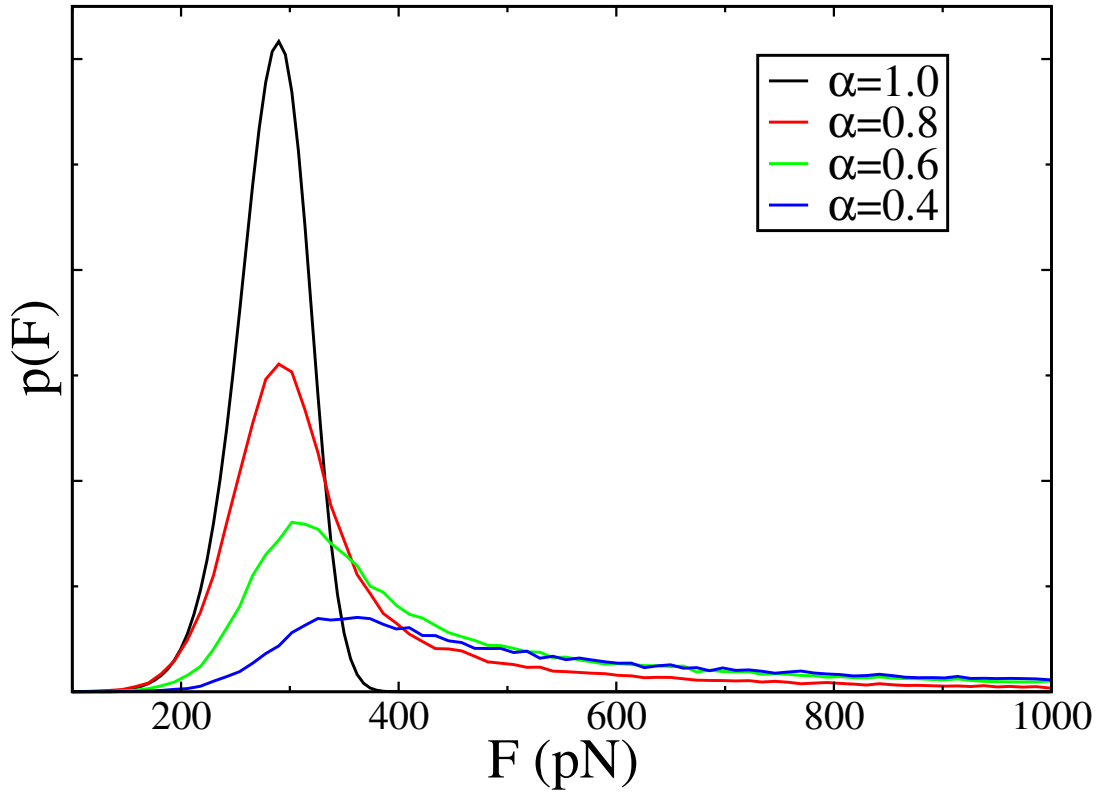


Figure 4.7: Rupture force distribution simulated for subdiffusion in the potential defined in Eq 4.17 at different α . Red, green, and blue are for α at 0.8, 0.6, and 0.4 respectively. The result for $\alpha = 1$ simulated in Brownian dynamics is shown in black color.

4.6 Conclusion

We have presented an integral equation connecting the usual conditional probability in the absence of reaction and the first passage time distribution and have found analytical solutions of this equation for the cases of free and biased particle diffusion in time-independent potentials. The long time tail $t^{-3/2}$ in the case of free diffusion rapidly vanishes as the diffusion is biased by a linear or harmonic potential. For diffusion in a time dependent potential of biological interest, we solved the integral equations numerically and compared the results with both stochastic simulations and a previously developed approximate theory

based on an adiabatic approximation. We found that iteration from the upper bound of the survival probability is useful for extracting kinetic and thermodynamic parameters (k_0 , k_s , b and k_m) from biological experimental data at extreme pulling speeds. We see that the approximated analytical formulas for the rupture force distribution based on the Kramers theory and the adiabatic assumption are likely to breakdown at larger pulling speeds, larger pulling spring constants or smaller intrinsic reaction rates. Once these thermodynamic and kinetic parameters are estimated or extracted either by fitting the average rupture force to the approximate analytical theories or by fitting the survival probability at extreme pulling speeds to their upper limits, our numerical treatment, based on the integral equation, can be immediately extended to fit experimental rupture force distributions at all pulling speeds and to further verify the validity of the parameters.

We provide a simple numerical procedure, based on an iterative solution of an integral equation for the survival probability, to extend previous methods for fitting the force distribution for arbitrary conditions of pulling speeds, cantilever spring constants and intrinsic reaction rates. However, we note that the underlying assumption that the rupture kinetics can be described by a Langevin process in its spatial diffusion limit might not be generally true. Anomalous rupture force distribution with positive skewness in some experiments on ligand-receptor complexes⁴⁻⁹ can not be explained by standard models based on Langevin dynamics. The anomalous rupture force distribution was explained with a static disorder model.¹⁰ Here we propose an alternative model based on subdiffusive dynamics. Stochastic simulations of this subdiffusion model give survival probabilities with power-law long time tail and rupture force distributions with positive skewness.

Bibliography

- [1] Liu, P.; Harder, E.; Berne, B. J. *J. Phys. Chem. B* **2004**, *108*, 6595-6602.
- [2] Kramers, H. A. *Physica* **1940**, *7*, 284 - 304.
- [3] Hummer, G.; Szabo, A. *Biophys. J.* **2003**, *85*, 5-15.
- [4] Bartels, F. W.; Baumgarth, B.; Anselmetti, D.; Ros, R.; Becker, A. *J. Struc. Biol.* **2003**, *143*, 145 - 152.
- [5] Eckel, R.; Wilking, S. D.; Becker, A.; Sewald, N.; Ros, R.; Anselmetti, D. *Angew. Chem. Int. Ed.* **2005**, *44*, 3921–3924.
- [6] Bartels, F. W.; McIntosh, M.; Fuhrmann, A.; Metzendorf, C.; Plattner, P.; Sewald, N.; Anselmetti, D.; Ros, R.; Becker, A. *Biophys. J.* **2007**, *92*, 4391 - 4400.
- [7] Krasnoslobodtsev, A. V.; Shlyakhtenko, L. S.; Lyubchenko, Y. L. *J. Mol. Biol.* **2007**, *365*, 1407 - 1416.
- [8] Eckel, R.; Ros, R.; Decker, B.; Mattay, J.; Anselmetti, D. *Angew. Chem. Int. Ed.* **2005**, *44*, 484–488.
- [9] Bonanni, B.; Kamruzzahan, A.; Bizzarri, A.; Rankl, C.; Gruber, H.; Hinterdorfer, P.; Cannistraro, S. *Biophys. J.* **2005**, *89*, 2783 - 2791.

- [10] Raible, M.; Evstigneev, M.; Bartels, F.; Eckel, R.; Nguyen-Duong, M.; Merkel, R.; Ros, R.; Anselmetti, D.; Reimann, P. *Biophys. J.* **2006**, *90*, 3851 - 3864.
- [11] Alba-Simionesco, C.; Coasne, B.; Dosseh, G.; Dudziak, G.; Gubbins, K. E.; Radhakrishnan, R.; Sliwinska-Bartkowiak, M. *J. Phys.: Condens. Matter* **2006**, *18*, R15.
- [12] Christenson, H. K. *J. Phys.: Condens. Matter* **2001**, *13*, R95.
- [13] Richert, R. *Annu. Rev. Phys. Chem.* **2011**, *62*, 65-84.
- [14] Granick, S.; Bae, S. C.; Kumar, S.; Yu, C. *Physics* **2010**, *3*, 73.
- [15] Khan, S. H.; Matei, G.; Patil, S.; Hoffmann, P. M. *Phys. Rev. Lett.* **2010**, *105*, 106101.
- [16] Morineau, D.; Xia, Y.; Alba-Simionesco, C. *J. Chem. Phys.* **2002**, *117*, 8966-8972.
- [17] Le Quellec, C.; Dosseh, G.; Audonnet, F.; Brodie-Linder, N.; Alba-Simionesco, C.; Hussler, W.; Frick, B. *Eur. Phys. J. Spec. Top* **2007**, *141*, 11-18 10.1140/epjst/e2007-00009-y.
- [18] Chaban, V. *Chemical Physics Letters* **2010**, *496*, 50 - 55.
- [19] Kalugin, O. N.; Chaban, V. V.; Loskutov, V. V.; Prezhdo, O. V. *Nano Lett.* **2008**, *8*, 2126-2130 PMID: 18627204.
- [20] Loughnane, B.; Farrer, R.; Scodinu, A.; Fourkas, J. *J. Chem. Phys.* **1999**, *111*, 5116.
- [21] Zhang, J.; Jonas, J. *J. Phys. Chem* **1993**, *97*, 8812.
- [22] Tanaka, H.; Iiyama, T.; Uekawa, N.; Suzuki, T.; Matsumoto, A.; Grn, M.; Unger, K. K.; Kaneko, K. *Chem. Phys. Lett.* **1998**, *293*, 541 - 546.

- [23] Kittaka, S.; Iwashita, T.; Serizawa, A.; Kranishi, M.; Takahara, S.; Kuroda, Y.; Mori, T.; Yamaguchi, T. *J. Phys. Chem. B* **2005**, *109*, 23162-23169.
- [24] Yamaguchi, T.; Yoshida, K.; Smirnov, P.; Takamuku, T.; Kittaka, S.; Takahara, S.; Kuroda, Y.; Bellissent-Funel, M.-C. *Euro. Phys. J. Spec. Top.* **2007**, *141*, 19-27.
- [25] Yamaguchi, T.; Sugino, H.; Ito, K.; Yoshida, K.; Kittaka, S. *J. Mol. Liq.* **2011**, *164*, 53 - 58.
- [26] Morales, C. M.; Thompson, W. H. *J. Phys. Chem. A* **2009**, *113*, 1922.
- [27] Gulmen, T.; Thompson, W. *Langmuir* **2009**, *25*, 1103.
- [28] Hu, Z.; Weeks, J. D. *J. Phys. Chem. C* **2010**, *114*, 10202.
- [29] Ding, F.; Hu, Z.; Zhong, Q.; Manfred, K.; Gattass, R. R.; Brindza, M. R.; Fourkas, J. T.; Walker, R. A.; Weeks, J. D. *J. Phys. Chem. C* **2010**, *114*, 17651-17659.
- [30] Milischuk, A. A.; Ladanyi, B. M. *J. Chem. Phys* **2011**, *135*, 174709.
- [31] Redner, S. *A Guide to first-passage processes*; Cambridge University Press: The Pitt Building, Trumpington Street, Cambridge, United Kingdom, 2001.
- [32] Dudko, O. K.; Hummer, G.; Szabo, A. *Phys. Rev. Lett.* **2006**, *96*, 108101.
- [33] Dudko, O. K.; Hummer, G.; Szabo, A. *Proc. Natl. Acad. Sci. USA* **2008**, *105*, 15755-15760.
- [34] Freund, L. B. *Proc. Natl. Acad. Sci. USA* **2009**, *106*, 8818-8823.
- [35] Bell, G. *Science* **1978**, *200*, 618-627.
- [36] Evans, E.; Ritchie, K. *Biophys. J.* **1997**, *72*, 1541 - 1555.

- [37] Evans, E. A.; Calderwood, D. A. *Science* **2007**, *316*, 1148-1153.
- [38] Carrion-Vazquez, M.; Oberhauser, A. F.; Fowler, S. B.; Marszalek, P. E.; Broedel, S. E.; Clarke, J.; Fernandez, J. M. *Proc. Natl. Acad. Sci. USA* **1999**, *96*, 3694-3699.
- [39] Schlierf, M.; Rief, M. *Biophys. J.* **2006**, *90*, L33-L35.
- [40] Math, J.; Visram, H.; Viasnoff, V.; Rabin, Y.; Meller, A. *Biophys. J.* **2004**, *87*, 3205-3212.
- [41] Chandrasekhar, S. *Rev. Mod. Phys.* **1943**, *15*, 1-89.
- [42] Montroll, E. W.; Weiss, G. H. *J. Math. Phys.* **1965**, *6*, 167-181.
- [43] Yang, H.; Luo, G.; Karnchanaphanurach, P.; Louie, T.-M.; Rech, I.; Cova, S.; Xun, L.; Xie, X. S. *Science* **2003**, *302*, 262-266.
- [44] Gee, P. J.; van Gunsteren, W. F. *Mol. Phys.* **2006**, *104*, 477-483.
- [45] Bródka, A.; Zerda, T. W. *J. Chem. Phys.* **1996**, *104*, 6319-6326.
- [46] Lee, S. H.; Rossky, P. J. *J. Chem. Phys.* **1994**, *100*, 3334-3345.
- [47] Giovambattista, N.; Rossky, P. J.; Debenedetti, P. G. *Phys. Rev. E* **2006**, *73*, 041604.
- [48] Nikitin, A. M.; Lyubartsev, A. P. *J. Comput. Chem.* **2007**, *28*, 2020-2026.
- [49] VandeVondele, J.; Krack, M.; Mohamen, F.; Parrinello, M.; Chassaing, T.; Hutter, J. *Comp. Phys. Comm.* **2005**, *167*, 103.
- [50] Becke, A. *Phys. Rev. A* **1988**, *38*, 3098.
- [51] Lee, C.; Wang, W.; Parr, R. *Phys. Rev. B* **1988**, *37*, 785.

- [52] VandeVondele, J.; Lynden-Bell, R.; Meijer, E. J.; Sprik, M. *J. Phys. Chem. B* **2006**, *110*, 3614.
- [53] Schiffmann, F.; Hutter, J.; VandeVondele, J. *J. Phys.: Condens. Matter* **2008**, *20*, 064206.
- [54] vanBeest, B.; Kramer, G.; Santen, R. *V. Phys. Rev. Lett.* **1990**, *64*, 1955.
- [55] Carre, A.; Horbach, J.; Ispas, S.; Kob, W. *Europhys. Lett.* **2008**, *82*, 17001.
- [56] Price, M. L.; Ostrovsky, D.; Jorgensen, W. *J. Comput. Chem.* **2001**, *13*, 1340.
- [57] Weiner, S. J.; Kollman, P. A.; Case, D. A.; Singh, U. C.; Ghio, C.; Alagona, G.; Profeta, S.; Weiner, P. *J. Am. Chem. Soc.* **1984**, *106*, 765.
- [58] Soper, A. K. *J. Phys.: Condens. Matter* **1997**, *9*, 2399.
- [59] Mancinelli, R.; Imberti, S.; Soper, A. K.; Liu, K. H.; Mou, C. Y.; Bruni, F.; Ricci, M. A. *J. Phys. Chem. B* **2009**, *113*, 16169.
- [60] Brinker, C. J.; Scherer, G. W. *Sol-Gel Science: The Physics and Chemistry of Sol-Gel Processing Academic, San Diego, 1990*, .
- [61] Rodriguez, J.; Elola, M. D.; Laria, D. *J. Phys. Chem. B* **2010**, *114*, 7900-7908.
- [62] Hess, B.; Kutzner, C.; van der Spoel, D.; Lindahl, E. *J. Chem. Theory. Comput.* **2008**, *4*, 435.
- [63] Liu, S.; Hu, Z.; Weeks, J. D.; Fourkas, J. T. *J. Phys. Chem. C* **2012**, *116*, 4012-4018.
- [64] Horng, P.; Brindza, M. R.; Walker, R. A.; Fourkas, J. T. *J. Phys. Chem. C* **2010**, *114*, 394.

- [65] Lide, D. R., Ed.; *Handbook of Chemistry and Physics*; CRC Press: Boca Raton, 77th ed.; 1996.
- [66] Loughnane, B.; Scodinu, A.; Fourkas, J. *J. Phys. Chem. B* **1999**, *103*, 6061.
- [67] Loughnane, B.; Farrer, R.; Fourkas, J. *J. Phys. Chem. B* **1998**, *102*, 5409.
- [68] Metzler, R.; Klafter, J. *Physics Reports* **2000**, *339*, 1.
- [69] Wong, I. Y.; Gardel, M. L.; Reichman, D. R.; Weeks, E. R.; Valentine, M. T.; Bausch, A. R.; Weitz, D. A. *Phys. Rev. Lett.* **2004**, *92*, 178101.
- [70] Gallo, P.; Rovere, M.; Chen, S. H. *J. Phys.: Condens. Matter* **2010**, *22*, 284102.
- [71] Gallo, P.; Rovere, M.; Spohr, E. *J. Chem. Phys* **2000**, *113*, 11324.
- [72] Easteal, A. *J. Aust. J. Chem.* **1980**, *33*, 1667.
- [73] Arfken, G. B.; Weber, H. J.; Harris, F. *Mathematical Methods for Physicists, Sixth Edition: A Comprehensive Guide*; Academic Press: San Diego, 6 ed.; 2005.
- [74] Naqvi, K. R.; Mork, K. J.; Waldenstrøm, S. *Phys. Rev. Lett.* **1982**, *49*, 304–307.
- [75] Botan, A.; Rotenberg, B.; Marry, V.; Turq, P.; Noetinger, B. *J. Phys. Chem. C* **2011**, *115*, 16109-16115.
- [76] Rotenberg, B.; Marry, V.; Vuilleumier, R.; Malikova, N.; Simon, C.; Turq, P. *Geochim. cosmochim. acta* **2007**, *71*, 5089 - 5101.
- [77] Wick, C. D.; Dang, L. X. *J. Phys. Chem. B* **2005**, *109*, 15574-15579 PMID: 16852975.
- [78] Yeh, I.-C.; Hummer, G. *J. Phys. Chem. B* **2004**, *108*, 15873-15879.

- [79] Predota, M.; Cummings, P. T.; Wesolowski, D. J. *J. Phys. Chem. C* **2007**, *111*, 3071-3079.
- [80] Alegre-Cebollada, J.; Kosuri, P.; Rivas-Pardo, J. A.; Fernandez, J. M. *Nature Chem.* **2011**, *3*, 882–887.
- [81] Zwanzig, R. *Nonequilibrium Statistical Mechanics*; Oxford University Press: New York, USA, 2001.
- [82] Szabo, A.; Lamm, G.; Weiss, G. H. *J. Stat. Phys.* **1984**, *34*, 225-238
10.1007/BF01770356.
- [83] Bicout, D. J.; Szabo, A. *J. Chem. Phys.* **1997**, *106*, 10292-10298.
- [84] Szabo, A.; Schulten, K.; Schulten, Z. *J. Chem. Phys.* **1980**, *72*, 4350-4357.
- [85] Gerstein, G. L.; Mandelbrot, B. *Biophys. J.* **1964**, *4*, 41-68.
- [86] Fienberg, S. E. *Biometrics* **1974**, *30*, 399–427.
- [87] Risken, H. *The Fokker-Planck Equation*; Springer-Verlag: Berlin Heidelberg, 1989.
- [88] Harris, N. C.; Kiang, C.-H. *Phys. Rev. E* **2009**, *79*, 041912.
- [89] Zwanzig, R. *Acc. Chem. Res.* **1990**, *23*, 148-152.
- [90] Zwanzig, R. *J. Chem. Phys.* **1992**, *97*, 3587-3589.
- [91] Kuo, T.-L.; Garcia-Manyes, S.; Li, J.; Barel, I.; Lu, H.; Berne, B. J.; Urbakh, M.; Klafter, J.; Fernandez, J. M. *Proc. Natl. Acad. Sci. USA* **2010**, *107*, 11336-11340.
- [92] Li, J.; Fernandez, J. M.; Berne, B. J. *Proc. Natl. Acad. Sci. USA* **2010**, *107*, 19284-19289.
- [93] Weron, A.; Magdziarz, M.; Weron, K. *Phys. Rev. E* **2008**, *77*, 036704.

[94] Weron, R. *Int. J. Mod. Phys. C* **2001**, *12*, 209.

[95] Metzler, R.; Klafter, J. *Chem. Phys. Lett.* **2000**, *321*, 238 - 242.

[96] Yang, H.; Xie, X. S. *J. Chem. Phys.* **2002**, *117*, 10965-10979.

Appendix A

Analytical solutions of the first passage time distribution for three model potentials

We derive the analytical solutions of the integral Eqs 4.31 and 4.32 for the simple potentials illustrated in Fig. 4.2 (A) in this appendix. For $V_0(x) = 0$, we find

$$\int_{-\infty}^b dx f^0(x, t|b, \tau) = \int_{-\infty}^b dx \frac{1}{\sqrt{4\pi D(t-\tau)}} \exp\left\{-\frac{(x-b)^2}{4D(t-\tau)}\right\} = \frac{1}{2}. \quad (\text{A1})$$

Eq 4.32 thus takes a remarkably simple form:

$$S(t) = \int_{-\infty}^b dx f^0(x, t|x_0, 0) - \frac{1}{2}(1 - S(t)). \quad (\text{A2})$$

The analytical solution of the survival probability is :

$$S(t) = 2 \int_{-\infty}^b dx f^0(x, t|x_0, 0) - 1, \quad (\text{A3})$$

and its differentiation gives the first passage time distribution:

$$h(t) = -\frac{dS(t)}{dt} = \frac{(b-x_0)}{\sqrt{4\pi Dt^3}} \exp\left\{-\frac{(b-x_0)^2}{4Dt}\right\}. \quad (\text{A4})$$

which is the same as Eq 4.34. Alternatively, the Laplace transform of Eq 4.31 in the case of free particle diffusion yields:

$$\frac{1}{\sqrt{4Ds}} \exp \left\{ -\frac{(x-b)\sqrt{s}}{\sqrt{D}} \right\} \tilde{h}(s) = \frac{1}{\sqrt{4Ds}} \exp \left\{ -\frac{(x-x_0)\sqrt{s}}{\sqrt{D}} \right\}. \quad (\text{A5})$$

Immediately we have:

$$\tilde{h}(s) = \exp \left\{ -\frac{(b-x_0)\sqrt{s}}{\sqrt{D}} \right\}, \quad (\text{A6})$$

and its inverse Laplace transform gives the same result as in Eq A4.

We further rewrite Eq 4.31 as:

$$\int_0^t d\tau h(\tau) \frac{f^0(x,t|b,\tau)}{f^0(x,t|x_0,0)} = 1. \quad (\text{A7})$$

$h(\tau)$ implicitly depends on b and x_0 only and it has to be chosen such that the integration is 1 for any $x \geq b$. For the case of $V_0(x) = 0$,

$$\frac{f^0(x,t|b,\tau)}{f^0(x,t|x_0,0)} = \frac{\sqrt{t}}{\sqrt{t-\tau}} \exp \left\{ -\frac{(x-b)^2}{4D(t-\tau)} + \frac{(x-x_0)^2}{4Dt} \right\}. \quad (\text{A8})$$

The exponential part of $h(t)$ as in Eq A4 completes an parabolic form inside the exponential:

$$-\frac{(x-b)^2}{4D(t-\tau)} + \frac{(x-x_0)^2}{4Dt} - \frac{(b-x_0)^2}{4D\tau} = -\frac{[(x-x_0)\tau - (b-x_0)t]^2}{4Dt\tau(t-\tau)}. \quad (\text{A9})$$

After a substitution of the integration dummy variable: $y = \sqrt{t-\tau}/\sqrt{t\tau}$, Eq A7 becomes a known result:

$$\int_0^\infty dy \frac{2d}{\sqrt{\pi}} \exp \left\{ -d^2 \left[y - \frac{c}{y} \right]^2 \right\} = 1, \quad (\text{A10})$$

where $c = (x-b)/[t(b-x_0)]$ and $d = (b-x_0)/(4D)$ are both positive parameters independent of y . The derivation from Eq A7 to Eq A10 provides a simple method through which we can guess the form of $h(t)$ such that the integration does not depend on the parameter x , for general cases of the biased diffusions.

For $V_0(x) = -Fx$, the usual conditional probability of the linear process takes the form of Eq 4.35. We might make the following analogy:

$$x \leftrightarrow x - FDt, \quad b \leftrightarrow b - FD\tau, \quad x_0 \leftrightarrow x_0.$$

When we choose $h(\tau) \sim \exp\left\{-\frac{(b - FD\tau - x_0)^2}{4D\tau}\right\}$, the analog expression inside the exponential of the integral is:

$$\begin{aligned} -\frac{[(x-x_0)\tau - (b-x_0)t]^2}{4Dt\tau(t-\tau)} &\leftrightarrow -\frac{[(x-FDt-x_0)\tau - (b-FD\tau-x_0)t]^2}{4Dt\tau(t-\tau)} \\ &= -\frac{[(x-x_0)\tau - (b-x_0)t]^2}{4Dt\tau(t-\tau)}. \end{aligned} \quad (\text{A11})$$

which is the same as in the case of the free particle diffusion. Therefore taking the same coefficient as in Eq A4 arrives at Eq A10 after the substitution from τ to y . We thus find the result in Eq 4.36:

$$h(t) = \frac{(b-x_0)}{\sqrt{4\pi Dt^3}} \exp\left\{-\frac{(b-FDt-x_0)^2}{4Dt}\right\}. \quad (\text{A12})$$

For $V_0(x) = \frac{1}{2}kx^2$, we apply the following analogy:

$$\begin{aligned} x &\leftrightarrow xe^{Dkt}, & b &\leftrightarrow be^{Dk\tau}, & x_0 &\leftrightarrow x_0, \\ t &\leftrightarrow \frac{e^{2Dkt} - 1}{2Dk} = \hat{t}, & \tau &\leftrightarrow \frac{e^{2Dk\tau} - 1}{2Dk} = \hat{\tau}, & t - \tau &\leftrightarrow \frac{e^{2Dkt} - e^{2Dk\tau}}{2Dk} = \hat{t} - \hat{\tau}. \end{aligned}$$

The corresponding analog expression inside the exponential reads:

$$-\frac{[(x-x_0)\tau - (b-x_0)t]^2}{4Dt\tau(t-\tau)} \leftrightarrow -\frac{[(xe^{Dkt} - x_0)\hat{t} - (be^{Dk\tau} - x_0)\hat{\tau}]^2}{4D\hat{t}\hat{\tau}(\hat{t} - \hat{\tau})}. \quad (\text{A13})$$

In this case, it might not be easy to choose an appropriate coefficient of $h(\tau)$ such that the integral is independent of x . However, for $b = 0$, it is straightforward to have:

$$h(\tau) = \frac{d\hat{\tau}}{d\tau} \frac{b-x_0}{\sqrt{4\pi D\hat{\tau}^3}} \exp\left\{-\frac{(be^{Dk\tau} - x_0)^2}{4D\hat{\tau}}\right\} = \frac{e^{2Dk\tau}|x_0|}{\sqrt{4\pi D\hat{\tau}^3}} \exp\left\{-\frac{x_0^2}{4D\hat{\tau}}\right\}, \quad (\text{A14})$$

which is equivalent to Eq 4.38. We thus complete the analytical solutions for the three simple potentials in Fig. 4.2.

Appendix B

Time-dependent Green's function for a linear stochastic process in the absence of an absorbing boundary

The derivation of Eq 4.39 is explained here. There are many alternative methods to solve the stochastic differential equation described by Eq 4.4 in a time-dependent harmonic potential. One method is to use the solution for the Ornstein-Uhlenbeck process given on page 238 of Ref 87. We indicate here a similar approach for the simple case of one-dimensional system in order to illustrate this method. The Markov process of interest can be rewritten as

$$\frac{dx}{dt} = -D(k_m + k_s)x + Dk_s vt + \sqrt{2D} \frac{d\omega}{dt} \quad (\text{B1})$$

where $\omega(t)$ is the Wiener process. Considering the initial condition $x(\tau) = x_\tau$ with probability of 1, direct integration gives the solution as

$$\begin{aligned}
 x(t) &= x_\tau e^{-Dk(t-\tau)} + \int_\tau^t e^{-D(t-t')} (Dk_s v t' + \sqrt{2D} \frac{d\omega}{dt'}) dt' \\
 &= x_\tau e^{-Dk(t-\tau)} + \frac{k_s v}{Dk^2} ((1 - Dk\tau) e^{-Dk(t-\tau)} + Dkt - 1) + \sqrt{2D} \int_\tau^t e^{-Dk(t-t')} d\omega \quad (\text{B2}) \\
 &= \bar{x}_{\tau,t} + \sqrt{2D} \lim_{\Delta t \rightarrow 0} \sum_{i=1}^N e^{-Dk(t-\tau-(i-1)\Delta t)} \omega_i(\Delta t)
 \end{aligned}$$

where $\bar{x}_{\tau,t}$ is the same as in Eq 4.40 and $k = k_m + k_s$. $\omega_i(\Delta t)$ are treated as independent Gaussian random variable with variance Δt and $t = \tau + N\Delta t$. The variance of the random variable $x(t)$ is

$$\sigma_{t-\tau}^2 = 2De^{-2Dk(t-\tau)} \lim_{\Delta t \rightarrow 0} \Delta t \frac{1 - e^{2Dk(t-\tau)}}{1 - e^{2Dk\Delta t}} = \frac{1 - e^{-2Dk(t-\tau)}}{k} \quad (\text{B3})$$